

國立交通大學  
光電工程學系暨研究所  
博士論文

鈣鈦礦結構對螢光及鐵性材料特性的影響



研究 生：黃同慶

指 導 教 授：謝文峰 教授

中華民國九十八年十月

# 鈣鈦礦結構對螢光及鐵性材料特性影響

## Influence of perovskite structure on luminescence and characteristics of ferroics

研究 生：黃 同 慶

Student : Tung-Ching Huang

指導 教授：謝 文 峰 教 授

Advisor: Dr. Wen-Feng Hsieh



A Dissertation

Submitted to Department of Photonics and Institute of Electro-Optical Engineering  
College of Electrical Engineering and Computer Science

National Chiao Tung University  
In Partial Fulfillment of the Requirements  
for the Degree of  
Doctor of Philosophy  
in  
Electro-Optical Engineering

October 2009  
Hsinchu, Taiwan, Republic of China

中華民國九十八年十月

## 誌謝

由衷地感謝許多的老師與夥伴們給予我無盡的幫助和建議，讓我順利地完成我的博士學位，也感謝這個過程中你們給予我的感動和歡笑。

首先，我最要感謝的是我的指導老師 謝文峰教授，在學術上，謝謝老師帶我進入光譜的研究領域，教我如何增進自己的知識，訓練我如何尋找研究方向、獨自做實驗、建立自己一套邏輯性思考模式，進而架構一套研究模式，此外，特別感謝老師這幾年來給我許許多多的人生建議，我想告訴老師，很多您說過的話，我是有聽進去的，而且我想那些將會是我人生用之不盡的寶藏。接著，我要感謝 張振雄教授、徐嘉鴻老師和 許火順老師在我研究上的幫助，也要感謝口試委員們對我的論文的指導與建議。最後我要感謝陪我走過研究生生涯的交大光電所雷射診測實驗室的夥伴們，老郭和阿政學長引領我進入研究的領域和智章學長給予的建議與幫助；潘晴如學姊(雖然她不喜歡我叫她學姐)，她的美食團是我可以繼續念完博士班的最大動力，特別感謝她即使在畢業後的這一兩年來還是不斷地給我鼓勵和加油；楊松和林國峰不只在研究上給予許多的幫助，也感謝在吃喝玩樂上一路相伴，他們可是陪我走過美國和歐洲；感謝劉維仁在生活上和學業上的相互鼓勵；邱偉豪、郭晉嘉、王政丹、蔡明容、黃冠智和蔡智雅，很高興在人生旅途上與你們相遇，更感謝你們在我研究生涯的協助！

最後我要感謝的是我的家人，感謝阿公、阿媽、爸爸和媽媽，謝謝他們這麼都多年來支持與鼓勵，也要特別感謝我老婆和女兒一路的相伴與鼓勵，你們都是我過去、現在和未來不斷前進的最大動力。

# 鈣鈦礦結構對螢光及鐵性材料特性的影響

研究生：黃同慶

指導教授：謝文峰 教授

國立交通大學光電工程學系暨研究所

## 摘要

我們利用拉曼散射實驗研究物質尺寸和介面應力效應對鐵性材料(包含鈣鈦礦和尖石礦結構)物理特性的影響，同時也探討因取代而造成結構變化對摻雜在  $ABO_3$  鈣鈦礦結構中稀土族元素的發光機制的影響。所有的實驗樣品我們利用簡單的化學溶液合成法加以合成。由於取代效應，利用觀察到螢光和拉曼信號消失的現象，我們發現在鈦酸鑭鉛( $Pb_{0.8}La_{0.2}TiO_3$ )薄膜中當摻雜的三價鉕離子( $Er^{3+}$ )超過 7 mol%時，會對原先微距(short-range)結構中的鈦原子的移位量造成破壞。這個由於鈦原子的移位量造成的擾動(disorder)會破壞寄主(host materials)鈣鈦礦結構之中心對稱，進而激發稀土元素的螢光輻射和鈣鈦礦的拉曼訊號。在另外一個取代效應的研究中，當以 980nm 的半導體雷射激發鉕和镱雙摻雜的鈦酸鉛、鈦酸鋇、和鈦酸鋨粉末，觀察 upconversion 螢光光譜時，我們發現發紅光的機制由 energy-back-transfer (EBT) 程序所主導。EBT 的效率不僅依賴镱離子的濃度大小，也和鉕離子( $Er: ^4S_{3/2} \rightarrow ^4I_{13/2}$ )與镱離子 ( $Yb: ^2F_{7/2} \rightarrow ^2F_{5/2}$ ) 的殼層躍遷能階大小是否吻合息息相關。而這個殼層能階大小是否吻合，則取決於摻雜取代造成結構變化，所產生的晶格場(crystal field)變化對離子的殼層能階的影

響程度。

不同尺寸(size)鈦酸鋇奈米顆粒的晶格動力學研究中，當粉末顆粒由 140 nm 縮減到 30 nm 時，顆粒的四方晶特性(tetragonality)也隨之變弱，同時伴隨著單位晶胞(unit-cell)體積的膨脹，這也是造成光學聲子的縱模和橫模的分裂隨著顆粒尺寸變小而減少的主要機制；另外我們在這部份的研究中，也發現了  $A_1(TO_1)$  和  $A_1(TO_2)$  的耦合強度隨著顆粒尺寸變小而減少，進而造成  $A_1(TO_1)$  原先在拉曼光譜是以下陷(dip)表現的形式變成在奈米尺寸下是以峰型(peak)展示。

最後，在鈦酸鋇-氧化鐵鈷的多重鐵性系統的研究中，發現兩介質介面間的應力造成的磁電效應(magnetoelectric effect)和介質的聲子頻率位移有很強的相關性。受介面影響的聲子能量和多重鐵性系統中的鐵磁物質的鐵電特性都會受到介面間的應力影響；而這個介面間的應力大小，同時受到兩介質晶格不匹配和介質間的化學鍵鍵結程度的影響。在埋有自成長碟型氧化鐵鈷的鈦酸鋇(disk-3 type structure)的樣品，闡明了兩介質間有強的彈性交互作用。而這個較強的作用造成了它的鐵磁特性和晶格特性都有較大的變化，當鐵磁部分有較大的非對稱性磁頑力差和出現不存在飽和的磁化率，伴隨著的是鐵電部分的聲子存在較大的聲子頻率位移。

# Influence of perovskite structure on luminescence and characteristics of ferroics

Student: Tung-Ching Huang

Advisor: Dr. Wen-Feng Hsieh

Department of Photonics & Institute of Electro-Optical Engineering  
National Chiao Tung University

## Abstract

We investigated on the physical characteristics of ferroics,  $\text{ABO}_3$ -type perovskite and  $\text{AB}_2\text{O}_4$ -type spinel, which depend on size and strain effects by Raman spectroscopy, and the emission mechanism of rare-earth doped / co-doped  $\text{ABO}_3$  films on substitution effect. All the samples discussed in this thesis were prepared by chemical solution methods. In one of the cases of substitution effect, we found destruction to a displacement of Ti in the short-range structure by observing the disappearance of emission and Raman signals when the  $\text{Er}^{3+}$  concentration exceeds 7 mol% in sol-gel-derived  $\text{Pb}_{0.8}\text{La}_{0.2}\text{TiO}_3$  (PLT) polycrystalline films. The disorder due to a displacement of Ti breaks the centrosymmetry to activate emission of rare earth ions such as  $\text{Er}^{3+}$  and Raman modes of perovskites. We found that the symmetry breaking diminishes with introducing more  $\text{Er}^{3+}$  ions. Furthermore, in another case of substitution effect, we found that quenching of green upconversion (UC) emission accompanied with enhancement of red UC emission under a 980 nm laser pumping was observed dominated by the energy back-transfer (EBT) process in  $\text{Er}^{3+}$  and  $\text{Yb}^{3+}$  co-doped  $\text{PbTiO}_3$  (PTO),  $\text{BaTiO}_3$  (BTO), and  $\text{SrTiO}_3$  (STO)

polycrystalline powders. The efficiency of the EBT process depends not only on Yb<sup>3+</sup> concentration but also on level match of the doped Er<sup>3+</sup> and Yb<sup>3+</sup> ions caused by the crystal fields with different symmetries. Results of emission spectra and X-ray diffraction (XRD) confirm that the centrosymmetric crystal field arising from reducing tetragonality causes level match of transition  $^4S_{3/2} \rightarrow ^4I_{13/2}$  of Er<sup>3+</sup> and  $^2F_{7/2} \rightarrow ^2F_{5/2}$  of Yb<sup>3+</sup> that is responsible for enhancing red UC emission.

Moreover, in the case of size-dependent lattice dynamics of BTO nanoparticles, we found, upon decreasing the particle size from 140 nm to 30 nm, the tetragonality of BTO nanocrystallites is reduced accompanied with expanding unit-cell volume, which is the dominant mechanism for reducing giant splitting of longitudinal optical (LO) and transverse optical (TO) phonon modes in BTO system. The weakening coupling of two low-frequency modes among three A<sub>1</sub>(TO) phonons leads to change the lowest one from a spectral dip to a peak; whereas the increasing coupling strength between two high-frequency modes, repels them farther so that the less reducing in spectral separation.

Finally, in the part of strain effect, we found the energy of interfacial phonons and ferromagnetic properties depend on stress due to not only the lattice misfit but also the degree of chemical bonding at the interface between CFO and PTO matrices. The disk-3 type structure, the self-assembled CFO disks embedded in PTO matrix, illustrates the strong elastic interactions between these two phases. The largest nonsymmetrical coercivity H<sub>c</sub> and the absence of saturation magnetization M<sub>s</sub> of CFO matches with the largest Raman shift of A<sub>1</sub>(TO<sub>2</sub>) and A<sub>1</sub>(TO<sub>3</sub>) modes of PTO found in the disk-3 type as compared with the CFO and PTO multilayered structure and the CFO particles embedded in PTO matrix.

# Table of Contents

|  |           |
|--|-----------|
| Abstract in Chinese.....   | I         |
| Abstract in English .....  | III       |
| Contents.....  | V         |
| List of Figures.....   | IX        |
| List of Tables.....  | XIII      |
| <br>   |           |
| <b>Chapter 1    Introduction.....</b>  | <b>1</b>  |
| 1.1 Ferroelectricity, Photorefractive effect, and Perovskite.....  | 1         |
| 1.2 Ferromagneticity and Spinel.....   | 6         |
| 1.3 Multiferroic materials.....  | 11        |
| 1.4 Motive ( <b>develop a solution for integrated modulable decices</b> ).....                             | 13        |
| 1.4.1 Dependence of crystal structure on substitution, <b>size</b> , and shape.....                        | 13        |
| 1.4.2 Dependence of mechanism of luminescence on crystal structure in rare-earth ions doped materials..... | 14        |
| 1.4.3 Dependence of coupling of electricity and magnetism on lattice mismatch.....                         | 15        |
| 1.5 Organization of this dissertation.....   | 16        |
| References.....  | 18        |
| <b>Chapter 2    Theoretical Background.....</b>  | <b>20</b> |

|                  |   |           |
|------------------|---|-----------|
| 2.1              | Vibrational spectroscopy.....   | 20        |
| 2.1.1            | IR absorption.....  | 20        |
| 2.1.2            | Raman scattering.....   | 22        |
| 2.2              | Coupled phonon model.....   | 24        |
| 2.3              | Born effective charges and LO-TO splitting.....                         | 26        |
| 2.4              | Optical transitions of rare earth doped materials and upconversion..... | 31        |
| 2.4.1            | Fundamental optical transitions.....                                    | 31        |
| 2.4.2            | Upconversion.....   | 33        |
| 2.5              | Multiferroic magnetoelectrics .....                                     | 35        |
| References.....  |   | 39        |
| <b>Chapter 3</b> | <b>Experimental procedures and characterization techniques.....</b>     | <b>41</b> |
| 3.1              | Synthesis mechanisms and sample preparation.....                        | 41        |
| 3.1.1            | Barium titanate nanoparticles .....                                     | 41        |
| 3.1.2            | Barium titanate rods .....  | 43        |
| 3.1.3            | Rare earth doped perovskites.....                                       | 45        |
| 3.1.3.1          | Er <sup>3+</sup> -doped PLT poly-crystalline films.....                 | 45        |
| 3.1.3.2          | Er-Yb codoped ferroelectrics.....                                       | 46        |
| 3.1.4            | Multiferroic films.....   | 47        |
| 3.2              | Characterization of structure.....                                      | 48        |
| 3.2.1            | X-ray Diffraction.....  | 48        |
| 3.2.2            | Field-Emission Scanning Electron Microscopy (FESEM).....                | 49        |

|  |           |
|--|-----------|
| 3.2.3 Raman spectroscopy .....   | 49        |
| 3.3 Characterization of optical properties--Photoluminescence spectroscopy .....   | 51        |
| 3.4 Characterization of megnetic properties--Superconducting quantum interference device magnetometry.....   | 51        |
| References.....  | 52        |
| <b>Chapter 4      Destruction of the short-range disorder due to erbium doping in <math>\text{Pb}_{0.8}\text{La}_{0.2}\text{TiO}_3</math> films.....</b> | <b>53</b> |
| 4.1 Crystal structure (results of XRD).....  | 53        |
| 4.2 Relationship between results of emission spectra and Raman spectra.....  | 58        |
| 4.3 Summary.....   | 64        |
| References.....  | 66        |
| <b>Chapter 5      Er-Yb codoped ferroelectrics for controlling visible upconversion emissions.....</b>   | <b>67</b> |
| 5.1 Upconversion emission.....   | 68        |
| 5.2 Mechanisms of upconversion emission.....   | 72        |
| 5.2.1 Crystal structure (results of XRD).....  | 72        |
| 5.2.2 Symmetry-dependent upconversion mechanism.....   | 75        |
| 5.2.3 Pump power dependent upconversion.....   | 76        |
| 5.3 Summary.....   | 78        |
| References.....  | 80        |
| <b>Chapter 6      Size-dependent lattice dynamics of <math>\text{BaTiO}_3</math> nanoparticles.....</b>  | <b>81</b> |
| 6.1 Size-dependent lattice constants of $\text{BaTiO}_3$ nanoparticles.....  | 82        |

|   |            |
|---|------------|
| 6.2 Size-dependent Raman spectra of BaTiO <sub>3</sub> nanoparticles.....   | 87         |
| 6.3 Born effective charges and LO-TO splitting in BaTiO <sub>3</sub> nanoparticles system.....  | 95         |
| 6.4 Summary.....  | 98         |
| References.....   | 99         |
| <b>Chapter 7 Correlating phonon frequency shift with magnetoelectric effect in the PbTiO<sub>3</sub>-CoFe<sub>2</sub>O<sub>4</sub> multiferroic system due to interfacial stress.....</b> | <b>101</b> |
| 7.1 Microstructure and morphology.....  | 102        |
| 7.2 Magnetic properties.....  | 108        |
| 7.3 Relationship between interfacial phonon behavior and magnetic properties....  | 112        |
| 7.4 Summary.....  | 116        |
| References.....   | 118        |
| <b>Chapter 8 Conclusions and Prospective .....</b>  | <b>119</b> |
| 8.1 Conclusions.....  | 119        |
| 8.2 Prospective.....  | 123        |
| References.....   | 127        |
| <b>Vita.....</b>  | <b>128</b> |
| <b>Publication list.....</b>  | <b>129</b> |

## List of Figures

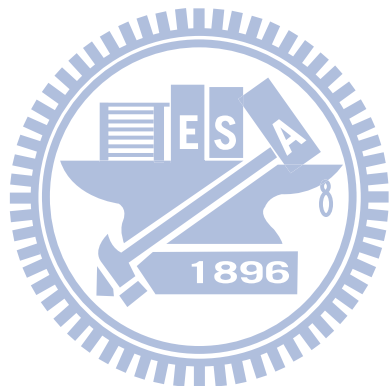
|   |    |
|---|----|
| Figure 1.1 Schematic illustrations for A-cell and B-cell types of unit cell for cubic- $\text{ABO}_3$ and possible alternative ways to derive cubic- $\text{ABO}_3$ structure.....  | 4  |
| Figure 1.2 Properties of paramagnetism, diamagnetism, and ferromagnetism.....   | 7  |
| Figure 1.3 Arrangement of atoms within the $\text{MgAl}_2\text{O}_4$ unit cell.....   | 10 |
| Figure 1.4 Schematic illustration of multiferroic material.....   | 12 |
| Figure 2.1 Diagram of dipole moment.....  | 21 |
| Figure 2.2 Transition from level $i$ to $f$ .....   | 22 |
| Figure 2.3 Energy level diagram of $\text{PLT:Er}^{+3}$ thin films.....   | 32 |
| Figure 2.4 Energy level diagram of $\text{Er}^{3+}$ and $\text{Yb}^{3+}$ ions as well as the proposed mechanisms to produce UC spectra.....   | 34 |
| Figure 3.1 Flowchart of $\text{BaTiO}_3$ nanocrystals preparation by glycothermal treatment method.....   | 42 |
| Figure 3.2 Proposed schematic diagram of the synthetic mechanism of $\text{BaTiO}_3$ rods.....  | 43 |
| Figure 3.3 Flowchart of sol-gel derived $\text{Er}^{3+}$ -doped PLT poly-crystalline films.....   | 45 |
| Figure 3.4 Schematic illustration of three thin films with different connectivity schemes: (a) the 0-3 type with CFO particles embedded in PTO matrix, (b) the 2-2 type with CFO and PTO nanolayers, and (c) the disk-3 type with CFO disc aligned in PTO matrix..... | 47 |
| Figure 3.5 BL01C Experimental Station.....  | 49 |
| Figure 3.6 Setup of typical Raman and PL measurements.....  | 50 |
| Figure 4.1 XRD patterns of $\text{Er}^{3+}$ -doped PLT films with 7 mol% $\text{Er}^{3+}$ doping at various sintering temperatures and with different $\text{Er}^{3+}$ concentrations at sintering temperature 950°C.....   | 55 |
| Figure 4.2 The ratio of lattice constants $c/a$ after Rietveld refinement and the FWHM  |    |

|   |    |
|---|----|
| of (100) with different $\text{Er}^{3+}$ concentrations at sintering temperature 950°C.....   | 57 |
| Figure 4.3 Dependence of the green emission intensities of $\text{Er}^{3+}$ -doped PLT films on $\text{Er}^{3+}$ concentrations and sintering temperature.....  | 59 |
| Figure 4.4 Raman spectra of $\text{Er}^{3+}$ -doped PLT films with different $\text{Er}^{3+}$ concentrations at sintering temperature 950°C and with 7 mol% $\text{Er}^{3+}$ dopant at various sintering temperatures.....  | 61 |
| Figure 4.5 Schematic representation of the position of B atom in $\text{ABO}_3$ structure.....  | 63 |
| Figure 5.1 UC fluorescence spectra of (a) $\text{PbTiO}_3$ , (b) $\text{BaTiO}_3$ , and (c) $\text{SrTiO}_3$ doped with 6 mol% $\text{Er}^{3+}$ ions and various concentrations of $\text{Yb}^{3+}$ ions under the same pump power of 980 nm diode laser at 107 mW..... | 69 |
| Figure 5.2 XRD patterns of $\text{PbTiO}_3$ and $\text{BaTiO}_3$ doped with 6 mol% $\text{Er}^{3+}$ ions and various concentrations of $\text{Yb}^{3+}$ ions.....   | 73 |
| Figure 5.3 Rietveld pattern of $\text{PbTiO}_3$ doped with only 6 mol% $\text{Er}^{3+}$ ions and 6 mol% $\text{Yb}^{3+}$ ions.....  | 74 |
| Figure 5.4 $c/a$ ( $a$ and $c$ are lattice constants) ratio as function of $\text{Yb}^{3+}$ - ion concentrations after Rietveld refinement.....   | 74 |
| Figure 5.5 Pump power dependence of the red upconversion emission of $\text{PbTiO}_3$ and $\text{BaTiO}_3$ doped with 6 mol% $\text{Er}^{3+}$ ions and various concentrations of $\text{Yb}^{3+}$ ions in a logarithmic scale.....                                      | 76 |
| Figure 6.1 Microstructure (FESEM) of $\text{BaTiO}_3$ nanoparticles with average grain size of $140 \pm 8$ nm, $60 \pm 6$ nm, and $30 \pm 5$ nm.....  | 83 |
| Figure 6.2 Rietveld pattern of $\text{BaTiO}_3$ nanoparticles with average grain size of 60 nm .....  | 84 |
| Figure 6.3 The lattice constants $a$ and $c$ of $\text{BaTiO}_3$ nanoparticles after Rietveld   |    |

|   |     |
|---|-----|
| refinement procedure and the ratio of $c/a$ (b).....  | 86  |
| Figure 6.4 Size dependence of Raman spectra for BaTiO <sub>3</sub> bulk ( $> 1$ m) and nanoparticles of diameter 140, 60, and 30nm, respectively.....   | 88  |
| Figure 6.5 Structural model of the cubic- and tetragonal-phase occurring with bulk BaTiO <sub>3</sub> crystals.....   | 89  |
| Figure 6.6 The fitted parameters using the coupled-phonon model as a function of particle size. ....  | 93  |
| Figure 6.7 The LO-TO splitting of the $A_1(\text{LO}_3)$ and $A_1(\text{TO}_1)$ modes as function of particle size.....   | 96  |
| Figure 6.8 Normalized square difference of phonon frequencies of $A_1(\text{LO}_3)$ and $A_1(\text{TO}_1)$ and normalized reciprocal of unit cell volume for nanometer size samples to the micrometer size.....   | 96  |
| Figure 7.1 Schematic illustration of three thin films with different connectivity schemes: the 0-3 type with CFO particles embedded in PTO matrix, the 2-2 type with CFO and PTO nanolayers, and the disk-3 type with CFO disc aligned in PTO matrix..... | 103 |
| Figure 7.2 Top view of FESEM and OM images of the disk-3 type showing the CoFe <sub>2</sub> O <sub>4</sub> disks in the PbTiO <sub>3</sub> matrix.....  | 103 |
| Figure 7.3 X-ray diffraction patterns of the 2-2, 0-3, and disk-3 multiferroics together with those of, pure CFO powder, pure PTO powder, and PTO on Pt/Si film for comparison.....   | 104 |
| Figure 7.4 Hysteresis loops of out-of-plane and in-plane magnetization for the pure CFO, 0-3, 2-2, and disk- samples.....   | 109 |
| Figure 7.5 Micro Raman spectra of disk-3, 2-2, 0-3 multiferroics together with those of PTO on Pt/Si, and PTO powder for comparison.....  | 113 |

Figure 7.6 The fitted Raman shift of the  $A_1(TO_3)$ ,  $A_1(TO_2)$ , and  $A_1(TO_1)$  modes as a function of film type.....116

Figure 8.1 SEM images of the three-series products: BT-1, BT-2, and BT-3...125



## List of Tables

|   |     |
|---|-----|
| Table 6-1 Refined crystal parameters and reliability factors of BaTiO <sub>3</sub> nanoparticles.....           | 85  |
| Table 7-1 The refined lattice parameters of PTO for the pure PTO powder and the films with different types..... | 105 |
| Table 7-2 The refined lattice parameters of CFO for the films with different types.....                         | 105 |



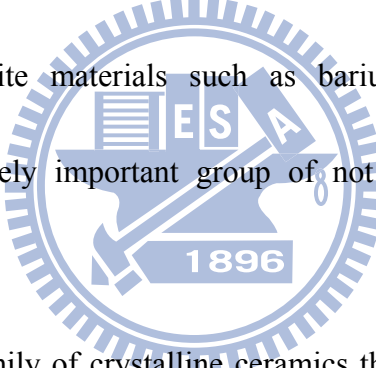
# Chapter 1 Introduction

## 1.1 Ferroelectricity, Photorefractive effect, and Perovskites

Ferroelectricity is a spontaneous electric polarization of a material that can be reversed by the application of an external electric field, upon cooling the material below a certain temperature called the Curie temperature. Ferroelectric ceramics were born in the early 1940s with the discovery of the phenomenon of ferroelectricity with high dielectric constant in barium titanate ( $\text{BaTiO}_3$ ). Ferroelectric materials have long been used in bulk forms in variety of fields such as ceramic capacitors. Furthermore, ferroelectric materials in the forms of thin films are essential for variety of devices such as ferroelectric random access memory (FRAM), infrared pyroelectric sensors, transistors, microwave electronics, electro-optic modulators, and in other integrated devices. Among the many classes of ferroelectric materials, the perovskite compounds such as lead lanthanum titanate (PLT) [1], lead zirconate titanate (PZT) [2], lead titanate (PTO) [3], and barium titanate (BTO) [4] have been the most intensively investigated.

Because of the beneficial properties of light such as wide bandwidth and high speed switching, photonic devices have the trend to replace electronic ones when they are available. Photorefractive materials particularly offer many fascinating

possibilities for applications in the development of communication networks and volume holographic memories [5]. The photorefractive effect is a phenomenon whereby the local refraction index is modified by spatial variations of the light intensity. When two coherent rays interfere with each other in a photorefractive material to forms a spatially varying pattern of illumination, charge carriers will be produced in the material and migrate owing to drift or diffusion and space charge separation effects. The resulting electric field from charge separation induces a refractive index change via the electro-optic effect. Owing to the large electro-optic effect present in perovskite materials such as barium titanate, the perovskite compounds are an extremely important group of not only ferroelectric but also photorefractive materials.



**Perovskites** are a large family of crystalline ceramics that derive their name from a specific mineral known as perovskite. The parent material, perovskite, was first described in the 1830's by a geologist Gustav Rove, who named it after the famous Russian mineralogist Count Lev Aleksevich von Perovski. The general formula of perovskite oxides is  $ABO_3$  (see Fig. 1.1), which is composed of three distinct chemical elements in the ratio of 1:1:3. Ideal oxide perovskite of the aristotype assumes cubic group  $Pm\bar{3}m$  with atom positions of cation "A" at  $(1/2, 1/2, 1/2)$  of Wyckoff position 1a, cation "B" at  $(0, 0, 0)$  of Wyckoff position 1b, and anions "O" at

(1/2, 1/2, 0), (1/2, 0, 1/2) and (0, 1/2, 1/2) of Wyckoff position 3d. The cation “A” is usually larger than vation “B” in the perovskite oxide structure and the “A” and “B” sites are normally occupied by “+2” and “+4” ions, respectively. Conventionally, two types of unit cells with (1) A-cation and (2) B-cation located at center are adopt and often termed the A-cell and B-cell. For type A-cell, the corner-sharing  $\text{BO}_6$  octahedra where A-cation is located in the cubo- octahedral interstice of coordination number CN=12 is easily visualized. On the other hand, B-cation of CN=6, forming  $\text{BO}_6$  octahedron with six oxygen ions, is situated at the octahedral interstice. The configurations of two types of unit cells are illustrated schematically in Fig. 1.1(a) for A-cell type and Fig. 1.1(b) for B-cell type [Galasso 1970]. B-cell type unit cell has adopted recently since it clearly represents the  $\text{BO}_6$  octahedra from whose distortion the ferroelectricity in t- $\text{BaTiO}_3$  and other ferroic properties, e.g. ferroelasticity, ferromagnetism are derived. Take cubic- $\text{ABO}_3$  ( $Pm\bar{3}m$ ), the 3C-polytype, to exemplify how perovskite structure is constructed is illustrated schematically in Fig. 1.1(c). Its crystal structure designated to E2<sub>1</sub> using Strukturbericht symbols may be derived in the way from either  $\alpha$ - $\text{ReO}_3$  (D0<sub>9</sub>),  $\alpha$ - $\text{Cu}_3\text{Au}$  (L1<sub>2</sub>) or  $\text{CsCl}$  (B2). When  $\text{A}^{2+}$  is inserted into D0<sub>9</sub> at eight corner sites, the structure becomes perovskite B-cell type. Similarly, removing “A” from B-cell type, the structure becomes  $\text{ReO}_3$  with all A-site vacant. Removing “B” from B-site of B-cell type, the crystal

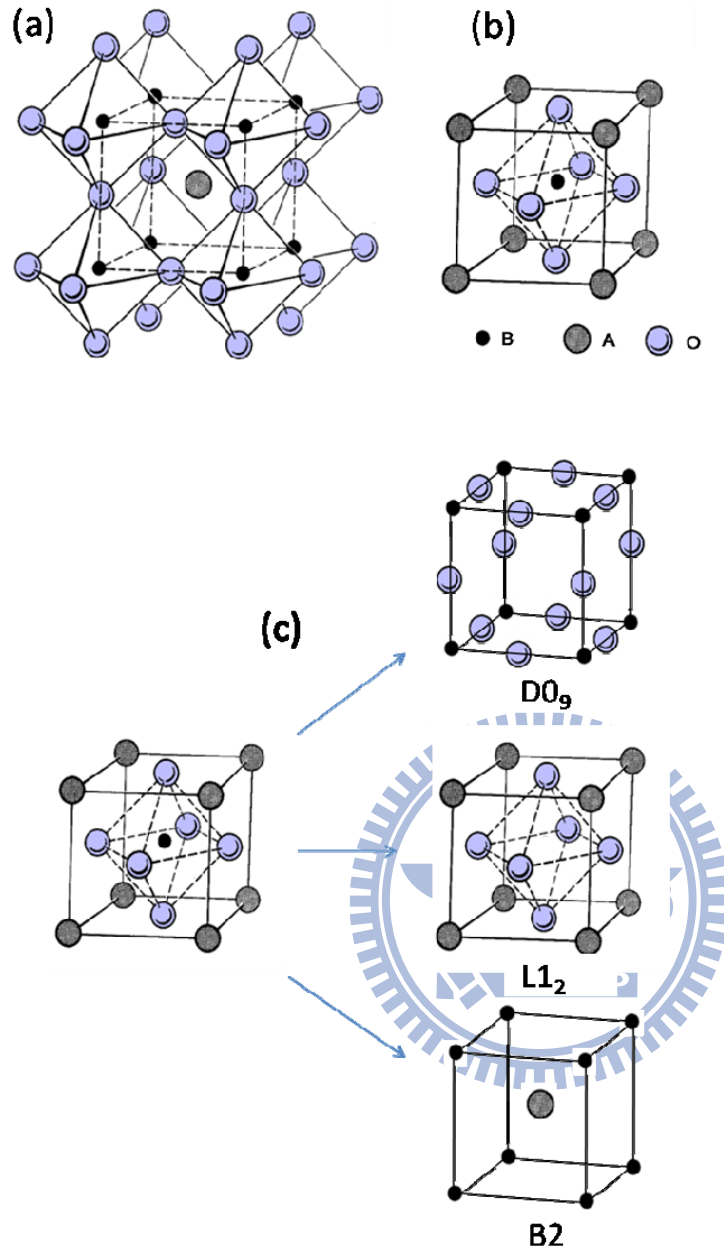
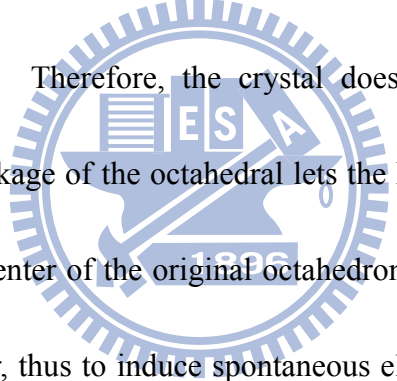


Figure 1.1: Schematic illustrations for A-cell and B-cell types of unit cell for cubic-ABO<sub>3</sub> and possible alternative ways to derive cubic-ABO<sub>3</sub> structure. [Galasso 1970].

structure becomes ordered fcc  $\alpha$ -Cu<sub>3</sub>Au (L1<sub>2</sub>). And then, by removing O<sup>2-</sup> from B-cell type, the structure perovskite is reduced to ordered bcc CsCl (B2). The atomic structure of perovskite is very sensitive to the alteration in the temperature of

the crystal. As the temperature changes, the crystallographic dimensions change and the crystal structures of  $\text{ABO}_3$  include cubic, tetragonal, orthorhombic, and rhombohedral due to distortion of the  $\text{BO}_6$  octahedra[6]. According to Landau free energy [Putnis 1992], the phase transition is discontinuous first-order in nature. All of the ferroelectric materials have a transition temperature called the Curie temperature ( $T_c$ ). When the crystal temperature goes above the Curie temperature,  $T > T_c$ , the elongated crystallographic dimensions allow the B cation to sit at the center of  $\text{BO}_6$  skeleton. In this case, the crystal structure is cubic with no spontaneous or permanent electric dipole. Therefore, the crystal doesn't exhibit ferroelectricity.



While for  $T < T_c$ , the shrinkage of the octahedral lets the B cation be more energized to move farther from the center of the original octahedron. Shifting of the B cation causes the structure to alter, thus to induce spontaneous electric dipole. As a result, the distorted octahedra are coupled together, and a very large spontaneous polarization can be achieved. This large spontaneous polarization will lead to a large dielectric constant highly sensitive to temperature. It possesses ferroelectricity in this non-cubic crystal structure and is called ferroelectric phase. A ferroelectric crystal undergoes a phase transition from a non-ferroelectric phase to a ferroelectric phase on decreasing the temperature through the Curie point. The structure of perovskite is also sensitive to A cation substitutions [7-9] and the behavior is similar

to the alteration in the temperature of the crystal.

## 1.2 Ferromagneticity and Spinel

The spin of an electron combined with its orbital angular momentum results in a magnetic dipole moment and creates a magnetic field. But, the total dipole moment of all the electrons in many materials which have a filled electron shell is zero. Only atoms with partially filled shells can undergo a net magnetic moment in the absence of an external field. Ferromagnetic materials contain many atoms with unpaired spins. When the tiny magnetic dipoles are aligned in the same direction, they create a measurable macroscopic field. These magnetic dipoles tend to align in parallel to an external magnetic field, an effect called **paramagnetism** (see Fig. 1.2(a)). A related but much weaker effect is **diamagnetism** (see Fig. 1.2(b)), due to the orbital motion induced by an external field, resulting in a dipole moment opposite to the applied field. Ferromagnetism involves an additional phenomenon---the dipoles tend to align spontaneously even without any applied field (see Fig. 1.2(c)). This is a purely quantum-mechanical effect. According to the classical electromagnetism, two nearby magnetic dipoles will tend to align in opposite directions. However, they tend to align in the same direction because of the Pauli exclusive principle: two electrons with the same spin cannot sit at the same "position", which effectively

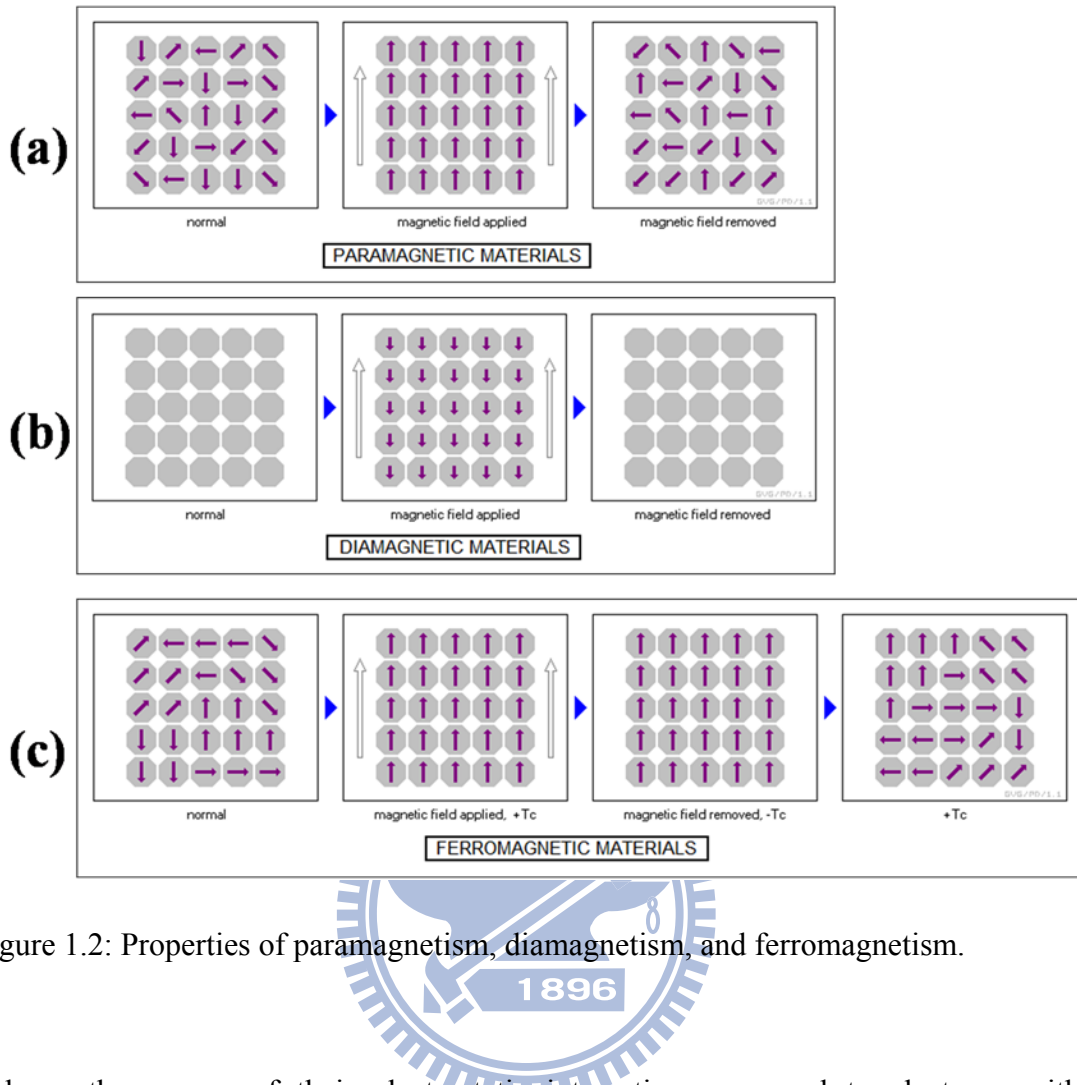


Figure 1.2: Properties of paramagnetism, diamagnetism, and ferromagnetism.

reduces the energy of their electrostatic interaction compared to electrons with

opposite spin. This difference in energy is called the exchange energy.

The exchange interaction is primarily responsible for the ordering of atomic moments occurring in magnetic solids and for two other major magnetic ordering types, antiferromagnetism and ferrimagnetism. For instance, in iron (Fe) the exchange interaction between two atoms is about 1000 times stronger than that of classical interaction. There are a small number of "exotic" ferromagnets in which the exchange interactions are exceptionally weak, and then the classical dipole-dipole

interaction may become the dominant ones. However, such systems become ferromagnetic only at very low temperature, usually below 1 K. But if the Curie point in a given material is higher than a few kelvins, then its ferromagnetism is surely produced by exchange interaction. In such systems the classical dipole-dipole interaction may only give rise to secondary effects.

For the long range, the advantage of exchange energy is overtaken by the classical tendency of dipoles to anti-align. This is why, in an equilibrated ferromagnetic material, the dipoles in the whole material are not aligned. Rather, they organize into magnetic domains (also known as Weiss domains) that are aligned at short range, but at long range adjacent domains are anti-aligned. The boundary between two domains, where the magnetization flips, is called a domain wall (i.e., a Bloch/Néel wall, depending upon whether the magnetization rotates parallel/perpendicular to the domain interface) and is a gradual transition on the atomic scale.

Thus, an ordinary piece of iron generally has little or no net magnetic moment. However, if it is placed in a strong enough external magnetic field, the domains will re-orient in parallel with that field, and will remain re-oriented when the field is turned off, thus creating a "permanent" magnet. The domains don't go back to their original minimum energy configuration when the field is turned off because the

domain walls tend to become 'pinned' or 'snagged' on defects in the crystal lattice, preserving their parallel orientation. This is shown by the Barkhausen effect: as the magnetizing field is changed, the magnetization changes in thousands of tiny discontinuous jumps as the domain walls suddenly "snap" past defects. This magnetization as a function of the external field is described by a hysteresis curve.

Although this state of aligned domains is not a minimal-energy configuration, it is extremely stable and has been observed to persist for millions of years in seafloor magnetite aligned by the Earth's magnetic field. Alloys used for the strongest permanent magnets are "hard" alloys made with many defects in their crystal structure where the domain walls "catch" and stabilize. The net magnetization can be destroyed by heating and then annealing the material without an external field, however. The thermal motion allows the domain boundaries to move, releasing them from any defects to return to their low-energy unaligned state.

As the temperature increases, thermal motion and entropy competes with the ferromagnetic tendency for dipoles to align. When the temperature rises beyond a certain point, called the Curie point, there is a second-order phase transition and the system can no longer maintain a spontaneous magnetization, although it still responds paramagnetically to an external field. Below that temperature, there is a spontaneous symmetry breaking and random domains form. The Curie temperature itself is a

critical point, where the magnetic susceptibility ( $\chi$ ) is theoretically infinite and, although there is no net magnetization, domain-like spin correlations fluctuate at all length scales.

Spinel is an important class of mixed-metal oxides, which has the general chemical composition of  $AB_2O_4$ . Atom “A” is a divalent ion of radius between 80 and 110 pm, such as Fe, Mn and Cu; atom “B” is a trivalent atom of radius between 75 and 90 pm, such as Ti, Fe and Co. The majority of spinel compounds belong to the space group  $Fd\bar{3}m$  ( $F_{1/d}^4\bar{3}_{2/m}$ ;  $O_h^7$ ; No. 227 in the International Tables). The structure consist of a cubic close-packed array of 32 oxygen ions, which forms 64 tetrahedral interstices and 32 octahedral interstices in one unit cell (containing eight formula units  $(AB_2O_4)_8$ ) [10]. In a normal spinel structure, e.g.  $MgAl_2O_4$ , all the

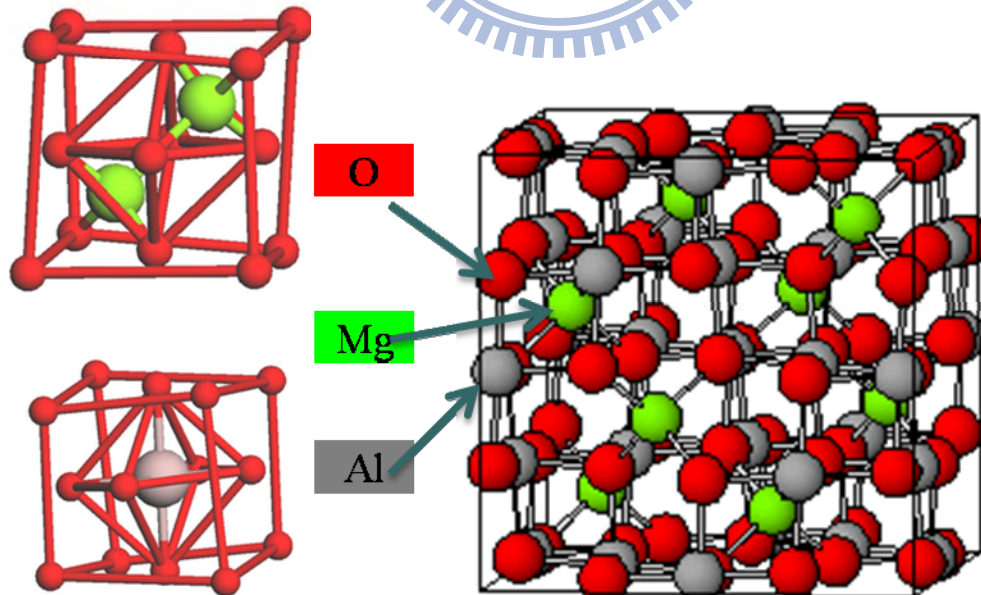


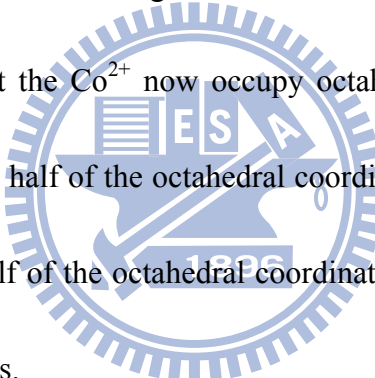
Figure 1.3: Arrangement of atoms within the  $MgAl_2O_4$  unit cell.

trivalent cations ( $Al^{3+}$ ) are located in half the octahedral sites, while all the divalent cations ( $Mg^{2+}$ ) occupy 1/8 of the tetrahedral sites. Figure 1.2 shows a typical spinel structure. Notice the red oxygen atoms, the green “A” atoms are in the tetrahedral holes, and the grey “B” atoms in the octahedral holes.

Cobalt ferrite,  $CoFe_2O_4$  (CFO), has an inverse spinel structure. The normal crystal structure of an  $AB_2O_4$  spinel consists of the  $A^{2+}$  atoms occupying the tetrahedral coordination sites and the  $B^{3+}$  atoms occupying the octahedral sites [11].

An inverse spinel is an alternative arrangement where the divalent ions swap with half of the trivalent ions so that the  $Co^{2+}$  now occupy octahedral sites i.e.  $Fe(CoFe)O_4$ .

The  $Co$  cation occupies one half of the octahedral coordination sites and half the  $Fe^{3+}$  cations occupy the other half of the octahedral coordination sites as well as all of the tetrahedral coordination sites.



### 1.3 Multiferroic materials

**Multiferroics** displaying both ferroelectric and ferromagnetic properties is known possessing the magnetoelectric (ME) effect between the two parameters [12]. The ME effect in multiferroics possesses not only simultaneous magnetic and electric ordering but also interconversion of energies stored in electric and magnetic fields.

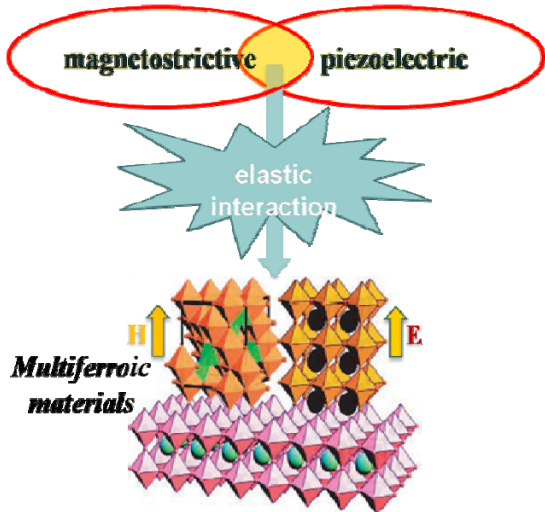


Figure 1.4: Schematic illustration of multiferroic material.

It is also an important mechanism in applications of transducers, actuators, and sensors [13, 14]. There are some theoretical studies [15-17] on calculating the coupling effect of different geometric structures and many experimental reports [13, 18] of ME effect in various types of materials, different geometric shapes, and operational modes. The coexistence of magnetic and electric subsystems engenders the material with the “product” property (i.e., the composite exhibits responses that are not available in the individual component phases), thus allowing an additional degree of freedom in the design of actuators, transducers, and storage devices. However, the choice of single-phase materials exhibiting coexistence of strong ferro/ferrimagnetism and ferroelectricity is limited [19, 20]. Van Suchtelen et al. [21] proposed that composites of piezoelectric and magnetostrictive phases can be electromagnetically coupled via stress mediation (see Fig. 1.4). The ME coupling

results from the elastic bonding at the interface and is transmitted through the stress/strain exerted by a magnetized magnetostrictive phase on a piezoelectric phase or vice versa along their boundary, hence it induces a net polarization or magnetization [12, 22, 23].

## 1.4 Motive

To develop a solution for integrated modulable devices, study on not only the emission properties of rare-earth (RE)-doped ferroelectric materials but also the various properties of host materials is strongly motivated.

### 1.4.1 Dependence of crystal structure on substitution, size, and shape

The physical properties of complex oxide perovskites have been dramatically influenced by various effects, such as temperature [24-26], pressure [25, 27], substitution [28], size, and shape [29-33]. With the development of miniaturization of electronics, recent advances in solid-state science have resulted in ferroelectric materials and devices with nanostructures with length scales less than 200 nm. The size dependence of Curie temperature and tetragonal distortion of the ferroelectric phase has been investigated theoretically based on the Landau-Ginsburg-Devonshire (LGD) theory in the case of isolated particles.[34-37] The change of the ferroelectric phase in isolated particles is mainly the consequence of the surface effect and a transition from the ferroelectric phase to a cubic paraelectric phase at room

temperature for a critical particle size from a few nanometers to a few tens of nanometers is predicted. However, it is often difficult in experiment to separate true size effects from other factors that change with the size. The fixity of the ferroelectric phase can be determined by additional factors like defect chemistry, incorporation of foreign atoms and bulk hydroxyl groups, aggregation level of the particles, porosity level, and residual stresses.[\[38-43\]](#) To avoid the disturbance of other causes, powders with uniform size therefore seems a more convenient system to study size effects. In this part, we synthesize BaTiO<sub>3</sub> nanocrystals with uniform crystal size less than 200 nm by using glycothermal synthesis method. We probe the size dependence of structure characterization with crystal size ranging from  $\sim\mu\text{m}$  to  $\sim 10$  nm by using the x-ray diffraction (XRD), scanning Electron microscope (SEM) and Raman scattering. The research topic will focused on the behavior of phonon modes, including the displacement of B cation and the coupling of phonon, as the crystal size decreases from  $\sim\mu\text{m}$  to  $\sim 10$  nm. We also attempt to synthesize BaTiO<sub>3</sub> nano-wires (nano-rods) by using molten-salt synthesis method.

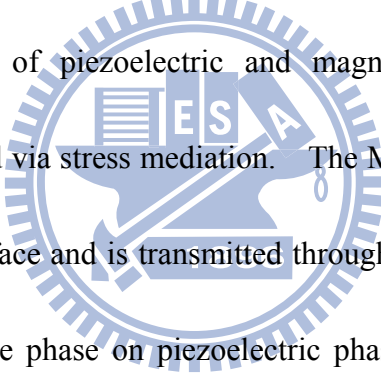
#### **1.4.2 Dependence of mechanism of luminescence on crystal structure in rare-earth ions doped materials**

The different crystal field caused by structure symmetry of the host material would contribute to different perturbation terms for the rare-earth ions inner shell

transitions. Therefore, the crystal structure is a more important mechanism for not only emission efficiency in erbium-doped  $\text{Pb}_{0.8}\text{La}_{0.2}\text{TiO}_3$  system, but also converting up-conversion (UC) green radiation to red radiation due to the EBT process in Er-Yb codoped ferroelectrics. In this part, we have studied the dependence of emission mechanism on the crystal structure of perovskites doped with rare-earth ions.

#### 1.4.3 Dependence of coupling of electricity and magnetism on lattice mismatch

Multiferroics displaying both ferroelectric and ferromagnetic properties is known possessing the ME effect between the two parameters. Van Suchtelen et al. [21]



proposed that composites of piezoelectric and magnetostrictive phases can be electromagnetically coupled via stress mediation. The ME coupling results from the elastic bonding at the interface and is transmitted through the stress/strain exerted by magnetized magnetostrictive phase on piezoelectric phase or vice versa along their boundary and hence it induces a net spontaneous polarization or magnetization [12, 22, 23].

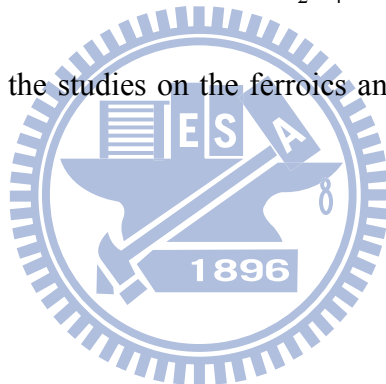
Moreover, it is well known that the behavior of interfacial phonon is sensitive to the giant residual stress/strain resulting from the lattice misfit between the different media [44]. It is interesting and important to investigate the relationship between the ME effect and the behavior of interfacial phonon. Recent studies on phonon behavior of multiferroics were reported [45-47], but the results are inconclusive. In this part, we report on the stress dependence of the behavior of interfacial phonon and

the magnetic properties in three multiferroics consisting of the different geometric shapes of ferromagnetic  $\text{CoFe}_2\text{O}_4$  (CFO) embedded in ferroelectrics  $\text{PbTiO}_3$  (PTO) by using the micro-Raman spectroscopy and superconducting quantum interference device (SQUID).

## 1.5 Organization of this dissertation

In this thesis, I present investigations of the influence of perovskite structure on luminescence and characteristics of ferroics. The dissertation is organized as follows. I first describe the related theoretic background in Chapter 2, including a general concept of crystal structures, lattice dynamics, fundamental optical transitions, and magnetolectric (ME) effect. In Chapter 3, I present the synthesis of the samples with different processes and also show the brief illustrations of characterization techniques. In Chapter 4, I discuss the dominant mechanisms on visible emission of the  $\text{Er}^{3+}$  doped  $\text{Pb}_{0.8}\text{La}_{0.2}\text{TiO}_3$  polycrystalline films. Combining with examining the disappearance of Raman modes, I show destruction to a displacement of Ti in the short-range structure for doping concentration exceeding 7 mol%. The diminishing of symmetry breaking causes quench of  $\text{Er}^{3+}$  emission. As increasing  $\text{Yb}^{3+}$  co-doped concentrations in 6 mol%  $\text{Er}^{3+}$  doped  $\text{PbTiO}_3$ ,  $\text{BaTiO}_3$ , and  $\text{SrTiO}_3$  polycrystalline powder samples, the dominant mechanisms of visible upconversion emissions in Er-Yb codoped ferroelectrics are discussed in Chapter 5. In Chapter 6, I discuss the

attractive LO-TO splitting behavior and depict the low frequency TO spectral peak along with change of the tetragonal phase toward the cubic one for reducing diameter of BaTiO<sub>3</sub> nanocrystals from 140 nm to 30 nm. In Chapter 7, I discuss the characteristics of three different geometric forms of the PbTiO<sub>3</sub>-CoFe<sub>2</sub>O<sub>4</sub> multiferroics. The analysis of the magnetic and Raman measurements under different geometric forms indicates the dependence of magnetic property and interfacial phonon behavior on stress/strain due to the lattice misfit and the strongest chemical bonding at the interface between CoFe<sub>2</sub>O<sub>4</sub> and PbTiO<sub>3</sub> matrices. In the final Chapter 8, I conclude the studies on the ferroics and propose the several topics worthy of the future work.



## References

[1] S. Bhaskar, S. B. Majmder, P. S. Dobal, R. S. Katiyar, and S.B. Krupanidhi, *J. Appl. Phys.* 89, 5637 (2001).

[2] J. Cheng and Z. Meng, *Thin Solid Films* 385, (2001).

[3] C. H. Wang and D. J. Choi, *J. Am. Ceram. Soc.* 84, 207 (2001).

[4] H. Kumazawa and K. Masuda, *Thin Solid Films* 353, 144 (1999).

[5] D. Psaltis and F. Mok, *Sci. Am.* 11, 52 (1995).

[6] C. N. R. Rao and K. J. Rao: *Phase Transitions in Soild* (Megrqw-Hill International Book Company, 1978).

[7] S.Y. Kuo, W.Y. Liao, and W.F. Hsieh, *Phys. Rev. B* 64, 224103 (2001)

[8] S.Y. Kuo, C.T. Li, and W.F. Hsieh, *Appl.Phys. Lett.* 81, 3019 (2002)

[9] S.Y. Kuo, C.T. Li, and W.F. Hsieh, *Phys. Rev. B* 69, 184104 (2004)

[10] W. Gary, *Inorganic Chemistry*, University Science Books, 691 (2000).

[11] *Modern Ferrite Technology: Crystal structures of Ferrites*, 52-69.

[12] H. Zheng, J. Wang, S. E. Lofland, Z. Ma, L. Mohaddes-Ardabili, T. Zhao, L. Salamanca-Riba, S. R. Shinde, S. B. Ogale, F. Bai, D. Viehland, Y. Jia, D. G. Schlom, M. Wuttig, A. Roytburd, and R. Ramesh, *Science* 303, 661-663 (2004).

[13] C. W. Nan, M. I. Bichurin, S. X. Dong, D. Viehland, G. and Srinivasan, *J. Appl. Phys.* 103, 031101 (2008).

[14] J. F. Scott, *Nat. Mater.* 6, 256-257 (2007).

[15] V. M. Petrov, G. Srinivasan, M. I. Bichurin, and A. Gupta, *Phys. Rev. B* 75, 224407 (2007).

[16] C. Q. Liu, W. D. Fei, and W. L. Li, *J. Phys. D-Appl. Phys.* 41, 125404 (2008).

[17] C. K. Wong and F. G. Shin, *J. Phys. D-Appl. Phys.* 41, 135002 (2008).

[18] J. Zhai, Z. Xing, S. Dong, J. Li, and D. Viehland, *J. Am. Ceram. Soc.* 91, 351-358 (2008).

[19] F. A. Smolenskii, I. E. Chupis, *Sov. Phys. Usp.* 25, 475 (1982).

[20] J. Wang et al., *Science* 299, 1719 (2003).

[21] J. Van Suchtelen, *Philips Res. Rep.* 27, 28 (1972).

[22] J. G. Wan, X. W. Wang, Y. J. Wu, M. Zeng, Y. Wang, H. Jiang, W. Q. Zhou, G. H. Wang, and J. M. Liu, *Appl. Phys. Lett.* 86, 122501 (2005).

[23] C. W. Nan, G. Liu, Y. H. Lin, and H. Chen, *Phys. Rev. Lett.* 94, 197203 (2005).

[24] R. Pirc and R. Blinc, *Phys. Rev. B* 70, 134107 (2004).

[25] J. Iguez and D. Vanderbilt, *Phys. Rev. Lett.* 89, 115503 (2002).

[26] D. Damjanovic, F. Brem, and N. Setter, *Appl. Phys. Lett.* 80, 652 (2002).

[27] U. D. Venkateswaran, V. M. Naik, and R. Naik, Phys. Rev. B 58, 14256 (1998).

[28] S. Y. Kuo, W. Y. Liao, and W. F. Hsieh Phys. Rev. B 64, 224103 (2001).

[29] M. H. Frey and D. A. Payne, Phys. Rev. B 54, 3158 (1996).

[30] S. Tsunekawa, S. Ito, T. Mori, K. Ishikawa, Z. Q. Li, and Y. Kawazoe1, Phys. Rev B 62, 3065 (2000).

[31] Z. Zhao, V. Buscaglia, M. Viviani, M. T. Buscaglia, L. Mitoseriu, A. Testino, M. Nygren, M. Johnsson, and P. Nanni, Phys. Rev. B 70, 024107 (2004).

[32] T. Hoshina, H. Kakemoto, T. Tsurumi, S. Wada, and M. Yashima, J. Appl. Phys. 99, 054311 (2006).

[33] M. Yashima, T. Hoshina, D. Ishimura, S. Kobayashi, W. Nakamura, T. Tsurumi and S. Wada, J. Appl. Phys. 98, 014313 (2005).

[34] C. L. Wang, and S. R.P. Smith, J. Phys.:Condens. Matter 7, 7163 (1995)

[35] S. Li, J. A. Eastman, Z. Li, C.M. Foster, R. E. Newnham, and L. E. Cross, Phys. Lett. A 212, 341 (1996)

[36] B. Jiang, and L. A. Bursill, Phys. Rev. B 60, 9978 (1999)

[37] H. Huang, C. Q. Sun, and P. Hing, J. Phys.: Condens. Matter 12, L127 (2000).

[38] E. K. Akdogan, M. R. Leonard, and A. Safari, in Handbook of Low and High Dielectric Constant Materials and Their Applications, edited by H. S. Nalwa (Academic Press, San Diego, 1999), Vol. 2, p. 61.

[39] K. Ishikawa, K. Yoshikawa, and N. Okada, Phys. Rev. B 37, 5852 (1988);

[40] K. Ishikawa, and T. Uemori, ibid. 60, 11 841 (1999)

[41] S. Tsunekawa, S. Ito, T. Mori, K. Ishikawa, Z.-Q. Li, and Y. Kawazoe, ibid. 62, 3065 (2000).

[42] M. H. Frey and D. A. Payne, Phys. Rev. B 54, 3158 (1996)

[43] X. Li and W.-H. Shih, J. Am. Ceram. Soc. 80, 2844 (1997).

[44] D. S. Fu, T. Ogawa, H. Suzuki, and K. Ishikawa, Appl. Phys. Lett. 77, 1532-1534 (2000).

[45] J. Barbosa, B. G. Almeida, J. A. Mendes, A. G. Rolo, J. P. Araujo, and J. B. Sousa, J. Appl. Phys. 101, 09M101(2007).

[46] N. Ortega, A. Kumar, P. Bhattacharya, S. B. Majumder, and R. S. Katiyar, Phys. Rev. B 77, 014111(2008).

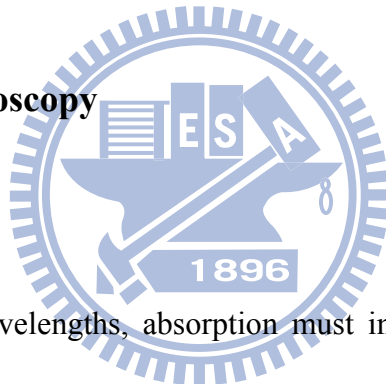
[47] H. M. Zheng, J. Kreisel, Y. H. Chu, R. Ramesh, and L. Salamanca-Riba, Appl. Phys. Lett. 90, 113113(2007).

## Chapter 2 Theoretical Background

In this chapter, lattice vibration in crystals, optical transitions of rare earth, and multiferroic magnetoelectrics are reviewed. Lattice dynamics corresponding to lattice vibrational properties, the behavior of coupled phonon and, the mechanism of LO-TO splitting are discussed. Optical transitions in rare earth doped materials have been described, including the mechanism of fundamental optical transitions and upconversion.

### 2.1 Vibrational spectroscopy

#### 2.1.1 IR absorption



For infra-red (IR) wavelengths, absorption must in some way be related to a variation in the charge distribution. This arises due to a change in the dipole moment associated with molecule. After bonding, one atom of the molecules has a local charge  $\Delta q$  then the rest of atoms have charge  $-\Delta q$  and the dipole moment  $\mu$ , is given by

$$\mu = \Delta q \times l \quad (2-1)$$

where  $l$  is the separation of the charges (see Figure 2.1).



Figure 2.1: Diagram of dipole moment.

Electromagnetic wave can be absorbed or emitted by a medium if during its interaction there is a change in the charge distribution within the medium. During the interaction with photon, the dipole moment  $\mu$  will change, thus one can rewrite the dipole moment as

$$\mu = \mu_0 + \frac{\partial \mu}{\partial Q} Q, \quad (2-2)$$

where  $Q = (r - r_{eqm})$  is the displacement from the equilibrium position “ $r_{eqm}$ ”.

In order to describe the excitation of a molecule from vibrational level,  $v = i$  to  $v = f$ , as shown in Figure 2.2, an interaction Hamiltonian  $H_{int} = E \cdot \mu$  that expresses the interaction of an atom with a photon is added to the unperturbed Hamiltonian  $H_0$  to describe the total Hamiltonian,

$$H = H_0 + H_{int} \quad (2-3)$$

Thus the transition moment,  $R$ , can be written as

$$R = \int \psi_i H_{int} \psi_f = \langle i | H_{int} | f \rangle, \quad (2-4)$$

so,

$$R = \langle i \left| \left( \mu_0 + Q \frac{\partial \mu}{\partial Q} \right) \cdot E \right| f \rangle = \langle i \left| Q \frac{\partial \mu}{\partial Q} \cdot E \right| f \rangle \quad (2-5)$$

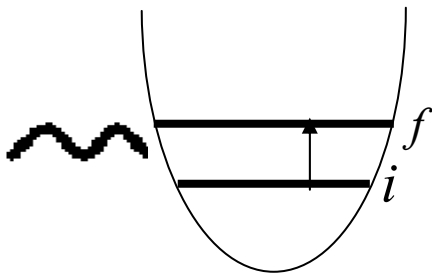
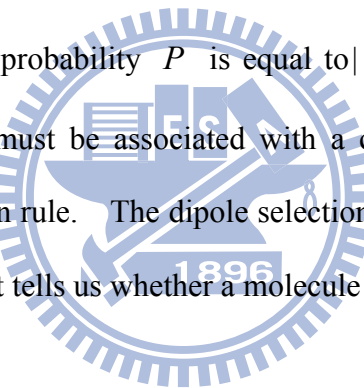


Figure 2.2: Transition from level  $i$  to  $f$ .

IR absorption occurs as the transition  $R \neq 0$ , in other words, there must be a change in the dipole moment due to vibration of the molecule which is induced by the applied field  $E$ , since the transition probability  $P$  is equal to  $|R|^2$ . The condition that an IR absorption or emission must be associated with a change in dipole moment is known as the dipole selection rule. The dipole selection rule plays an important role in IR spectroscopy because it tells us whether a molecule will be IR active or not.



### 2.1.2 Raman scattering

When light passes through a medium, most of the light is reflected, transmitted, absorbed, elastic or inelastic scattered. Raman scattering is an inelastic scattering process. When the light encounters the medium, it interacts inelastically with phonon (vibration) modes and produces outgoing photons whose frequencies are relatively shifted by an amount of energy correspondent to phonon energy from that of the incoming light. The scattered outgoing photons are called the Raman-scattered photons. If the light of frequency  $v_0$  is scattered by some media, the spectrum of the scattered light contains a strong line of frequency  $v_0$  and much

weaker lines of frequencies  $\nu_0 - \Delta\nu_1$ ,  $\nu_0 - \Delta\nu_2$ , ...,  $\nu_0 + \Delta\nu_2$ ,  $\nu_0 + \Delta\nu_1$ , etc. Those lines on the low frequency side of the exciting lines (i.e.,  $\nu_0 - \Delta\nu_i, i = 1, 2, \dots$ ) are always matched by lines on the high frequency side (i.e.,  $\nu_0 + \Delta\nu_i, i = 1, 2, \dots$ ) but the latter are much weaker when the scattering medium is at room temperature. Raman scattering is inherently a weak process, but laser provides enough intensity that the spectra can be routinely measured. In analogy with terms used in the discussion of fluorescence spectra, lines on the low frequency side of the exciting line are known as Stokes lines and those on the high frequency side as anti-Stokes lines.

The incident photon loses its energy by producing a phonon (Stokes shifted), or gain energy and momentum by absorbing a phonon (anti-Stokes shifted), according to the energy conservation rules :

$$h\nu_i + W_1 = h\nu_s + W_2, \quad (2-6)$$

$$h(\nu_s - \nu_i) = h\Delta\nu = W_1 - W_2, \quad (2-7)$$

where  $\nu_i$  and  $\nu_s$  are the incoming and scattered photon frequencies,  $W_1$  and  $W_2$  are the energy of the molecule before and after the interaction, respectively.

Assuming that the scattering medium is in temperature equilibrium at temperature  $T$ , the distribution of the molecules over the energy states will be Boltzmann and the ratio of the number of molecules  $N_1$  in a state of energy  $W_1$  to the number of molecules  $N_2$  in a state of energy  $W_2$  is given by

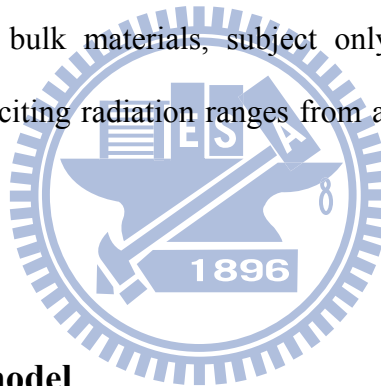
$$\frac{N_1}{N_2} = e^{-h\Delta\nu/kT}, \quad (2-8)$$

if degeneracy is neglected. If one includes the fact that scattered intensity is proportional to the fourth power of the frequency then the relative intensities of

Stokes to anti-Stokes lines and their temperature dependence be consistent with the ratio

$$\frac{I_{\text{anti-Stokes}}}{I_{\text{Stokes}}} = \left( \frac{\nu + \Delta\nu}{\nu - \Delta\nu} \right)^4 e^{-h\Delta\nu/kT} \quad (2-9)$$

All the Raman mode frequencies, intensities, line-shape, and line-width, as well as polarization behavior can be used to characterize the lattice and impurities. The intensity gives information on crystallinity. The line-width increases when a material is damaged or disordered, because damage or disorder occurs in a material will increase the phonon damping rate or relax the rules for momentum conservation in Raman process. All these capabilities can be used as a judgment for layered microstructure as well as bulk materials, subject only to the limitation that the penetration depth of the exciting radiation ranges from a few hundred nanometers to few micrometers.



## 2.2 Coupled phonon model

The Hamiltonian of an isolated system can always be brought to a diagonal form, which means that any coupling of the quantum states is reducible. Under this assumption, the reflectivity of the crystal with more than one infrared active mode is often quite well reproduced by a formula involving the sum of contributions from independent classical oscillators. However, no system above the temperature 0 K is isolated, for that we have least the blackbody radiation connecting it with the environment. In some notable cases, the Hamiltonian of the system is intrinsically

non-diagonal. The profile of the energy spectrum of such system is not composed of a set of Lorentzian peaks, but contains asymmetric interfering features.

Since the occurrence of coupling in the lattice modes was recognized by Barker and Hopield to explain the infrared reflectivity of some perovskites, a handful of spectral anomalies in data on Raman, Brillouin and neutron scattering were observed and associated with phonon-phonon coupling. Because the coupling phenomenon is a temperature-induced effect, it seems probable that its occurrence will be more frequent in crystal showing other thermal anomalies in the phonon behavior. In fact, most of the crystals undergo a structural phase transition at some temperature not far from where the interference starts to be observable.  $\text{BaTiO}_3$  presents three structural phase transitions, at  $-80$ ,  $0$ , and  $130^\circ\text{C}$ . In the tetragonal phase between  $0$  and  $130^\circ\text{C}$  the dynamics of the crystal is complicated. All the three  $A_1$  modes of vibration are strongly coupled and two of them are heavily damped.

Because the three  $A_1(\text{TO})$  modes are strongly coupled and two of them are heavily damped in the tetragonal phase of  $\text{ABO}_3$ , Sood, [1] and Chaves, *et al.* [2] have considered three coupled  $A_1(\text{TO})$  modes to describe the complicated coupling phenomenon. The Raman intensity of the three coupled modes can be expressed by

$$I(\omega) = A [n(\omega) + 1] \text{Im}[\mathbf{T}^* \mathbf{G} \mathbf{T}], \quad (2-10)$$

where  $A$  is a constant,  $n(\omega)$  is Bose-Einstein factor,  $\mathbf{T}$  is a vector involving Raman

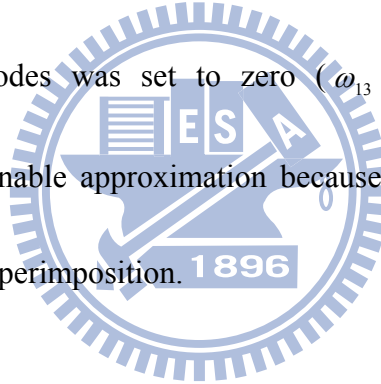
scattering amplitudes, and the inverse matrix response is

$$\mathbf{G}^{-1}(\omega) = \mathbf{\Omega}^2 - \omega^2 \mathbf{I} - i\omega \mathbf{\Gamma}. \quad (2-11)$$

In Eq. (2-11),  $\mathbf{I}$  is the unit matrix,  $\mathbf{\Omega}^2$  is the force constant matrix, and  $\mathbf{\Gamma}$  is the damping matrix:

$$\mathbf{\Omega}^2 = \begin{pmatrix} \omega_1^2 & \omega_{12}^2 & 0 \\ \omega_{12}^2 & \omega_2^2 & \omega_{23}^2 \\ 0 & \omega_{23}^2 & \omega_3^2 \end{pmatrix} \text{ and } \mathbf{\Gamma} = \begin{pmatrix} \Gamma_1^2 & 0 & 0 \\ 0 & \Gamma_2^2 & 0 \\ 0 & 0 & \Gamma_3^2 \end{pmatrix}. \quad (2-12)$$

Here  $\omega_i$  and  $\omega_{ij}$  ( $i, j = 1, 2, 3$ ) are the uncoupled mode frequencies and the coupling strengths between modes  $i$  and  $j$ . The coupling between the lowest ( $\omega_1$ ) and the highest ( $\omega_3$ ) modes was set to zero ( $\omega_{13} = 0$ ), to allow less fitting parameters; this is a reasonable approximation because they are too far from each other, having no spectral superimposition.



## 2.3 Born effective charges and LO-TO splitting

The total polarization in the crystal can be expressed as a sum of contribution from the displacements of the charged ions and from the displacements of electrons relative to their ionic nuclei

$$P^i = P_{ion}^i + P_{electron} \quad (2-13)$$

and

$$P_{ion}^i = \frac{N}{V} \sum_{\alpha} e_{\alpha} U_{\alpha}^i, \quad (2-14)$$

where  $i$  is the label of Cartesian coordinate,  $N$  is the number of primitive cells in the crystal volume  $V$  and  $e_\alpha$  is the charge of the  $\alpha$ th ions in a primitive cell, all ions of the same label suffering the same displacement  $U_\alpha$ .

It is convenient to express the ionic polarization in terms of the normal coordinates. The polarization is a vector, and the vibrational modes that contribute to the polarization are limited to those with the same symmetry character as a polar vector. These polar modes can be chosen so that their contributions to the polarization are parallel to principal axes of the susceptibility tensor. Let  $\xi_\sigma$  be a unit vector parallel to the polarization contributed by the displacement of normal coordinates  $W_\sigma$ . Then one of the Cartesian components  $\xi_\sigma^i$  is unity and the other two are zero. The ionic polarization can be written as

$$P_{ion}^i = \frac{N}{V} \sum_{\sigma} Z_{\sigma} \xi_{\sigma}^i W_{\sigma}, \quad (2-15)$$

$$Z_{\sigma} \xi_{\sigma}^i \equiv \sum_{\alpha} \frac{e_{\alpha} c_{\alpha\sigma}^{i*}}{M_{\alpha}^{1/2}}, \quad (2-16)$$

where  $Z_\sigma$  is the effective charge of the normal mode  $\sigma$  and the mass of the  $\alpha$ th atom is denoted by  $M_\alpha$ . By simplifying equations of motion, we obtain

$$W_{\sigma} = \sum_{\alpha} W_{\alpha}^{1/2} c_{\alpha\sigma}^i U_{\alpha}^i, \quad (2-17)$$

where the transformation coefficients can be chosen to satisfy the orthonormality relations

$$\sum_{\alpha} c_{\alpha\sigma}^{i*} c_{\alpha\sigma'}^i = \delta_{\sigma\sigma'}. \quad (2-18)$$

The presence of an electric field  $E$  modifies the harmonic oscillator equation of the normal modes to

$$\ddot{W}_\sigma + \Gamma_\sigma \dot{W}_\sigma + \omega_\sigma^2 W_\sigma = Z_\sigma \xi_\sigma^i E^i. \quad (2-19)$$

The applied electric field of frequency  $\omega$ , therefore, produces a steady-state normal-mode amplitude,

$$W_\sigma = \frac{Z_\sigma \xi_\sigma^i E^i}{\omega_\sigma^2 - \omega^2 - i\omega\Gamma_\sigma}, \quad (2-20)$$

and the ionic polarization can be written in a form proportional to the electric-field components. We assume that  $\omega$  is in the vicinity of the vibrational frequencies and well below the frequencies of all electric transitions. The relative permittivity is then

$$\kappa^i = \kappa_\infty^i + \sum_\sigma \frac{NZ_\sigma^2 \xi_\sigma^{i2} / \epsilon_0 V}{\omega_\sigma^2 - \omega^2 - i\omega\Gamma_\sigma}, \quad (2-21)$$

where  $\kappa_\infty^i$  is a constant electric contribution to the relative permittivity, so that

$$P_{electron}^i = \epsilon_0 (\kappa_\infty^i - 1) E^i. \quad (2-22)$$

The electric field and polarization of any electromagnetic wave frequency  $\omega$  and wavevector  $q$  will satisfy the Maxwell's equation :

$$-\epsilon_0 c^2 q (q \cdot E) + \epsilon_0 (c^2 q^2 - \omega^2) E = \omega^2 P. \quad (2-23)$$

This equation is unfortunately very complicated in its most general form, but simplification can be made for most applications. The most striking simplification occurs when the frequency and wavevector satisfy  $cq \gg \omega$ . We obtained

$$\kappa^x q^{x^2} + \kappa^y q^{y^2} + \kappa^z q^{z^2} = 0. \quad (2-24)$$

By combining the equation for the divergence of the electrical displacement,

$$q \cdot (\epsilon_0 E + P) = 0, \quad (2-25)$$

with Eqs. (2.23) and (2.24), we can obtain the general representation

$$\ddot{W}_\sigma + \omega_\sigma W_\sigma = -\frac{NZ_\sigma (q \cdot \xi_\sigma) \sum_\tau Z_\tau (q \cdot \xi_\tau) W_\tau}{\epsilon_0 V (\kappa_\infty^x q^{x^2} + \kappa_\infty^y q^{y^2} + \kappa_\infty^z q^{z^2})}, \quad (2-26)$$

where  $\tau$  is summed over all the polar modes. In cubic symmetry crystal, the polar-vector representation is threefold degenerate. The crystals are optically isotropic and the principal axes are not restricted to lie in any particular directions. For any direction of the wavevector of a threefold polar mode, it is permissible to choose two of the polarization vectors  $\xi_\sigma$  perpendicular to  $q$  and the third  $\xi_\sigma$  parallel to  $q$ . The two transverse polar modes have a frequency determined by the standard lattice dynamics calculation. The longitudinal polar mode has the associated macroscopic electric field, and its frequency is determined by the equation above, which reduces to

$$\kappa = 0 \quad (2-27)$$

in the cubic case. The simplest cases to consider first are the cubic crystals that have a single threefold polar mode. The relative permittivity has the isotropic form

$$\kappa = \kappa_\infty + \frac{NZ^2 / \varepsilon_0 V}{\omega_T^2 - \omega^2 - i\omega\Gamma}, \quad (2-28)$$

where the mode frequency  $\omega_0$  is replaced by  $\omega_T$  to emphasize its transverse nature and redundant subscripts and superscripts are omitted. The longitudinal frequency obtained from the equation mentioned above with the damping removed is

$$\omega_L = \left( \frac{\kappa_0}{\kappa_\infty} \right)^{1/2} \omega_T, \quad (2-29)$$

where  $\kappa_0$  is the zero-frequency value of the relative permittivity

$$\kappa_0 = \kappa_\infty + \frac{NZ^2}{\varepsilon_0 V \omega_T^2}. \quad (2-30)$$

This expression for the longitudinal frequency is the Lyddane-Sachs-Teller relation. The equation of motion for the longitudinal mode takes the form

$$\ddot{W} + \omega_T^2 W = -\frac{NZ^2 W}{\varepsilon_0 V \kappa_\infty}, \quad (2-31)$$

and leading to

$$\omega_L^2 = \omega_T^2 + \frac{NZ^2}{\epsilon_0 V \kappa_\infty}. \quad (2-32)$$

Resta *et al.* [3] have shown that polarization is linear in the change of the position vector of the basis atom to a good approximation. The Born effective charge tensor  $Z_m^*$  is rewritten through

$$\delta P = \frac{e}{\Omega} \sum_{m=1}^N Z_m^* \cdot \delta u_m. \quad (2-33)$$

Here,  $N$  is the number of atoms in the primitive unit cell,  $\delta u_m$  is the first-order change of the position vector of the  $m$ th basis atom, and  $\Omega$  is the volume of the unit cell.

The Born effective charge tensor reflects the effects of the Coulomb interactions and is directly related to the LO-TO splitting. The general representation of the dynamical material for LO and TO modes at  $q=0$  are the related by

$$D_{mn}^{LO} = D_{mn}^{TO} + \frac{4\pi e^2}{\Omega} \frac{Z_m^* Z_n^*}{\epsilon_0}, \quad (2-34)$$

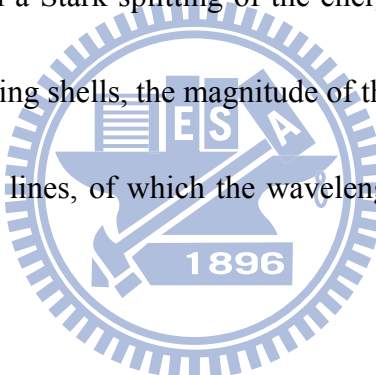
where  $D$  represents the dynamical matrix and is proportional to the square of the vibration frequency. Zhong, *et al.* [4] and Waghmare, *et al.* [5] have calculated that the softest TO mode is most associated with the hardest LO mode via Coulomb interaction to give rise to giant LO-TO splitting in  $\text{ABO}_3$  compounds, especially for the ferroelectric phonon modes.

## 2.4 Optical transitions of rare earth doped materials and

### upconversion

### 2.4.1 Fundamental optical transitions

Trivalent rare-earth (RE) ions are well known for their special optical properties, which result from the fact that the electrons of the partially filled  $4f$ -shell are shielded from the surrounding completely filled  $5s$  and  $5p$  shells. The energy levels of the  $4f$ -shell have equal parity, and hence electric dipole transitions are forbidden. In a solid, the slight mixing with odd-parity wavefunctions makes the transition slightly allowed. The influence of the electric field around the ion removes the degeneracy of the  $4f$ -levels, resulting in a Stark-splitting of the energy levels. However, due to the shielding by the outer lying shells, the magnitude of the splitting is small, resulting in relative narrow emission lines, of which the wavelength is almost independent of the host material.



The energy levels of the  $4f$ -level arise from spin-orbit interactions and are often denoted using Russel-Saunders notation  $^{2S+1}L_J$ , in which  $S$  is the total spin angular momentum,  $L$  is the total orbital angular momentum quantum number and  $J$  the magnitude of the total angular momentum,  $J=L+S$  according to vector model. There exist 14 rare-earth elements, that all have a different number of electrons in the incompletely filled  $4f$ -shell. As a result, each rare-earth ion has its own specific energy levels, and hence typical luminescence lines. The rare-earth ion erbium (Er) has transition at  $1.53 \mu m$ , which is the standard wavelength used in optical

telecommunication. The energy level scheme of trivalent RE ions was presented in the classic work by Dieke and Crosswhite [6] and then was reproduced in many reviews. Figure 2.3 has shown the energy levels and laser transitions of trivalent rare-earth ions.

As already mentioned, the choice of host material in rare-earth doped components does not influence significantly the position of the energy levels of the rare-earth ions.

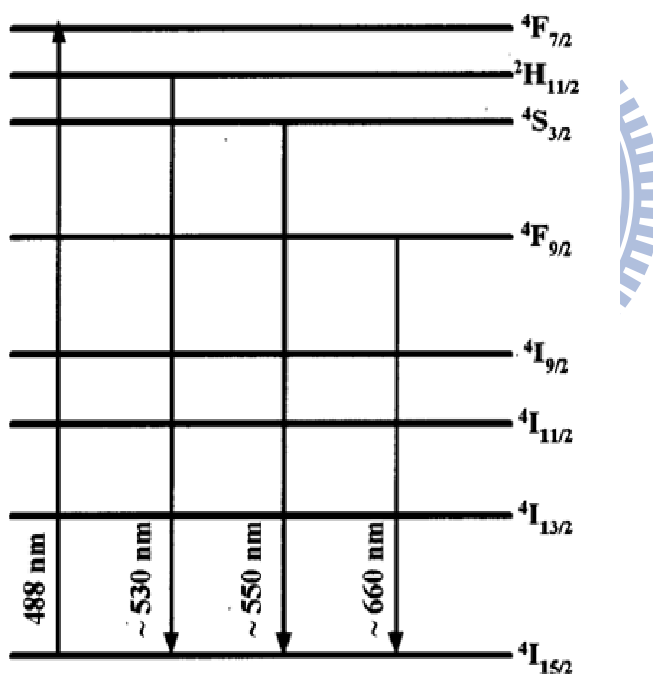


Figure 2.3: Energy level diagram of PLT:Er<sup>+3</sup> thin films [6].

Therefore, in principle any material that little absorption at the pump and emission wavelengths can be used. Many different rare-earth doped materials have been

studied, like pure  $\text{SiO}_2$ , silicate and phosphate glasses,  $\text{LiNbO}_3$ ,  $\text{Al}_2\text{O}_3$ , and  $\text{GaN}$ . By combining the excellent opto-electric properties and chemical stability, ferroelectric perovskite ( $\text{Pb}_{0.7}\text{La}_{0.3}\text{TiO}_3$ ) is being considered in our research.

#### 2.4.2 Upconversion

Upconversion (UC) in rare-earth (RE) ion-doped materials has been intensively studied in recent years of applications in laser devices [7], three-dimensional display [8], sensors [9], and biological fluorescent labels [10-12]. Energy UC of radiation can exist by intra-ionic successive absorption, cooperative energy transfer, and photon avalanche processes [13, 14]. The research of these mechanisms provides intellects on the physics of energy transfer processes and fluorescence converters. Recently, green and red UC radiation induced by a 980-nm diode laser excitation in  $\text{Er}^{3+}$ -doped and  $\text{Er}^{3+}$ — $\text{Yb}^{3+}$  co-doped  $\text{Y}_2\text{O}_3$  and  $\text{ZrO}_2$  nanocrystals were reported [15-17]. It is known that the  $\text{Er}^{3+}$  ion absorbs one laser photon and jumps from the ground state  ${}^4I_{15/2}$  to the long-lived  ${}^4I_{11/2}$  state, which is termed the ground-state absorption (GSA). Then, the excited-state absorption (ESA) could happen to populate  ${}^4F_{7/2}$  state. Subsequently, the  $\text{Er}^{3+}$  ions at  ${}^4F_{7/2}$  state could further rapidly relax to the  ${}^2H_{11/2}$  /  ${}^4S_{3/2}$  state by multiphonon processes, from which the green UC emission arises. Thus, the green UC emission is a result of two-photon excitation (GSA followed by ESA) process. The codoped  $\text{Yb}^{3+}$  ions provide excitation of the  ${}^4I_{11/2}(\text{Er}^{3+})$  state by the

larger absorption cross section of  $\text{Yb}^{3+}$  ions.

The strong red UC emission is reported enabled by quenching the  $^4S_{3/2}(\text{Er}^{3+})$  state to the saturation of the  $^4I_{13/2}(\text{Er}^{3+})$  state through the so-called efficient energy back-transfer (EBT) process. [17] Through the exciting the nearest-neighboring  $\text{Yb}^{3+}$  ion at the ground state  $^2F_{7/2}(\text{Yb}^{3+})$  to the  $^2F_{5/2}(\text{Yb}^{3+})$  state, the excited  $\text{Er}^{3+}$  ion located at the  $^4S_{3/2}(\text{Er}^{3+})$  state, which originally emits green UC radiation, will transit

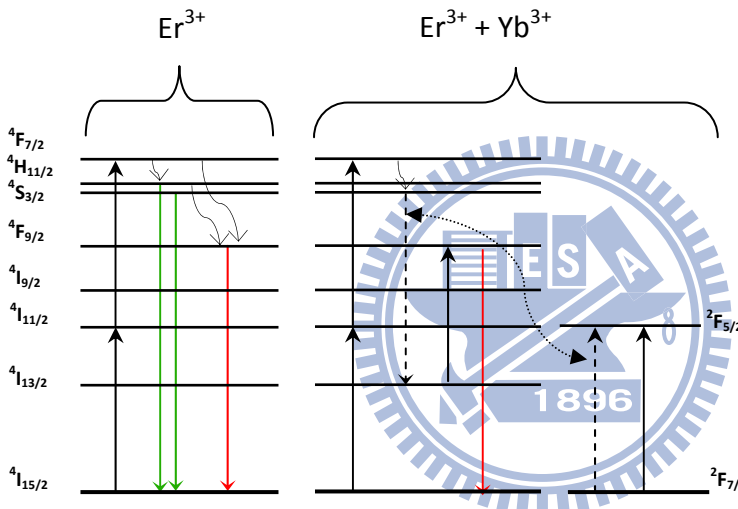


Figure 2.4: Energy level diagram of  $\text{Er}^{3+}$  and  $\text{Yb}^{3+}$  ions as well as the proposed mechanisms to produce UC spectra [17].

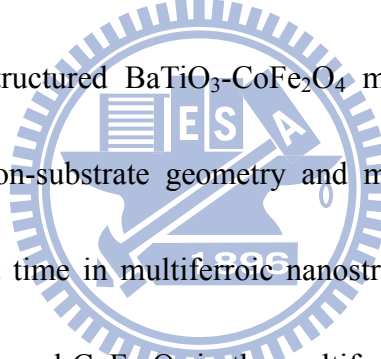
to the  $^4I_{13/2}(\text{Er}^{3+})$  state. This excitation was expressed as:  $^4S_{3/2}(\text{Er}^{3+}) + ^2F_{7/2}(\text{Yb}^{3+}) \rightarrow ^4I_{13/2}(\text{Er}^{3+}) + ^2F_{5/2}(\text{Yb}^{3+})$  and the energy diagram schematically presented in Figure 4 of Ref. 17 was duplicated in Figure 2.4 for making explanation clearer. Chen, *et al.* [17] reported that the energy mismatch in the EBT process is about  $320 \text{ cm}^{-1}$  and can be easily dissipated by one phonon of the  $\text{ZrO}_2$  lattice ( $470 \text{ cm}^{-1}$ ). The excited

$^2F_{5/2}$ -Yb $^{3+}$  ions can be further dissipated by another excitation that the Er $^{3+}$  ions transited from the ground state to the  $^4I_{11/2}$ (Er $^{3+}$ ) state then further relaxed to the long-lived  $^4I_{13/2}$ (Er $^{3+}$ ) state by the EBT process. The higher Yb $^{3+}$  ion concentration could provide the more Yb $^{3+}$  ions nearly neighboring to the Er $^{3+}$  ions to cause the efficient EBT process. The  $^4I_{13/2}$ -Er $^{3+}$  ion subsequently absorbs a laser photon from the  $^4I_{13/2}$ (Er $^{3+}$ ) state or directly relaxes from the high-lying states to populate  $^4F_{9/2}$ (Er $^{3+}$ ) state that the red UC emission arises. Thus, the efficient red UC radiation requires not only Yb $^{3+}$  concentration but also level match of  $^4S_{3/2} \rightarrow ^4I_{13/2}$  in Er $^{3+}$  and  $^2F_{7/2} \rightarrow ^2F_{5/2}$  in Yb $^{3+}$  under assistance of phonon for efficient EBT process. Therefore, the red UC emission would be a mixing process of one-photon process [12] through the efficient EBT process and two-photon process through relaxing from the high-lying states after GSA and ESA.

## 2.5 Multiferroic magnetoelectrics [18]

The magnetoelectric response is the appearance of an electric polarization upon applying a magnetic field and/or the appearance of magnetization upon applying an electric field. This magnetic-field- induced electric polarization has been observed as an intrinsic effect at low temperature and high magnetic field in some natural material systems (e.g., in RMnO<sub>3</sub> with R=Tb, Dy [19-21]). Alternatively and with

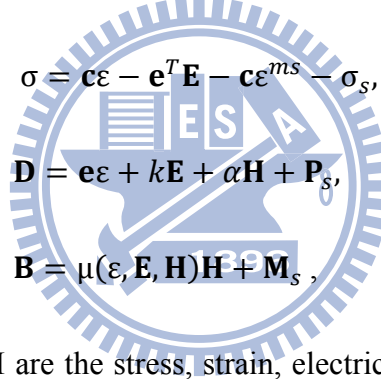
greater design flexibility, multiferroic composites made by a combination of ferromagnetic and ferroelectric substances, such as combinations of piezoelectric ceramics [e.g., BaTiO<sub>3</sub> and lead-zirconate-titanate (PZT)] and ferrites or rare-earth-iron alloys (e.g., Terfenol-D), have been recently found to exhibit large magnetoelectric response at room temperature and low magnetic field [22-27]. The magnetoelectric behavior in these multiferroic composites is dependent on their microstructure and coupling interaction across ferromagnetic-ferroelectric interface [28, 29].



Most recently, nanostructured BaTiO<sub>3</sub>-CoFe<sub>2</sub>O<sub>4</sub> multiferroic composites have been deposited in a film-on-substrate geometry and magnetoelectric coupling has been observed for the first time in multiferroic nanostructures [30]. The coupling interaction between BaTiO<sub>3</sub> and CoFe<sub>2</sub>O<sub>4</sub> in the multiferroic nanostructures has been found to be due to elastic interaction as was the case in bulk composites. However, the mechanical constraint arising from the film-on-substrate structures and the good bonding between the ferromagnetic and ferroelectric phases in the nanostructured films could significantly affect the coupling interactions, thereby the magnetoelectric effect and/or magnetic-field- induced electric polarization. Currently, a theoretical description on such multiferroic nanostructured films is lacking. The magnetoelectric effect is calculated in the nanostructured ferroelectric-ferromagnetic

composite films (e.g., BaTiO<sub>3</sub>-CoFe<sub>2</sub>O<sub>4</sub> films [30]) based on the Green's function is approach which had been successfully applied to bulk multiferroic composites [22, 23]. It provides the first phenomenological understanding of the magnetic-field-induced electric polarization in multiferroic nanostructures.

As the coupling interaction between ferroelectric and ferromagnetic phases in the multiferroic nanostructures is still an elastic interaction [30], the constitutive equations for the coupling magnetic-mechanical-electric interactions in the nanostructured films can be expressed by direct notation for tensors as

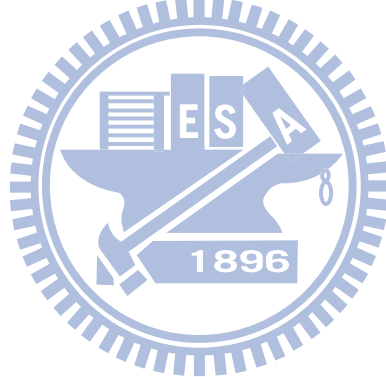


$$\begin{aligned}
 \sigma &= \mathbf{c}\boldsymbol{\varepsilon} - \mathbf{e}^T \mathbf{E} - \mathbf{c}\boldsymbol{\varepsilon}^{ms} - \sigma_s, \\
 \mathbf{D} &= \mathbf{e}\boldsymbol{\varepsilon} + k\mathbf{E} + \alpha\mathbf{H} + \mathbf{P}_\delta, \\
 \mathbf{B} &= \mu(\boldsymbol{\varepsilon}, \mathbf{E}, \mathbf{H})\mathbf{H} + \mathbf{M}_s,
 \end{aligned} \tag{2-35}$$

where  $\sigma$ ,  $\boldsymbol{\varepsilon}$ ,  $\mathbf{D}$ ,  $\mathbf{E}$ ,  $\mathbf{B}$ , and  $\mathbf{H}$  are the stress, strain, electric displacement, electric field, magnetic induction, and magnetic field, respectively;  $\mathbf{c}$  and  $k$  are, respectively, the stiffness at constant fields and the dielectric constant at constant strain; the permeability  $\mu$  strongly depends on  $\boldsymbol{\varepsilon}$  and electric and magnetic fields;  $\mathbf{e}$  ( $\mathbf{e}^T$  being the transpose of  $\mathbf{e}$ ) is the piezoelectric coefficient; and  $\boldsymbol{\varepsilon}^{ms}$  is the magnetostricively induced strain related with the magnetic field dependent magnetostriction constants (e.g.,  $\lambda_{001}$  and  $\lambda_{111}$  [31]) of the ferromagnetic phase;  $\sigma_s$  is the magnetoelectric coefficient. These are the same as the case for bulk multiferroic composites [22, 23].

However, in comparison to the bulk composites, there exist remarkable residual stress  $\sigma_s$  (or residual strain  $\varepsilon_s$ ), spontaneous polarization  $\mathbf{P}_s$  and magnetization  $\mathbf{M}_s$  in the multiferroic films.

The effective properties (denoted by the starred quantities below) of the multiferroic films can still be defined as usual [22, 23] in terms of the averaged fields (denoted by  $\langle \cdot \rangle$ ), e.g.,  $\langle \mathbf{D} \rangle = \mathbf{e}^* \langle \varepsilon \rangle + k^* \langle \mathbf{E} \rangle + \alpha^* \langle \mathbf{H} \rangle + \bar{\mathbf{P}}_s$ . We considered the magnetic-field- induced electric polarization of such nanostructured films. Under only applied magnetic field, the effective polarization in the mechanically clamped films is  $\bar{\mathbf{P}} = \alpha^* \langle \mathbf{H} \rangle + \bar{\mathbf{P}}_s$ .



## References

[1] A. K. Sood, N. Chandrabhas, D. V. S. Muthu, and A. Jayaraman, Phys. Rev. B 51, 8892 (1995).

[2] A. Chaves, R. S. Katiyar, and P. S. Porto, Phys. Rev. B 10, 3522 (1974).

[3] R. Resta, M. Posternak and A. Baldereschi, Phys. Rev. Lett. 70, 1010(1993).

[4] W. Zhong, R. D. King-Smith and D. Vanderbilt, Phys. Rev. Lett. 72, 3618 (1994).

[5] U. V. Waghmare and K. M. Rabe, Rev. B 55, 6161(1997).

[6] Gerhard Heinrich Dieke, H. M. Crosswhite, and Hannah Crosswhite Spectra and energy levels of rare earth ions in crystals ISBN: **0470213906** (1968).

[7] R. Scheps, Prog. Quant. Electr. 20, 271(1996).  
E. Heumann, S. Bär, K. Rademaker, G. Huber, S. Butterworth, A. Dienng, and W. Seelert, Appl. Phys. Lett. 88, 061108 (2006).

[8] E. Downing, L. Hesselink, and R. Macfarlane, Science 273 (5279) 1185 (1996).

[9] F. Xu, Z. Lv, Y. G. Zhang, G. Somesfalean, and Z. G. Zhang, Appl. Phys. Lett. 88, 231109 (2006).

[10] G. S. Yi, H. C. Lu, S. Y. Zhao, Y. Ge, W. J. Yang, D. P. Chen, and L. H. Guo Nano Lett. 4, 2191 (2004).

[11] G. Seisenberger, M. U. Ried, T. Endre, H. Büning, M. Hallek, and C. Bräuchle Science 294, 1929 (2001).

[12] J. H. Zeng, J. Su, Z. H. Li, R. X. Yan, and Y. D. Li, Adv. Mater. 17, 2119 (2005).

[13] G. Huber, E. Heumann, T. Sandrock, and K. Petermann, J. Lumin. 72-74, 1 (1997).

[14] U. Hömmerich, EiEi Nyein, and S. B. Trivedi, J. Lumin. 113, 100 (2005).

[15] G. Y. Chen, Y. G. Zhang, G. Somesfalean, Z. G. Zhang, Q. Sun, and F. P. Wang, Appl. Phys. Lett. 89, 163105 (2006).

[16] G. Y. Chen, Y. Liu, Y. G. Zhang, G. Somesfalean, Z. G. Zhang, Q. Sun and F. P. Wang, Appl. Phys. Lett. 91, 133103 (2007).

[17] G. Y. Chen, G. Somesfalean, Y. Liu, Z. Zhang, Q. Sun, and F. P. Wang, Phys. Rev. B 75, 195204 (2007).

[18] C. W. Nan, G. Liu, Y. Lin, and H. Chen, Phys. Rev. Lett. 94, 197203 (2005).

[19] T. Kimura et al., Nature (London) 426, 55 (2003);

[20] T. Goto et al., Phys. Rev. Lett. 92, 257201 (2004);

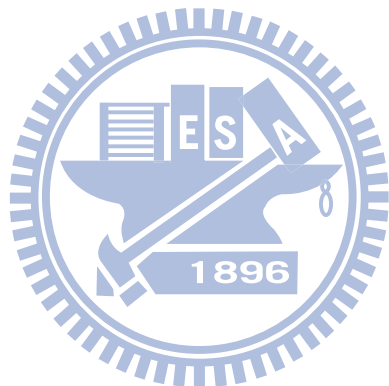
[21] N. Hur et al., Nature (London) 429, 392 (2004).

[22] C.W. Nan, M. Li, X. Q. Feng, and S. Yu, Appl. Phys. Lett. 78, 2527 (2001)

[23] C.W. Nan, M. Li, and J. H. Huang, Phys. Rev. B 63, 144415 (2001).

[24] J. Ruy et al., J. Am. Ceram. Soc. 84, 2905 (2001);

- [25] K. Mori and M. Wuttig, *Appl. Phys. Lett.* 81, 100 (2002);
- [26] S. X. Dong, J. F. Li, and D. Viehland, *Appl. Phys. Lett.* 83, 2265 (2003);
- [27] S. X. Dong, J. R. Cheng, J. F. Li, and D. Viehland, *Appl. Phys. Lett.* 83, 4812 (2003).
- [28] C.W. Nan, G. Liu, and Y. H. Lin, *Appl. Phys. Lett.* 83, 4366 (2003)
- [29] G. Liu, C.W. Nan, N. Cai, and Y. H. Lin, *J. Appl. Phys.* 95, 2660 (2004).
- [30] H. Zheng et al., *Science* 303, 661 (2004).
- [31] V. J. Folen, in *Magnetic and Other Properties of Oxides and Related Compounds*, edited by K. H. Hellwege and A. M. Hellwege, *Landolt-Bornstein Group III*, Vol. 4, Pt. b (Springer, Berlin, 1970), p. 366

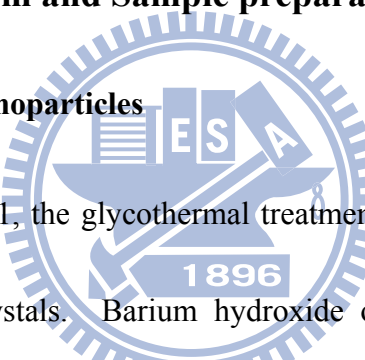


# Chapter 3 Experimental procedures and characterization techniques

The chemical solution methods were adopted to prepare various ferroics with different geometric types to yield homogeneous samples with highly accurate composition. We will describe in detail the procedure of chemical solution methods and characterization techniques as follows.

## 3.1 Synthesis mechanism and Sample preparation

### 3.1.1 Barium titanate nanoparticles

The logo is circular with a blue and white color scheme. It features a gear-like outer ring. Inside the ring, the letters 'TESLA' are arranged in a stylized font. Below the letters, the year '1896' is prominently displayed.

As shown in Figure 3.1, the glycothermal treatment method [1] was adopted to synthesize  $\text{BaTiO}_3$  nanocrystals. Barium hydroxide octahydrate ( $\text{Ba}(\text{OH})_2 \cdot 8\text{H}_2\text{O}$ ) was used as the source of Ba and titanium tetrachloride ( $\text{TiCl}_4$ ) was used as the source of Ti. Modification of titanium tetrachloride was achieved by adding deionized (DI) water to prepare transparent aqueous 0.1M  $\text{TiOCl}_2$  solution. Amorphous titanium hydrous gel was prepared by adding 30 ml  $\text{NH}_4\text{OH}$  (24%) drop into 160 ml 0.1M  $\text{TiOCl}_2$  solution at 60 °C for 2 h with stirring. The gel was separated and washed with DI water by 3 cycles of centrifugation for 4 min at 4000 rpm in a centrifuge. Excess water was decanted after final washing and the wet precursor was redispersed in a mixture of water and 1,4-butanediol.  $\text{Ba}(\text{OH})_2 \cdot 8\text{H}_2\text{O}$  then added into a mixture

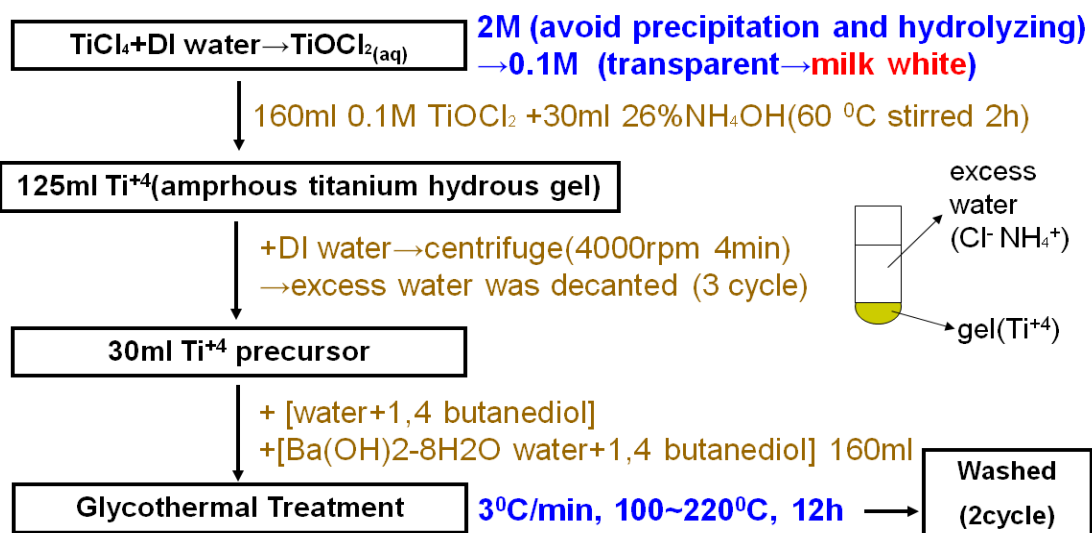


Figure 3.1: Flowchart of  $\text{BaTiO}_3$  nanocrystals preparation by glycothermal treatment method.

of water and 1,4-butanediol (1,4-butanediol/deionized water: B/W = 1, Ba:Ti molar ratio=1). Total volume of the solvent was 200 ml. The resultant suspension was placed in 250 ml flask equipped with a stirred head heated to the desired temperature with a rate of 3  $^\circ\text{C}/\text{min}$ . To acquire  $\text{BaTiO}_3$  particles with various grain sizes, reactions were carried out at the desired temperature from 100 to 220 $^\circ\text{C}$  for 12 h; the larger size of particles require the higher reaction temperature. After glycothermal treatment, the flask was cooled to RT. The powder was then washed with acetic acid solution to remove the residual  $\text{BaCO}_3$  and the unreacted Ba ions in solution. The removal of residual  $\text{BaCO}_3$  is crucial because its Raman spectra appear in the range of  $< 200 \text{ cm}^{-1}$  [2]. After washing, the recovered powder was dried at 60 $^\circ\text{C}$  in a hot plate for 48 h.

### 3.1.2 Barium titanate rods

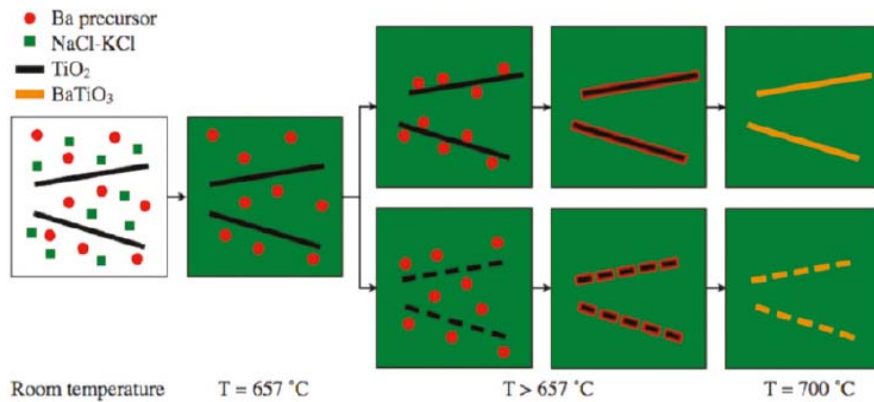


Figure 3.2: Proposed schematic diagram of the synthetic mechanism of  $\text{BaTiO}_3$  rods.

The three-series products (BT-1, BT-2 and BT-3) were synthesized with different barium and multi-shaped titanium precursors. Proposed schematic diagram of the synthetic mechanism of  $\text{BaTiO}_3$  rods is shown in Figure 3.2. BT-1 was synthesized by using  $\text{BaCO}_3$  as the barium precursors reacted with the spherical  $\text{TiO}_2$  in a eutectic mixture of NaCl-KCl flux. BT-2 and BT-3 were synthesized by using  $\text{BaO}$  and  $\text{BaCO}_3$  ( $\text{BaCO}_3$  will transform into  $\text{BaO}$  when heating over about  $1450\text{ }^\circ\text{C}$  which is much higher than the annealing temperature we used.) as the barium precursors reacted with the rod-shaped  $\text{TiO}_2$  in NaCl-KCl flux respectively. The reagents we used were  $\text{BaO}$ ,  $\text{BaCO}_3$ ,  $\text{TiO}_2$ ,  $\text{KCO}_3$ , NaCl and KCl, which were of A.R. grade without further purification. The rod-shaped  $\text{TiO}_2$  was synthesized and derived from rod-shaped  $\text{K}_2\text{Ti}_4\text{O}_9$ . The mixture of  $\text{K}_2\text{CO}_3$  and  $\text{TiO}_2$  in the molar ratio of 1:3 was annealed at  $1000\text{ }^\circ\text{C}$  for 18 h in the combustion boat ( $\text{Al}_2\text{O}_3$  boat). Then, the

as-synthesized product was washed with hot deionized water several times to remove the  $K_2CO_3$  phase entirely and finally dried at 60°C overnight. The product in the meanwhile was rod-shaped  $K_2Ti_4O_9$  verified by field emission scanning electron microscopy (FESEM) image and powder X-ray diffraction (XRD) pattern. The rod-shaped  $K_2Ti_4O_9$  then was washed with hot 1M HCl solution for 2 h to get rid of  $K_2O$  phase. The residue phase is  $TiO_2\bullet nH_2O$ , which was annealed at 700 °C for 1 h for transforming into the rod-shaped anatase.

To synthesize BT-1, BT-2, and BT-3, the detailed synthetic procedure is as follows. For starters, the mixture of barium precursor and titanium precursor in the molar ratio of 1:1 was wet-mixed in the ethanol solution at 50 °C for 1 h with magnetic stirring and then dried at 50 °C for 6 h. Second, the mixture was mixed with NaCl-KCl flux (50% mol NaCl and 50% mol KCl, m.p.: 657 °C), acting as a reaction medium, in the weight ratio of 1:1 by hand-grinding in a mortar and pestle for 0.5 h. Third, the as-synthesized mixture was placed into the combustion boat and heated at 700 °C for 1 h in the furnace. The increasing rate was 5 °C/min and the product was taken out of the furnace for cooling naturally after reaction. Finally, the as-synthesized product was washed with hot DI water several times until no chloride ions were detected by silver nitrate solution to assure the residue of salt was removed exhaustively and then dried at 120 °C overnight.

### 3.1.3 Rare-earth-doped perovskites

#### 3.1.3.1 Er<sup>3+</sup>-doped PLT poly-crystalline films

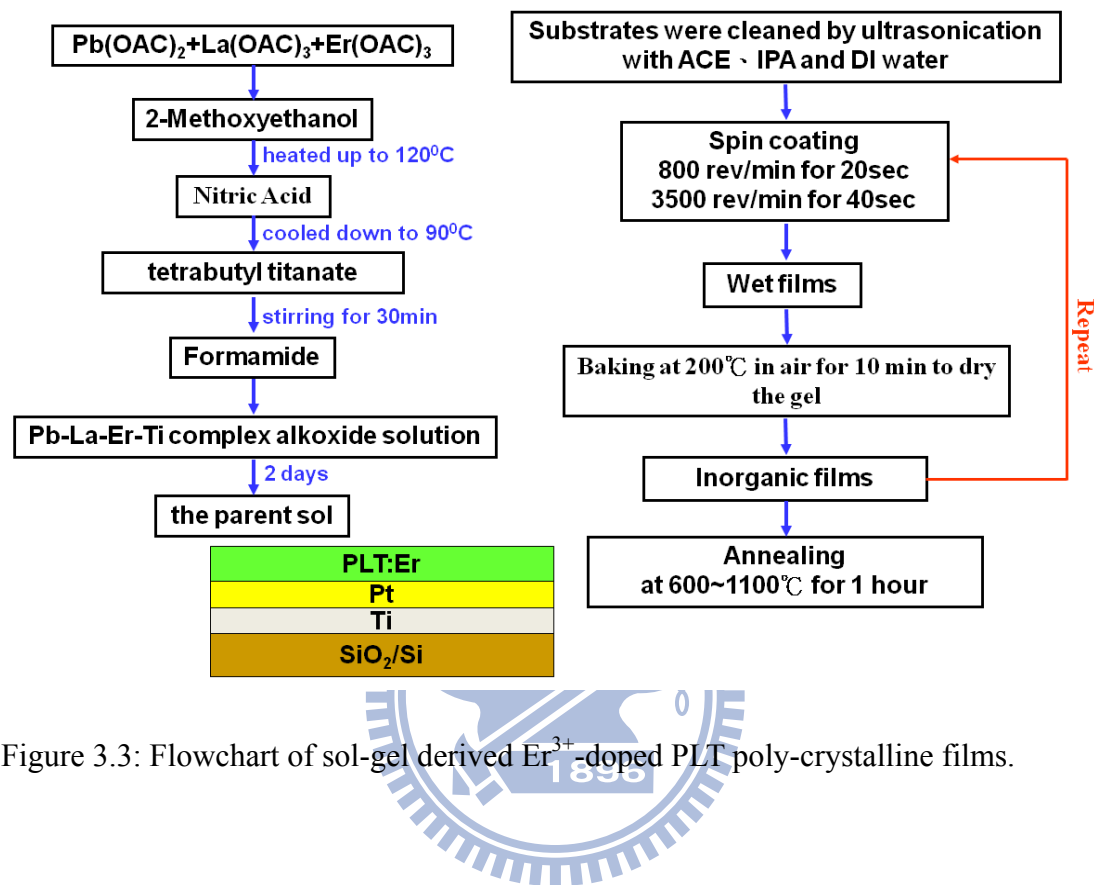
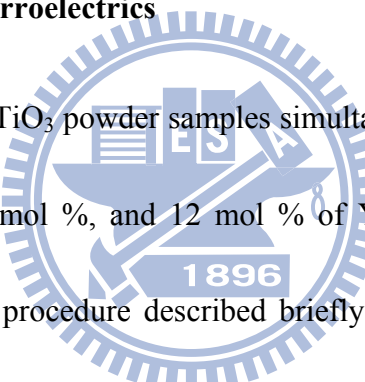


Figure 3.3: Flowchart of sol-gel derived Er<sup>3+</sup>-doped PLT poly-crystalline films.

As shown in Figure 3.3, Er<sup>3+</sup>-doped PLT poly-crystalline films were grown on the Pt/Ti/SiO<sub>2</sub>/Si substrates (supplied by ) by the sol-gel method. The starting materials are high-purity lead acetate, lanthanum acetate, titanium isopropoxide, and erbium acetate, respectively. Lead acetate and lanthanum acetate with molar ratios of 8:2 and proper mole of erbium acetate were dissolved in 2-Methoxyethanol and stirred for 10 minutes at 110°C to remove the associated water of crystallization. The stoichiometric amount of titanium isopropoxide was then added into the sol at 80°C while stirring continuously for approximately 10 minutes.

The diluted solution was then spin-coated on the clean Pt/Ti/SiO<sub>2</sub>/Si substrates, which were cleaned thoroughly in a series of organic solvents in an ultrasonic cleaner. The coated films were heated at 200°C in ambient atmosphere for 10 minutes to dry the gel. To accumulate the film thickness, we coated the samples by the aforementioned process ten times that corresponds to about 800 nm determined by the cross-section SEM. Finally, the samples were sintered in a furnace at various temperatures of 650~1100°C for 60 minutes.

### 3.1.3.2 Er-Yb codoped ferroelectrics



PbTiO<sub>3</sub>, BaTiO<sub>3</sub>, or SrTiO<sub>3</sub> powder samples simultaneously doped with 6 mol % Er<sup>3+</sup> ions and 0 mol %, 6 mol %, and 12 mol % of Yb<sup>3+</sup> ions, respectively, were synthesized according to a procedure described briefly as follows (see Figure 3.3). Lead acetate (or barium acetate, strontium acetate), erbium acetate, and ytterbium acetate with corresponding mole ratio of cations were first sufficiently stirred for 20 min at 90 °C for being completely dissolved in dehydrated acetic acid. Titanium isopropoxide was then added to the solution and kept stirring for another 20 min. We dried and solidified the solution under illumination of a 400 W infrared lamp for 36 h. The resultant solid was ground into powders and then sintered at 700 °C for 120 minutes in an Al<sub>2</sub>O<sub>3</sub> crucible.

### 3.1.4 Multiferroic films

We used simple solution method to fabricate three different geometric forms of the CFO-PTO multiferroics, which are respectively disk-like CFO aligned in PTO matrix (disk-3 type), the CFO and PTO multilayered structure (2-2 type), and the CFO particles embedded in PTO matrix (0-3 type) as shown in Figure 3.4.

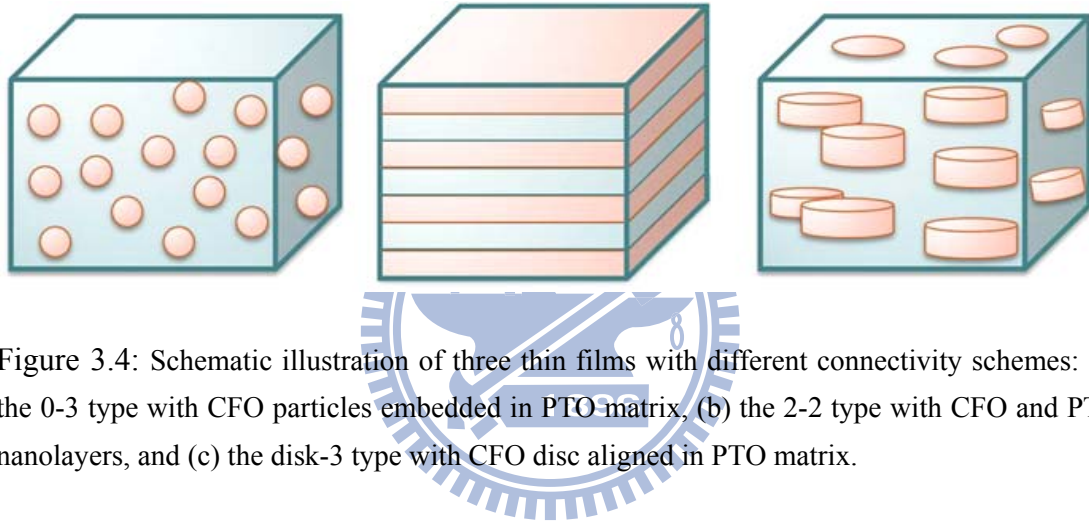
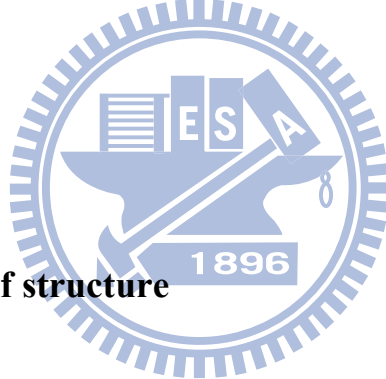


Figure 3.4: Schematic illustration of three thin films with different connectivity schemes: (a) the 0-3 type with CFO particles embedded in PTO matrix, (b) the 2-2 type with CFO and PTO nanolayers, and (c) the disk-3 type with CFO disc aligned in PTO matrix.

The gel of PTO was produced by dissolving lead acetate trihydrate and titanium isopropoxide into 2-methoxyethanol and stirring while heating for 30 min. The 0.3M CFO gel was made from the cobalt nitrate hexahydrate and iron nitrate enneahydrate by the same process. Pure PTO gel was spin-coated on Si and Pt/Si and CFO on Pt/Si substrate and then dried at 200°C for few times as the reference samples. The disk-3 type CFO-PTO samples were prepared by alternatively spin-coating PTO, drying then coating another CFO. Finally, we obtained

$(4p/4c/4p)^2/Pt/Si$  film, where “n”p and “n”c stands for successively coated and dried n times of PTO and CFO, respectively. The process of making the 2-2 type with  $(p/p/c/c)^3/p/p/Pt/Si$  stacking layers is the same as the disk-3 type except that every single layer was individually annealed at 500 °C for 3 minutes. The 0-3 type is made of dispersing CFO particles in PTO matrix. The CFO particles of ~100 nm, obtained by drying CFO gel and annealed at 750°C, were then put into the  $PbTiO_3$  solution with molar ratio 0.8:1 and shaken until they were well-mixed. The resultant solution was spin-coated 5 layers on Pt/Si substrate. Finally, all the samples were annealed at 750 °C for 1.5 h.



### 3.2 Characterization of structure

#### 3.2.1 X-ray Diffraction

The XRD data of the prepared  $BaTiO_3$  nanoparticles were collected on the imaging plate with transmission geometry using high intensity synchrotron radiation with wavelength of 0.56357 Å at beam line BL01C synchrotron radiation facility, NSRRC in Taiwan (see Figure 3.5). A single tetragonal-phase ( $P4mm$ ) model was applied to refine the crystal structure with the XRD data by using the Rietveld analysis computer program GSAS (General Structure Analysis System) provided by National Institute of Standards and Technology (NIST) in USA. Furthermore, the

XRD data of the others were measured, using a Mac science M18X X-ray diffractometer equipped with a rotating anode (Cu- $\text{k}\alpha$  line of 1.5405 Å). Data were recorded between the angle range  $20^\circ < 2\theta < 60^\circ$  with steps of  $0.04^\circ$  and rate of scanning is  $4^\circ/\text{min}$ . The resulting XRD patterns were Gaussian fitted to get the diffraction peaks and widths. By comparing with the JCPDS data, the fitted peak positions and corresponding reflection planes were used as the input of the refinement program [3]. In the next step, the lattice constants will be included in output files.



Figure 3.5: BL01C Experimental Station.

### 3.2.2 Field-Emission Scanning Electron Microscopy (FESEM)

The morphology of synthesized particles was observed using field-emission scanning electron microscopy (FESEM, JEOL 6500).

### 3.2.3 Raman spectroscopy

Raman spectroscopy consists of mainly three components: laser system, spectrometer, and computer. Figure 3.6 shows schematics of experimental setup. An-ion laser (Coherent INNOVA 90) provides an excitation source of a wavelength 488nm. The unwanted plasma lines were filtered out by a laser-line filter. A biconvex spherical lens with a focal length of 5cm was used to focus the laser beam onto the sample surface at 45 degree reflection geometry. The laser power on the sample surface is about 30~50 mW with beam spot size of 30~50  $\mu m$  (in diameter). The scattered light was collected by a camera lens and imaged onto the entrance slit of a spectrograph (Spex triplemate1877C) which is equipped with a liquid-nitrogen cooled charge coupled device (CCD) detector array (Phometrics CC200) at 140K.

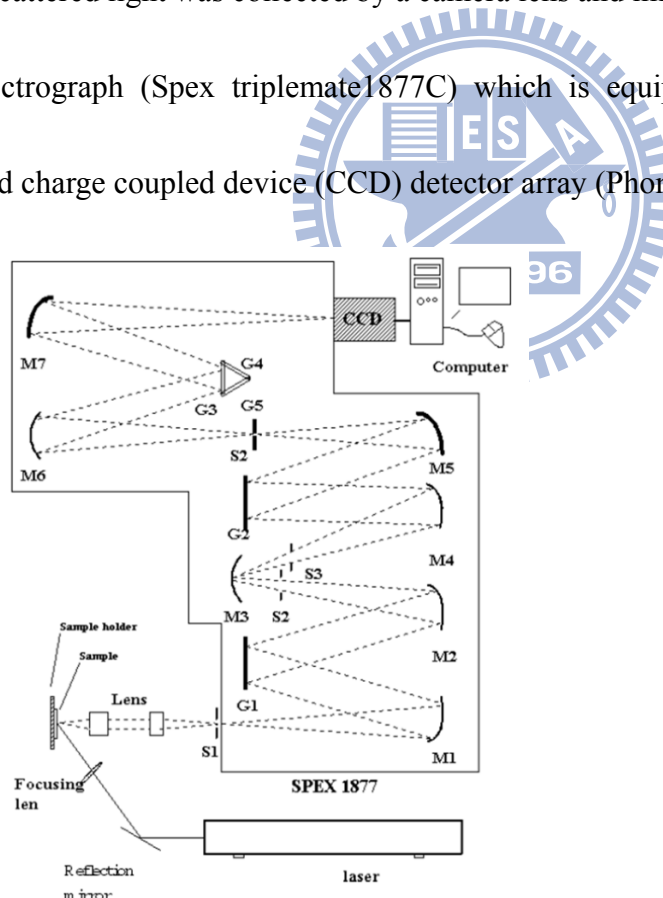


Figure 3.6: Setup of typical Raman and PL measurements.

### **3.3 Characterization of optical properties--Photoluminescence spectroscopy**

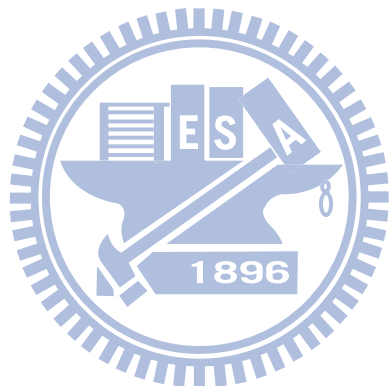
Photoluminescence (PL) of Er-doped  $\text{Pb}_{0.8}\text{La}_{0.2}\text{TiO}_3$  thin films were carried out by pumping with the 488 nm line of  $\text{Ar}^+$  laser and the emitted UC fluorescence spectra of Er-Yb codoped ferroelectrics were performed by pumping with a 980 nm diode laser with maximal power output of 600 mW. The experimental setup is the same as that described in Raman measurement.

### **3.4 Characterization of magnetic properties--Superconducting Quantum Interference Device magnetometry**

The magnetic properties were measured by Superconducting Quantum Interference Device (SQUID, MPMS-XL) system. The SQUID is very sensitive to magnetic field. By utilizing SQUID technology, the SQUID magnetometer can achieve superior measurement sensitivity. The standard deviation of measurement can achieve about  $10^{-8}$  emu with Reciprocating Sample Option (RSO) and about  $10^{-7}$  emu with traditional stepped-scan technique under 0.1 Tesla.

## References

- [1] Y. J. Junga, D. Y. Lima, J. S. Nhoc, S. B. Chob, R. E. Rimanc, and B. W. Leed, *J. Crystal Growth* 274, 638 (2005).
- [2] C. Pithan, Y. Shiratori, and R. Waser, *J. Am. Ceram. Soc.* 89, 2908 (2006).
- [3] B. Rupp, A computer program for Rietveld analysis of x-ray and neutron powder diffraction patterns, <http://www.tuppweb.org/weblat/weblat.htm> , (2005).



## Chapter 4 Destruction to the short-range disorder due to erbium dopant in $\text{Pb}_{0.8}\text{La}_{0.2}\text{TiO}_3$ films

Perovskites, the chemical formula of  $\text{ABO}_3$ , are generally composed of a three-dimensional framework of corner sharing  $\text{BO}_6$  octahedron and it is believed that there always exists disorder displacement of “B” ions in the skeleton. The characteristics of perovskites can be changed by replacing the “A” and “B” cations. In this chapter, we study on influence of perovskite structure due to the presence of substitution on luminescence and characteristics of  $\text{Er}^{3+}$ -doped  $\text{Pb}_{0.8}\text{La}_{0.2}\text{TiO}_3$  (PLT) polycrystalline films. We show destruction to a displacement of Ti in the short-range structure by observing the disappearance of emission and Raman signals when the  $\text{Er}^{3+}$  concentration exceeds 7 mol% in sol-gel-derived PLT polycrystalline films. The disorder due to a displacement of Ti breaks the centrosymmetry to activate emission of rare earth ions such as  $\text{Er}^{3+}$  and Raman modes of perovskites. We found the symmetry breaking diminishes with introducing more  $\text{Er}^{3+}$  ions.

### 4.1 Crystal structure (results of XRD)

Figure 4.1(a) shows the XRD patterns of 7 mol%  $\text{Er}^{3+}$ -doped PLT films on Pt/Ti/SiO<sub>2</sub>/Si at various sintering temperatures 650–1100°C and the pattern of un-doped

PLT film at 800°C is also presented for comparison. The Er<sup>3+</sup>-doped PLT film sintered at 650°C shows a perovskite phase with (100), (110), (200), (210) and (211) planes without obvious secondary phases. As the films were sintered at 800 °C and 950 °C, the diffraction peaks of the perovskite phase become more intense and their full widths at half maximum (FWHM) become narrower. It indicates that the films have better crystallinity at the higher sintering temperatures even though the weak secondary phases appear. We found small signatures of the secondary Er<sub>2</sub>Ti<sub>2</sub>O<sub>7</sub> phase appearing at  $2\theta = 31^\circ$  and Er<sub>2</sub>O<sub>3</sub> phase at 36° and 43.7° for sintering at 950°C. By further raising the sintering temperature to 1100°C, the strong peaks at 27° due to La<sub>2</sub>Si<sub>2</sub>O<sub>7</sub> consistent with the JCPDS data (# 722456) were recognized. It is believed that La<sub>2</sub>Si<sub>2</sub>O<sub>7</sub> phase appeared at the interface between Er<sup>3+</sup>-doped PLT thin films and silicon substrate during high-temperature sintering. And the peaks of the perovskite phase become weaker or even vanish, indicating the destruction of perovskite structure. The FWHM of (100) analyzed from the result of XRD pattern in Figure 4.1(a) tends to decrease from 0.28° to 0.22°, corresponding to the crystal size ranging from 28.9 to 36.8 nm, while increasing the sintering temperature from 650 to 950°C. The better crystallinity for the higher sintering temperature is universally known.

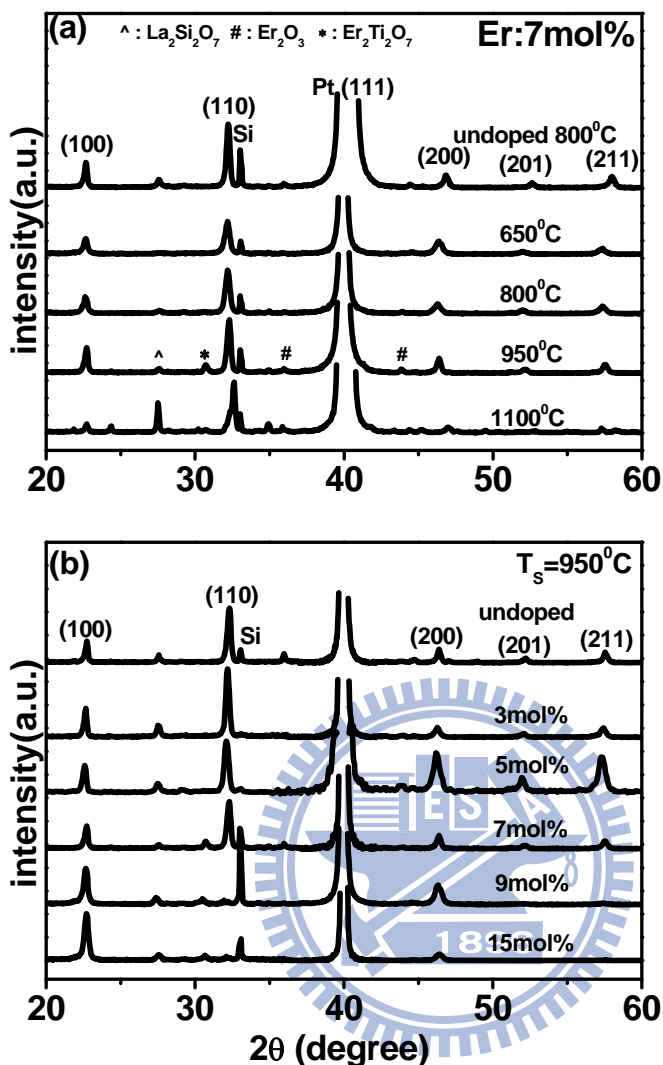


Figure 4.1: XRD patterns of Er<sup>3+</sup>-doped PLT films with 7 mol% Er<sup>3+</sup> doping at various sintering temperatures and with different Er<sup>3+</sup> concentrations at sintering temperature 950°C.

Figure 4.1(b) shows the XRD patterns of PLT films on Pt/Ti /SiO<sub>2</sub>/Si doped with different Er<sup>3+</sup> concentrations after being sintered at 950°C. All films exhibit good perovskite crystallinity, although several weak secondary phases appear. Due to the same charge state, Er<sup>3+</sup> may take the positions of La<sup>3+</sup> in the lattice. It indicates that

the  $\text{Er}^{3+}$  is dissolved in PLT by more than 15 mol% without destroying the crystallinity in the PLT system that exceeds the result of BST system<sup>8</sup> of 3 mol%. Although the slight difference in the peak intensity of (110) and (211) for 9 mol% and 15 mol%  $\text{Er}^{3+}$ -doped samples may not be ascribed to alignments, the results still confirm a perovskite phase in these  $\text{Er}^{3+}$ -doped PLT powders.

In order to investigate the variation of long-range structures with the increase of  $\text{Er}^{3+}$  concentration, the resultant XRD patterns in Figure 4.1(b) were further analyzed with the refinement procedure. We have adopted the tetragonal structure for all samples to obtain the ratio of lattice constants  $c/a$ . The initial data of (100), (110), (200), (201) and (211) planes identified with the JCPDS data are input to the XLAT program.<sup>[1]</sup> Plotted in Figure 4.2 are the FWHM of (100) and  $c/a$  versus the  $\text{Er}^{3+}$  concentration. The FWHM tends to linearly increase from  $0.22^\circ$  to  $0.31^\circ$ , corresponding to the crystal diameter ranging from 36.8 to 26.1 nm, as increasing the  $\text{Er}^{3+}$ -dopant from 0 to 15 mol%. It reveals degradation of the crystallinity for the higher  $\text{Er}^{3+}$ -dopant. On the other hand, the ratio of  $c/a$ , is between 1.001 and 1.007, which is much smaller than that of  $\text{PbTiO}_3$  (1.067) but comparable or slightly larger than that <sup>[2]</sup> of  $\text{BaTiO}_3$  (1.002). It indicates that the  $\text{Er}^{3+}$ -doped PLT films with different  $\text{Er}^{3+}$  concentrations of 0, 3, 5, 7, 9, and 15 mol% all belong to the tetragonal phase. We found that  $c/a$  is around 1.002 for the undoped sample, and slightly

increases and then declines to around 1.001 at 7 mol%, then increases to 1.007 for the samples with 9 and 15 mol%. The trend of  $c/a$  ratio with  $\text{Er}^{3+}$  concentration is similar to the results reported by Dobal *et al.* [3]. They reported that the tetragonality ratio  $c/a$  increases with increasing with dopant concentration when  $\text{Pb}_{0.90}\text{La}_{0.15}\text{TiO}_3$  was doped with  $\text{Gd}^{3+}$ . As the  $\text{Er}^{3+}$ -ion concentration increases or the host material possesses the higher tetragonality,

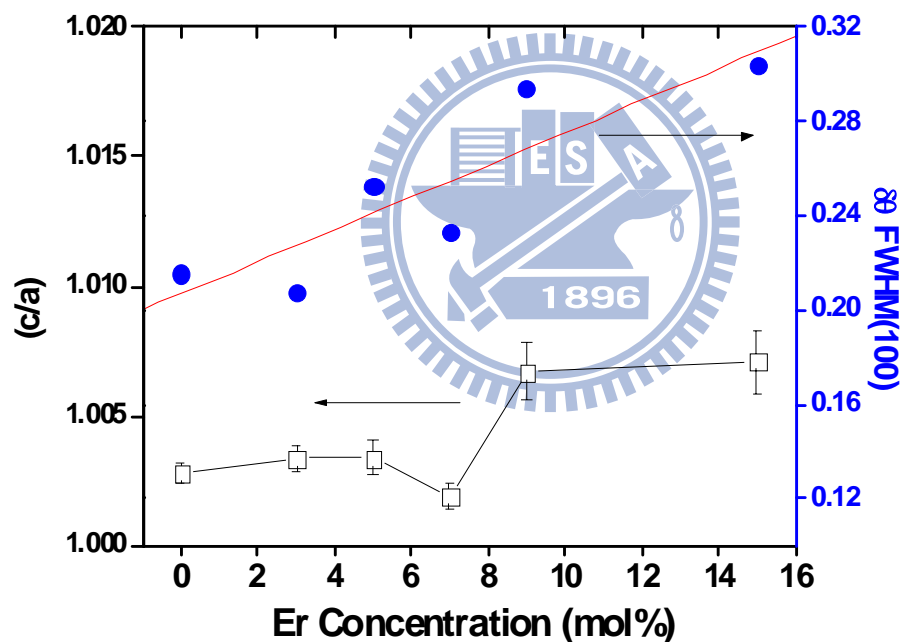


Figure 4.2: The ratio of lattice constants  $c/a$  after Rietveld refinement and the FWHM of (100) with different  $\text{Er}^{3+}$  concentrations at sintering temperature 950°C.

we expected that the stronger emission was observed. However, we will show shortly that the maximum emission was observed at 7 mol% but no emission for  $\text{Er}^{3+}$

dopant larger than 9 mol%, which possess the higher tetragonality (non-centrosymmetry) than for the 7 mol% one.

## 4.2 Relationship between results of emission spectra and Raman spectra

Figure 4.3(a) shows the RT visible emission spectra of PLT films doped with 7 mol%  $\text{Er}^{3+}$  ions at sintering temperatures of 650, 800, 950 and 1100°C, respectively.

All the visible emission spectra have similar shapes, but they possess the diversity of emission behavior. The strong green emission peaks at 530 and 550 nm are attributed to the  $\text{Er}^{3+}$   $4f-4f$  inner-shell transitions of  $^2\text{H}_{11/2} \rightarrow ^4\text{I}_{15/2}$  and  $^4\text{S}_{3/2} \rightarrow ^4\text{I}_{15/2}$ , while the weak red emission centered at 660 nm is ascribed to  $^4\text{F}_{9/2} \rightarrow ^4\text{I}_{15/2}$ . The splits in emission peaks are attributed to the Stark splitting of the degenerate 4f levels under the crystalline field of the host material. As expected, the better crystalline (see Figure 4.1(a)), the higher emission as increasing the sintering temperature from 650 to 950°C, and weak emission was observed at 1100°C sintering.

The high  $\text{Er}^{3+}$  concentration also might mean the high emission efficiency, and Figure 4.3(b) displays the spectra of PLT films doped with different  $\text{Er}^{3+}$  concentrations of 3, 5, 7, and 9 mol% after sintered at 950°C. However, the emission intensity of the  $\text{Er}^{3+}$ -doped PLT films does increase as the activated  $\text{Er}^{3+}$ -dopant

increases until 7 mol%, but quickly decreases as the  $\text{Er}^{3+}$ -doping concentration exceeds 7 mol%. The quenching mechanism was thought to be a cross-relaxation process between two closely-placed  $\text{Er}^{3+}$  ions. [4-6]

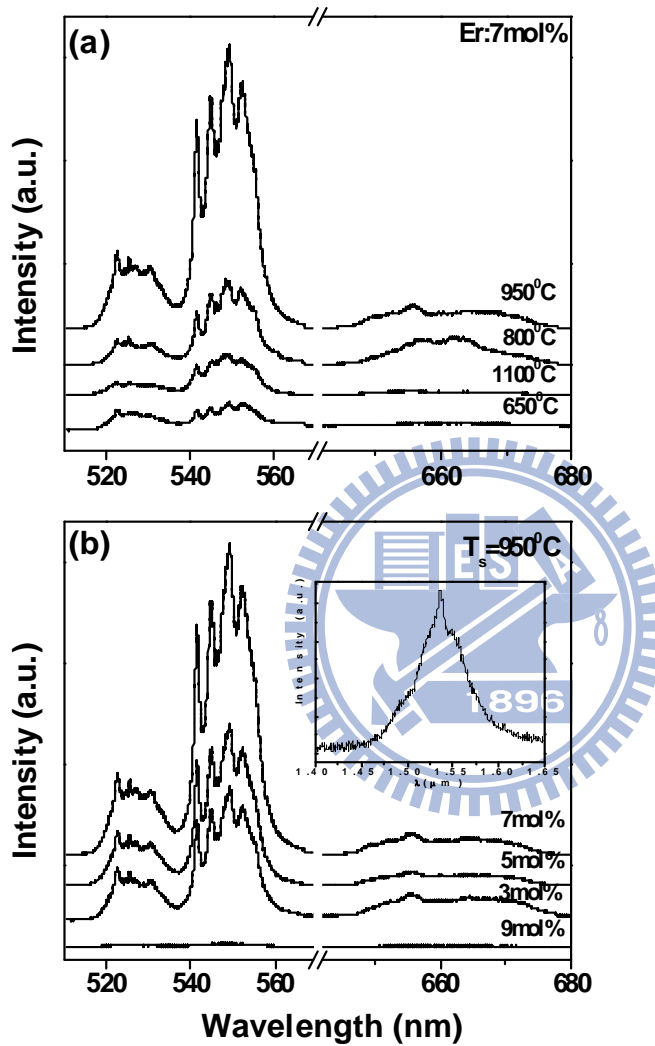


Figure 4.3: Dependence of the green emission intensities of  $\text{Er}^{3+}$ -doped PLT films on  $\text{Er}^{3+}$  concentrations and sintering temperature.

In this study, the ion density  $N$  of 3, 5, 7, and 9 mol %  $\text{Er}^{3+}$  doping is about  $4.9 \times 10^{20}$ ,  $8.2 \times 10^{20}$ ,  $11.4 \times 10^{20}$ , and  $14.7 \times 10^{20}/\text{cm}^3$ , respectively, and the mean

distance [7] among  $\text{Er}^{3+}$  ions estimated by  $\gamma=0.62\times N^{1/3}$  is 7.8, 6.6, 5.9, and 5.5 Å, correspondingly. The mean distance varies gently with increasing  $\text{Er}^{3+}$  concentration from 7 mol% to 9 mol%, while the emission efficiency decreases sharply. This indicates that the quenching mechanism would not be dominated by a cross-relaxation process, and therefore there may be other dominant factors responsible for decreasing emission efficiency in  $\text{Er}^{3+}$ -doped PLT system. Looking back on the result of Figure 4.2, because the 9 mol%  $\text{Er}^{3+}$ -dopant films do possess higher tetragonality (non-centrosymmetry) than the 7 mol% ones, the quenching mechanism also would not be dominated by the long-range structure and crystalline. As proposed by Tanabe *et al.*, that the emission efficiency has to do with the degree of local structure symmetry, [8] the quenching behavior is related to the local structure symmetry, which will be discussed with the results of Raman measurement later on. In addition, we also observed the RT IR-emission spectra of PLT films doped with 5 mol%  $\text{Er}^{3+}$  concentrations at 950°C sintering in the inset of Figure 4.3(b) under the excitation of 488-nm Ar-ion laser.

Figure 4.4(a) shows the Raman spectra of samples with different  $\text{Er}^{3+}$  concentrations in PLT sintered at 950°C. Besides the weak broad feature between 700 and 800  $\text{cm}^{-1}$  we found another broad spectrum centered around 560  $\text{cm}^{-1}$  that is attributed to  $\text{A}_1(\text{TO}_3)+\text{E}(\text{TO}_3)$  phonon modes due to the reduced grain size and the

localized disorder of displacement of Ti ion from the center of

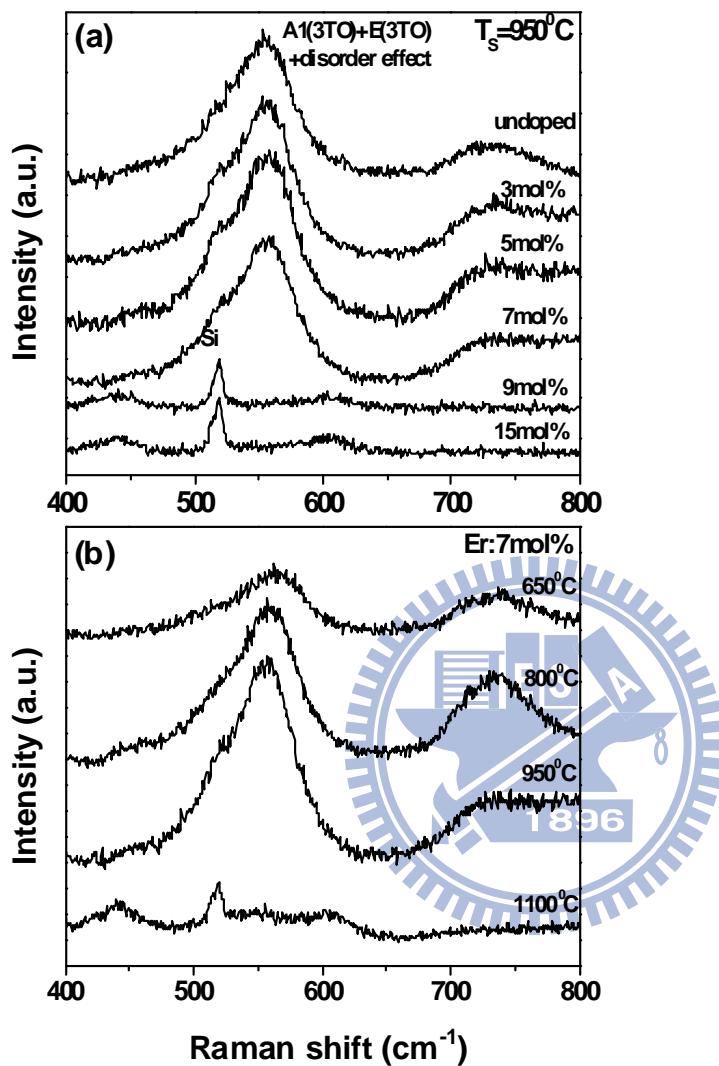


Figure 4.4: Raman spectra of  $\text{Er}^{3+}$ -doped PLT films with different  $\text{Er}^{3+}$  concentrations at sintering temperature  $950^\circ\text{C}$  and with 7 mol%  $\text{Er}^{3+}$  dopant at various sintering temperatures.

the  $\text{BO}_6$  octahedron. [4-6] These peaks keep almost unchanged as  $\text{Er}^{3+}$  concentration increases from 3 mol% to 7 mol%, but vanish for samples with 9 and 15 mol%  $\text{Er}^{3+}$

concentrations with only Si-LO phonon at  $520\text{ cm}^{-1}$  from the Si substrate and phonon modes of amorphous native oxide around  $440$  and  $600\text{ cm}^{-1}$ . The disappearance of Raman modes due to either weak ferroelectric phase or weak disorder effect (resulting from a displacement of Ti) is caused by decreasing the crystal diameter to result in the formation of a centrosymmetric structure [9] with increasing  $\text{Er}^{3+}$  concentration. By comparing with the results of XRD, we found weakening in disorder may be the dominant mechanism. In Figure 4.5, schematic representation of the mechanism illustrating that Ti atom displaces off its central position and moves towards one oxygen as  $\text{Er}^{3+}$  concentration is below or at 7 mol%. Nevertheless, it will return to its central position when the  $\text{Er}^{3+}$  concentration reaches or exceeds 9 mol%. Figure 4.4(b) shows change of the Raman spectra of  $\text{Er}^{3+}$ -doped PLT films at 7 mol %  $\text{Er}^{3+}$  ions, with increasing the annealing temperature from  $650$  to  $1100^\circ\text{C}$ . We found similar disappearance of these specific phonons resulting from destruction to a perovskite structure at sintering temperatures beyond  $1100^\circ\text{C}$ .

It is interesting to correlate the Raman spectra of Figure 4.4 with green emission emission of Figure 4.3. We found no variation in the ferroelectric and disorder modes from the Raman spectra, while the emission intensity of the  $\text{Er}^{3+}$ -doped PLT films increases as the  $\text{Er}^{3+}$ -dopant increases from 3 to 7 mol%. In contrast, by increasing the  $\text{Er}^{3+}$  concentration to 9 mol%, we found the green emission and the

disorder effect on Raman scattering suddenly diminish, indicating the selection rule is strongly reinforced to eliminate the short-range disorder, and the crystal structure becomes strictly centro-symmetric.

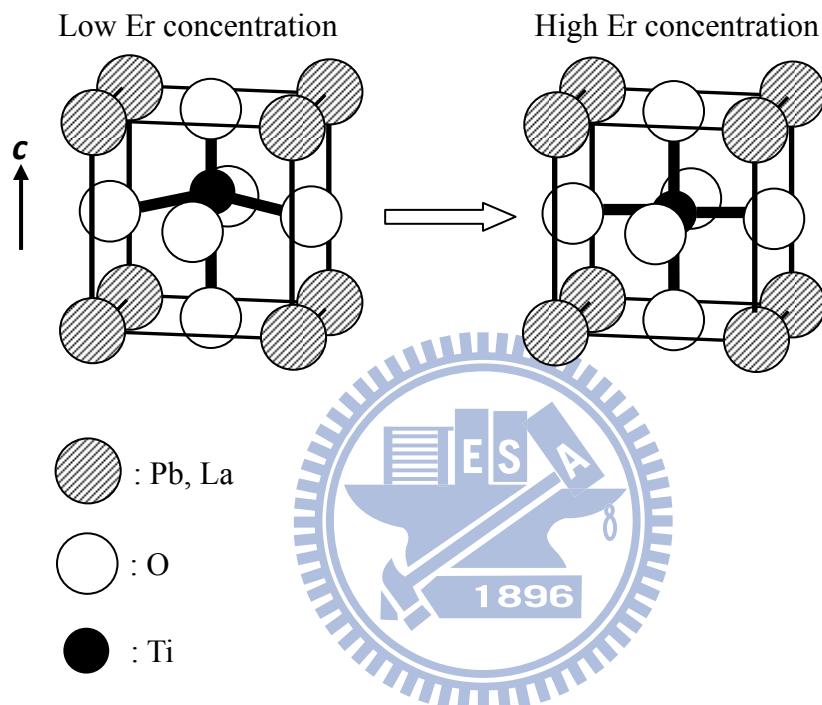
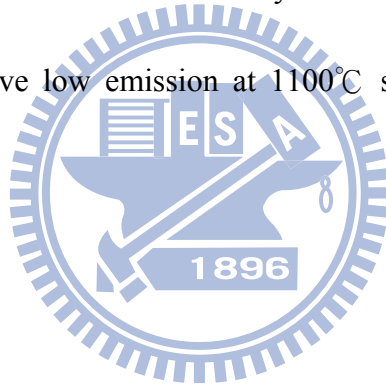


Figure 4.5: Schematic representation of the position of B atom in  $\text{ABO}_3$  structure.

Looking back in Figure 4.3(b) and Figure 4.4(a), we found that the green emission becomes weaker and the disorder effect vanishes separately, but the crystal structure remains unchanged while increasing the  $\text{Er}^{3+}$  concentration above 9 mol%. It reveals the destruction to short-range disorder reduces the efficiency of emission, even though these films still possess good crystallinity. Thus, the symmetry on short

range of  $\text{Er}^{3+}$ -doped PLT crystal seems to influence the activity of  $\text{Er}^{3+}$  ions. The more symmetric structure of the host materials would reduce the transition probability within the 4f-inner shell of  $\text{Er}^{3+}$  ion.

In contrast with the analysis of emission and Raman spectra, the films possess a good perovskite phase at sintering temperatures of  $600^\circ\text{C}$ ,  $800^\circ\text{C}$ , and  $950^\circ\text{C}$ , so that they have similar visible emission spectral shapes and phonon modes. The weak perovskite phase at a sintering temperature of  $650^\circ\text{C}$  results in weak emission as strong emission originates from the best crystalline at  $950^\circ\text{C}$ -sintering. The unobvious split with relative low emission at  $1100^\circ\text{C}$  sintering is due to structure destruction.



### 4.3 Summary

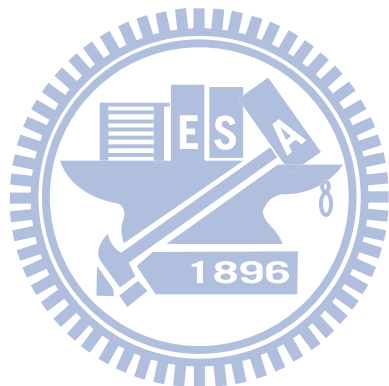
The  $\text{Er}^{3+}$ -doped  $\text{Pb}_{0.8}\text{La}_{0.2}\text{TiO}_3$  films with perovskite structure were manufactured on  $\text{Pt}/\text{Ti}/\text{SiO}_2/\text{Si}$  substrates by sol-gel method. The dependence of emission efficiency on  $\text{Er}^{3+}$  concentration and sintering temperature is dominated by solubility and symmetry of crystal structure. We showed that destruction to the short-range disorder displacement of B ions exists in the skeleton of  $\text{BO}_6$  from the disappearance of emission and Raman signals when the  $\text{Er}^{3+}$  concentration exceeded 7 mol%, although the samples still possess good long-range structure, confirmed by X-ray

diffraction. The crystal field due to the disorder effect that contributes to the perturbation term for the  $\text{Er}^{3+} 4f - 4f$  inner-shell transitions is diminished when introducing more  $\text{Er}^{3+}$  concentration.



## References

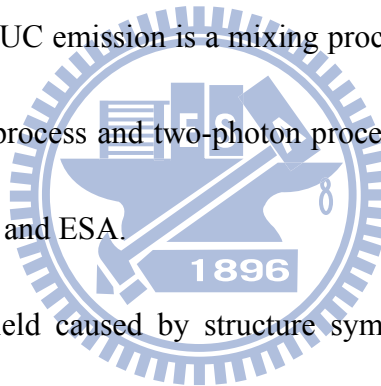
- [1] B. Rupp, A computer program for Rietveld analysis of x-ray and neutron powder diffraction patterns, <http://www.tuppweb.org/weblat/weblat.htm> , (2005).
- [2] S. Y. Kuo, W. Y. Liao and W. F. Hsieh, *Phys. Rev. B* **64** 224103 (2001).
- [3] P. S. Dobal, R. R. Das, B. Roy, R. S. Katiyar, S. Jain and D. C. Agrawal, *J. Raman Spectrosc.* **31**, 965–970 (2000).
- [4] M. Fujii, M. Yoshida, S. Hayashi, K. Yamamoto, *J. Appl. Phys.* **84**, 4525 (1998).
- [5] T. M. Kozhan, *Spectrochim. Acta Part A* **55**, 1407 (1999).
- [6] X. Chen, T. Nguyen, Q. Luu, and B. DiBartolo, *J. Lumin.* **85**, 295 (2000).
- [7] C. Y. Chen, R. P. Petrin, D. C. Yeh, W. A. Sibley, and J. L. Adam, *Opt. Lett.* **14**, 432 (1989).
- [8] S. Tanabe, T. Ohyagi, N. Soga, T. Hanada, *Phys. Rev. B* **46**, 3305 (1992).
- [9] V. Petkov, M. Gateshki, M. Niederberger, and Y. Ren, *Chem. Matter* **18**, 814 (2006).



## Chapter 5 Er-Yb codoped ferroelectrics for controlling visible upconversion emissions

UC emission in RE ion-doped materials has been intensively studied in recent years of applications in laser devices [1, 2], three-dimensional display [3], sensors [4], and biological fluorescent labels [5-7]. Following the influence of perovskite structure on luminescence with a **one-photon** process in  $\text{Er}^{3+}$ -doped PLT discussed in chapter 4, the mechanism of UC emission in RE ions co-doped materials has been discussed in this chapter. UC emission is a mixing process of one-photon process [8]

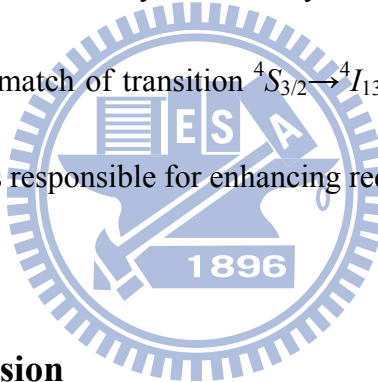
through the efficient EBT process and two-photon process through relaxing from the high-lying states after GSA and ESA.



The different crystal field caused by structure symmetry of the host materials would contribute to different perturbation terms for the  $\text{Er}^{3+}$  and  $\text{Yb}^{3+}$  inner shell transitions. Whether the energy matches level spacing  $^4S_{3/2} \rightarrow ^4I_{13/2}$  of the  $\text{Er}^{3+}$  ion and  $^2F_{7/2} \rightarrow ^2F_{5/2}$  of the  $\text{Yb}^{3+}$  ion or not should be sensitive not only to assistance of phonon but also to the crystal field resulting from the crystal symmetry. Therefore, the crystal structure may be a more important mechanism for converting UC green radiation to red radiation due to the EBT process. In order to investigate the relationship between the crystal field and the match of energy levels, in this chapter,

we chose  $\text{PbTiO}_3$ ,  $\text{BaTiO}_3$  and  $\text{SrTiO}_3$  with different degrees of tetragonality as the host materials. Both  $\text{PbTiO}_3$  and  $\text{BaTiO}_3$  are ferroelectric perovskites which possess tetragonal phase at room temperature, while  $\text{SrTiO}_3$  is a quantum paraelectric [9]. The tetragonality of  $\text{PbTiO}_3$  ( $c/a=1.065$ ) is higher than that of  $\text{BaTiO}_3$  ( $c/a=1.010$ ) according to the JCPDS-International Center for Diffraction Data No. 78-0298 and No. 83.1880.

In this chapter, UC emission spectra under a 980 nm laser pumping and X-ray diffraction confirm that the centrosymmetric crystal field arising from reducing tetragonality causes level match of transition  $^4S_{3/2}\rightarrow^4I_{13/2}$  of  $\text{Er}^{3+}$  and  $^2F_{7/2}\rightarrow^2F_{5/2}$  of  $\text{Yb}^{3+}$ . This level match is responsible for enhancing red UC emission.



## 5.1 Upconversion emission

Figure 5.1 shows the UC fluorescence spectra of  $\text{PbTiO}_3$  [Figure 5.1(a)],  $\text{BaTiO}_3$  [Figure 5.1(b)] and  $\text{SrTiO}_3$  [Figure 5.1(c)] doped with 6 mol%  $\text{Er}^{3+}$  ions and various concentrations of  $\text{Yb}^{3+}$  ions under 980 nm excitation. As mentioned above and in the literature [8, 10], the emission bands around 550/565 nm (green) and 655/680 nm (red) originate from the intra  $4f$ - $4f$  electronic transitions  $^2\text{H}_{11/2}/^4\text{S}_{3/2}\rightarrow^4\text{I}_{15/2}$  and  $^4\text{F}_{9/2}\rightarrow^4\text{I}_{15/2}$  of the  $\text{Er}^{3+}$  ions, respectively. The green and red bands in this study are

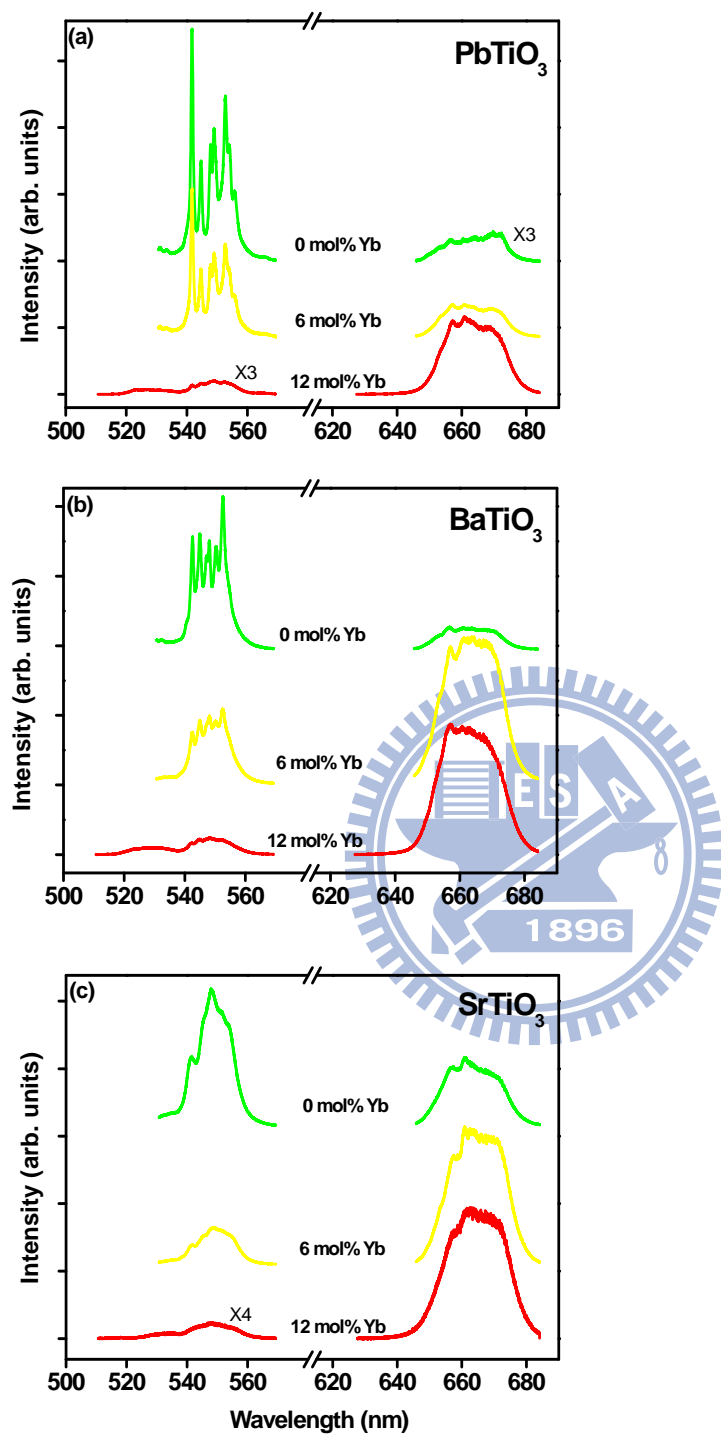


Figure 5.1: UC fluorescence spectra of (a)  $\text{PbTiO}_3$ , (b)  $\text{BaTiO}_3$ , and (c)  $\text{SrTiO}_3$  doped with 6 mol%  $\text{Er}^{3+}$  ions and various concentrations of  $\text{Yb}^{3+}$  ions under the same pump power of 980 nm diode laser at 107 mW.

slightly shifted comparing to what appears in Ref. 8, we found the radiation peak positions and the spectral shapes of the red (around 665 nm) and the green fluorescent radiations (545/565 nm) are different from those in Ref. 8. It indicates that the different structure symmetry of host materials result in the different influence of crystal field on the energy levels of  $\text{Er}^{3+}$  and  $\text{Yb}^{3+}$ . The very weak red UC emission is a two-photon process at only  $\text{Er}^{3+}$  doping in various systems, which indicates a few population of  $^4F_{9/2}(\text{Er})$  state. The bandwidths of the two UC labels are found about 30 nm. In these spectra, besides the quenching of green UC emission with increasing  $\text{Yb}^{3+}$  concentration, which indicates decreasing the population of the  $^2H_{11/2}$  /  $^4S_{3/2}(\text{Er}^{3+})$  state, we observed level splits in green UC emission of only  $\text{Er}^{3+}$  doping and co-doped 6 mol%  $\text{Yb}^{3+}$  ones in  $\text{PbTiO}_3$  and  $\text{BaTiO}_3$ . It is attributed to the Stark splitting of the degenerate 4f levels under the strong crystal field of the  $\text{PbTiO}_3$  and  $\text{BaTiO}_3$  [11]. The split in  $\text{PbTiO}_3$  system is more obvious than that in  $\text{BaTiO}_3$  system indicating the stronger influence of crystal field on the energy levels of  $\text{Er}^{3+}$  and  $\text{Yb}^{3+}$  in  $\text{PbTiO}_3$  than in  $\text{BaTiO}_3$  due to the larger asymmetric crystal field for the host material of larger tetragonality. On the other hand, the spectral shapes become smoother because of the weaker influence of the more centrosymmetric crystal field for high concentration  $\text{Yb}^{3+}$  (12 mol%) in both  $\text{PbTiO}_3$  and  $\text{BaTiO}_3$  systems and all samples in  $\text{SrTiO}_3$  system. Figure 5.1 also shows unobvious splits in all of the red

UC emission spectra. It reveals that the underlying mechanism of the red UC emission differs from that of green one. The intensity of red UC emission greatly increases as the  $\text{Yb}^{3+}$ -ion concentration increases, that results from the increasing of the EBT process as reported by Chen, *et al.* [8]. The very weak red UC emission is a two-photon process at only  $\text{Er}^{3+}$  doping in various systems, which indicates a few population of  $^4F_{9/2}(\text{Er})$  state; whereas, the strong red UC emission and almost complete quenching of the UC green emission are observed at co-doped 12 mol%  $\text{Yb}^{3+}$ . The energy mismatch in the EBT process is about  $320 \text{ cm}^{-1}$  that can be easily dissipated by the aid of one phonon of the  $\text{ZrO}_2$  lattice with energy  $470 \text{ cm}^{-1}$  in [8]. If the energy mismatch in the EBT process were dissipated by one phonon of the  $\text{PbTiO}_3$  lattice with energy  $290 \text{ cm}^{-1}$  or  $510 \text{ cm}^{-1}$  and the  $\text{BaTiO}_3$  lattice with  $310 \text{ cm}^{-1}$  or  $520 \text{ cm}^{-1}$ , then the intensity ratios of the green UC and the red UC should make no difference for the same amount of  $\text{Yb}^{3+}$  in  $\text{PbTiO}_3$  and  $\text{BaTiO}_3$ . However, we observed that the red UC emission is stronger than the green one at co-doped 6 mol%  $\text{Yb}^{3+}$  in  $\text{BaTiO}_3$  system, but weaker red UC emission in the  $\text{PbTiO}_3$  system of the same doping. This reveals a weak EBT process in  $\text{PbTiO}_3$  with 6 mol%  $\text{Yb}^{3+}$  co-doping. The observed spectral peak positions and shapes of green and red bands are slightly different from what observed in [8] that may be attributed to different crystal field. We observed a broad red emission around 665 nm with FWHM of 22

nm which is almost unchanged with crystal structure, but the position of maximal peak is at 544 nm ( $18382\text{ cm}^{-1}$ ) at only  $\text{Er}^{3+}$  doping in  $\text{PbTiO}_3$  while it changes to 555 nm ( $18018\text{ cm}^{-1}$ ) at the same doping in  $\text{BaTiO}_3$ . It indicates that the different structure symmetry of host materials resulted in the different influence of crystal field on the energy levels of  $\text{Er}^{3+}$  over a spectral range of  $363\text{ cm}^{-1}$ . Therefore, the energy mismatch in the EBT process may be dissipated not only by the aid of phonons but also by Boltzmann distributed population within the manifold of  $^4\text{S}_{3/2}$  or/and  $^4\text{I}_{13/2}$  ( $\text{Er}^{3+}$ ) state affected by the crystal field with different symmetries. The strength of EBT process depends on whether the energy match of level space  $^4\text{S}_{3/2}\rightarrow^4\text{I}_{13/2}$  of the  $\text{Er}^{3+}$  ion and  $^2\text{F}_{7/2}\rightarrow^2\text{F}_{5/2}$  of the  $\text{Yb}^{3+}$  ion that strongly depends on crystal field due to structure symmetry [10]. The match can be achieved for centrosymmetric media but may not be so due to the asymmetric crystal field in tetragonal phase, thus to lower the strength of EBT process. We will discuss the influence of change of the crystal structure on the EBT process in the following using X-ray diffraction.

## 5.2 Mechanisms of upconversion emission

### 5.2.1 Crystal structure (results of XRD)

Figure 5.2 displays the x-ray diffraction patterns of various concentrations of  $\text{Er}^{3+}$ - and  $\text{Yb}^{3+}$ - doped  $\text{PbTiO}_3$  [Figure 5.2(a)] and  $\text{BaTiO}_3$  [Figure 5.2(b)] with

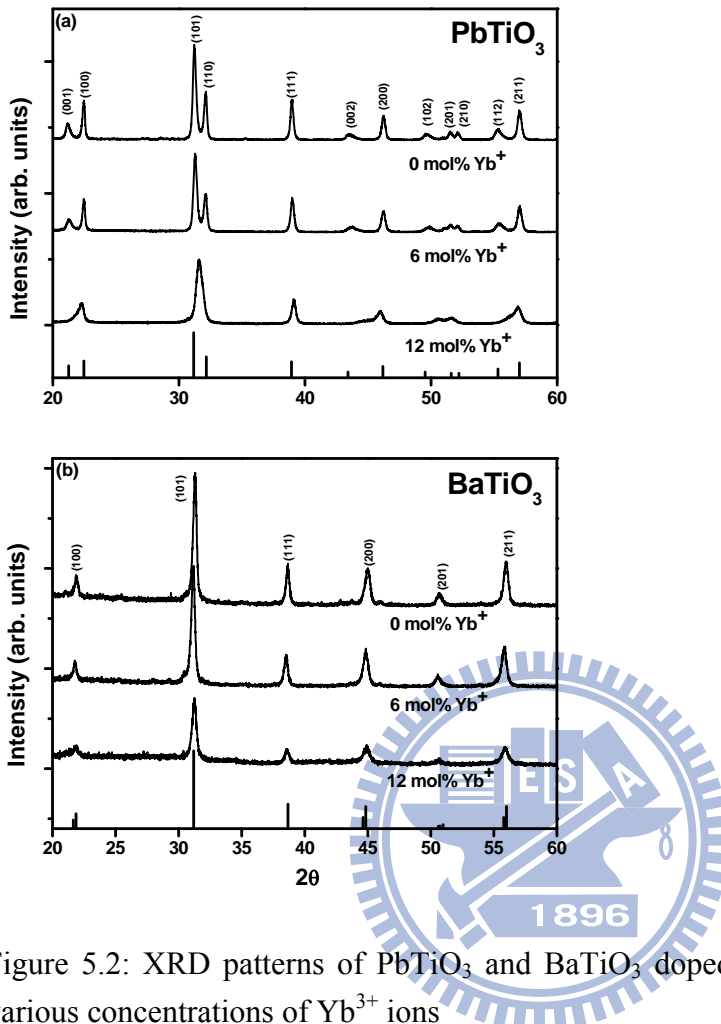


Figure 5.2: XRD patterns of  $\text{PbTiO}_3$  and  $\text{BaTiO}_3$  doped with 6 mol%  $\text{Er}^{3+}$  ions and various concentrations of  $\text{Yb}^{3+}$  ions

sintering temperature at  $700^\circ\text{C}$ . All the samples already show a tetragonal phase with various planes without obvious secondary phases, corresponding well to the standard powder diffraction pattern. To further investigate the variation of structures with the increase of  $\text{Yb}^{3+}$  concentration, a tetragonal single phase ( $P4mm$ ) model was applied to refine the crystal structure with the XRD data. Here we just showed the refinement result of  $\text{PbTiO}_3$  doped with 6 mol%  $\text{Er}^{3+}$  ions and 6 mol%  $\text{Yb}^{3+}$  ions in

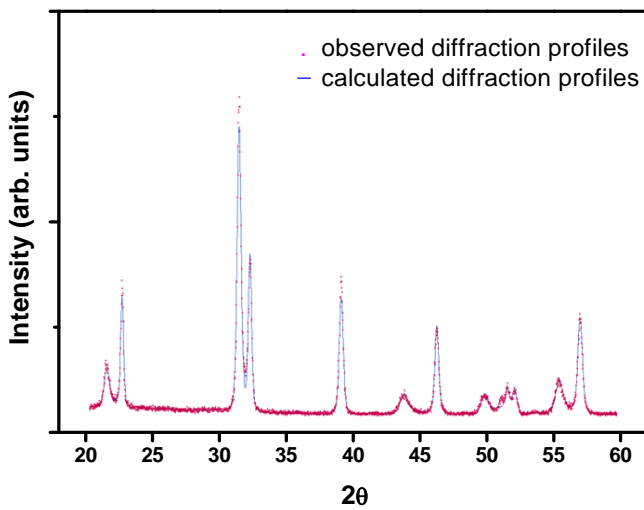


Figure 5.3: Rietveld pattern of  $\text{PbTiO}_3$  doped with only 6 mol%  $\text{Er}^{3+}$  ions and 6 mol%  $\text{Yb}^{3+}$  ions.

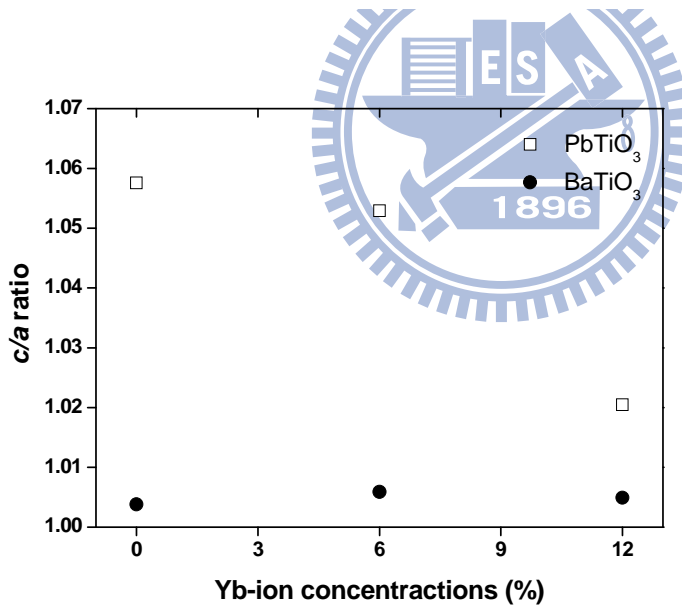


Figure 5.4:  $c/a$  ( $a$  and  $c$  are lattice constants) ratio as function of  $\text{Yb}^{3+}$ - ion concentrations after Rietveld refinement.

Figure 5.3 and the calculated profiles agree well with the observed ones. Figure 5.4 plots the  $\text{Yb}^{3+}$  concentrations dependence of the tetragonality,  $c/a$ , and lattice

constants following Rietveld refinement. As  $\text{Yb}^{3+}$ -ion concentration changes from 0, 6, to 12 mol %, the tetragonality ( $c/a$ ) of  $\text{PbTiO}_3$  system declines from 1.058, 1.053, to 1.020; moreover,  $c/a$  of  $\text{BaTiO}_3$  system retains around 1.005. A Decline of tetragonality is due to the presence of substitution of  $\text{Er}^{3+}$  and  $\text{Yb}^{3+}$  ions in  $\text{PbTiO}_3$  that is similar to the results reported by Kuo *et al.* [12].

### 5.2.2 Symmetry-dependent upconversion mechanism

The declining tetragonality of  $\text{PbTiO}_3$  system as increasing  $\text{Yb}^{3+}$  concentration will result in weakening the crystal field on  $\text{Er}^{3+}$  and  $\text{Yb}^{3+}$  ions, in turn, it benefits the match of the level space  $^4S_{3/2} \rightarrow ^4I_{13/2}$  of the  $\text{Er}^{3+}$  ion and  $^2F_{7/2} \rightarrow ^2F_{5/2}$  of the  $\text{Yb}^{3+}$  ion to enhance the EBT process. These results are consistent with the observed split of spectral peaks of green UC emission in tetragonal phase as well as the quenching of green UC emission and enhancement of red UC emission for high  $\text{Yb}^{3+}$  concentration with low tetragonality.

As compared with  $\text{PbTiO}_3$  system and  $\text{BaTiO}_3$  system at 6 mol% at  $\text{Yb}^{3+}$  concentration, the larger asymmetric crystal field for  $\text{PbTiO}_3$  of larger tetragonality on  $\text{Er}^{3+}$  and  $\text{Yb}^{3+}$  ions results in the mismatch of resonant photons. The weak strength of EBT process due to the larger asymmetric crystal field at 6 mol% at  $\text{Yb}^{3+}$  concentration in  $\text{PbTiO}_3$  leads to weak red UC emission. It agrees with the result of the dependence of red UC emission on structure of host material at the same  $\text{Yb}^{3+}$

concentration.

### 5.2.3 Pump power dependent upconversion

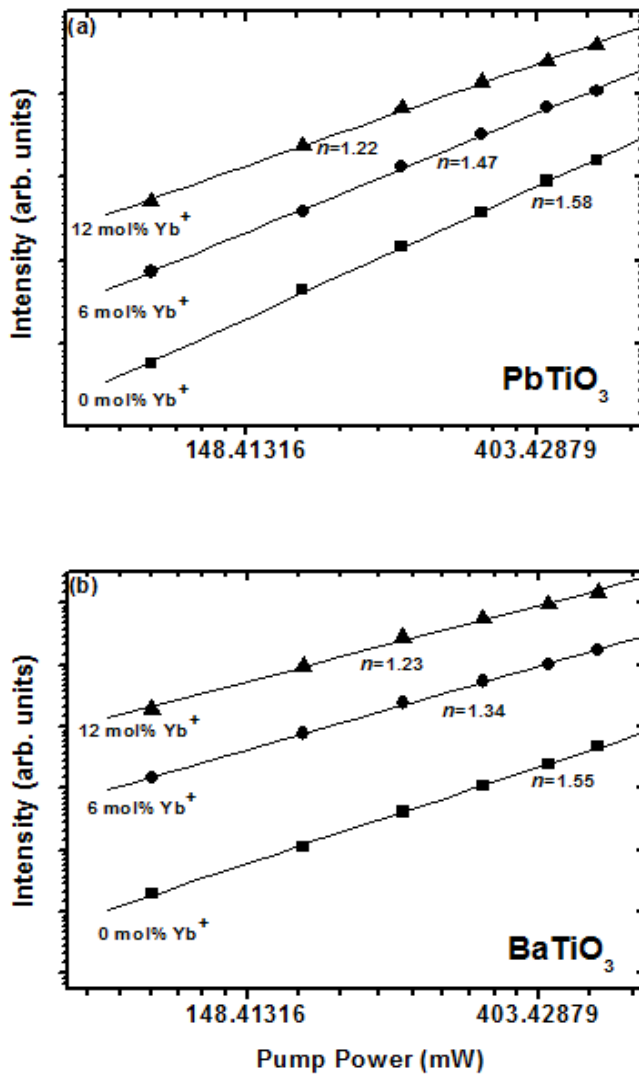


Figure 5.5: Pump power dependence of the red upconversion emission of  $\text{PbTiO}_3$  and  $\text{BaTiO}_3$  doped with 6 mol%  $\text{Er}^{3+}$  ions and various concentrations of  $\text{Yb}^{3+}$  ions in a logarithmic scale.

To verify the mechanism of red UC emission, we investigated the dependence of intensity ( $I$ ) of red UC emission on the pump power ( $P$ ). It is possible to determine

the number of photons ( $n$ ) required for populating the emitting state according to [13, 14]:

$$I \propto P^n. \quad (5-1)$$

Similar to Ref. [8], the  $n$  value is close to 2 for the green UC emission. Because we are more interested in the mechanism of red UC emission, we plotted the logarithm diagram of  $I$  versus  $P$  for both  $\text{PbTiO}_3$  and  $\text{BaTiO}_3$  systems in Figure 5.5.

As shown in Figure 5.5(a), the  $n$  value decreases from 1.58 for 0 mol %  $\text{Yb}^{3+}$ -ion to 1.47 for 6 mol %  $\text{Yb}^{3+}$ -ion concentration doped  $\text{PbTiO}_3$ , which indicate a mixing

process of one- and two-photon for producing the red band with two-photon process being still the dominant mechanism. The EBT process is relatively weak because the strong crystal field due to the structure asymmetry contributes to the level mismatch between  $^4S_{3/2} \rightarrow ^4I_{13/2}$  of  $\text{Er}^{3+}$  ion and  $^2F_{7/2} \rightarrow ^2F_{5/2}$  of  $\text{Yb}^{3+}$  ion. However,

for 12 mol%  $\text{Yb}^{3+}$  doping, the power law shows one-photon process dominant with  $n = 1.22$ , namely, the efficient EBT process takes over to effectively quench the  $^4S_{3/2}(\text{Er})$  state and so to diminish the green band (see Figure 5.1(a)) in the more centrosymmetric host matrices at the highest  $\text{Yb}^{3+}$ -ion concentration (Figure 5.2(a)).

On the contrary, the  $n$  value is also 1.55 in Figure 5.5(b) for 0 mol%  $\text{Yb}^{3+}$  doped  $\text{BaTiO}_3$ , which is a two-photon process. It becomes 1.34 and 1.23 for  $\text{Yb}^{3+}$ -ion concentrations of 6 and 12 mol%, respectively. Under this circumstance, the  $^4S_{3/2}(\text{Er})$

states, which the green UC radiation arises, were strongly quenched with low green emission in Figure 5.1(b) via the EBT process to saturate the  $^4I_{13/2}(\text{Er})$  state through coupling with the transition  $^2F_{7/2} \rightarrow ^2F_{5/2}$  of  $\text{Yb}^{3+}$  ion. And the strong red UC emission were observed dominated by the one-photon process in doped nearly cubic-phase  $\text{BaTiO}_3$  (see Figure 5.2(b)). The efficient red UC radiation requires not only  $\text{Yb}^{3+}$  concentration but also level match of  $^4S_{3/2} \rightarrow ^4I_{13/2}$  in  $\text{Er}^{3+}$  and  $^2F_{7/2} \rightarrow ^2F_{5/2}$  in  $\text{Yb}^{3+}$  under assistance of Boltzmann distributed population within the manifold of  $^4S_{3/2}$  or/and  $^4I_{13/2}(\text{Er}^{3+})$  state affected by the crystal field with different symmetries for efficient EBT process. Declining tetragonality results in the centrosymmetric crystal field for high  $\text{Yb}^{3+}$ -ion to achieve the above-mentioned level matches, which may be difficult to be fulfilled with asymmetric crystal field in ferroelectric phase. It agrees with the results of XRD and of the dependence of red UC emission on structure of host materials at the same  $\text{Yb}^{3+}$  concentration.

### 5.3 Summary

As increasing  $\text{Yb}^{3+}$  co-doped concentrations in 6 mol%  $\text{Er}^{3+}$  doped  $\text{PbTiO}_3$ ,  $\text{BaTiO}_3$ , and  $\text{SrTiO}_3$  polycrystalline powder samples, we have observed the room-temperature green UC emission at 550 nm being quenched by the simultaneously enhanced red UC emission at 660 nm under the 980-nm laser

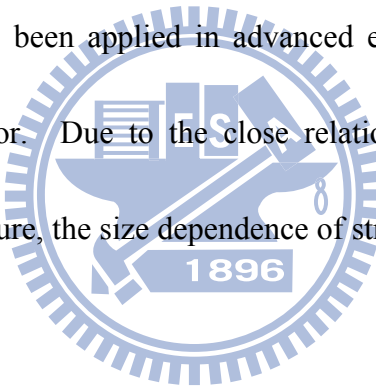
excitation. For codoping  $\text{Yb}^{3+}$  ions up to 6 mol% in  $\text{PbTiO}_3$  and only  $\text{Er}^{3+}$  doped  $\text{PbTiO}_3$  samples, which still possess relatively large tetragonality, the green UC emission is still much stronger than red one. In these cases, both the UC emissions are dominated by the two-photon process. But, as further increasing the  $\text{Yb}^{3+}$  ion concentration, the crystal structures tend to become cubic phase with enhancing red UC emission and almost diminishing in green emission. Since the pure  $\text{BaTiO}_3$  crystal exhibits weaker tetragonality than  $\text{PbTiO}_3$ , the stronger red emission and weaker green one were expected at the lower codoped  $\text{Yb}^{3+}$  concentration in  $\text{BaTiO}_3$  system than in  $\text{PbTiO}_3$  one. The observed quench of green radiation accompanied with enhancement of red radiation should be due to the efficient energy back-transfer process as reported by Chen, *et al.* by raising  $\text{Yb}^{3+}$  concentration [8]. The efficient EBT process requires not only  $\text{Yb}^{3+}$  concentration but also level match of  $^4\text{S}_{3/2} \rightarrow ^4\text{I}_{13/2}$  in  $\text{Er}^{3+}$  and  $^2\text{F}_{7/2} \rightarrow ^2\text{F}_{5/2}$  in  $\text{Yb}^{3+}$  under assistance of Boltzmann distributed population within the manifold of  $^4\text{S}_{3/2}$  or/and  $^4\text{I}_{13/2}$  ( $\text{Er}^{3+}$ ) state affected by the crystal field with different symmetries. As a result, declining tetragonality results in the centrosymmetric crystal field for high  $\text{Yb}^{3+}$ -ion concentration to achieve the level match required for the EBT process that may be difficult to be fulfilled with asymmetric crystal field in the tetragonal (ferroelectric) phase.

## References

- [1] R. Scheps, *Prog. Quant. Electr.* **20**, 271 (1996).
- [2] E. Heumann, S. Bär, K. Rademaker, G. Huber, S. Butterworth, A. Dienng, and W. Seelert, *Appl. Phys. Lett.* **88**, 061108 (2006).
- [3] E. Downing, L. Hesselink, and R. Macfarlane, *Science* **273** (5279) 1185 (1996).
- [4] F. Xu, Z. Lv, Y. G. Zhang, G. Somesfalean, and Z. G. Zhang, *Appl. Phys. Lett.* **88**, 231109 (2006).
- [5] G. S. Yi, H. C. Lu, S. Y. Zhao, Y. Ge, W. J. Yang, D. P. Chen, and L. H. Guo, *Nano Lett.* **4**, 2191 (2004).
- [6] G. Seisenberger, M. U. Ried, T. Endre, H. Büning, M. Hallek, and C. Bräuchle, *Science* **294**, 1929 (2001).
- [7] J. H. Zeng, J. Su, Z. H. Li, R. X. Yan, and Y. D. Li, *Adv. Mater.* **17**, 2119 (2005).
- [8] G. Y. Chen, G. Somesfalean, Y. Liu, Z. Zhang, Q. Sun, and F. P. Wang, *Phys. Rev. B* **75**, 195204 (2007).
- [9] K. A. Muller and H. Burkard, *Phys. Rev. B* **19**, 3593 (1979).
- [10] N. C. Chang, J. B. Gruber, R. P. Leavitt, and C. A. Morrison, *J. Chem. Phys.* **76**, 3877 (1982).
- [11] J. B. Gruber, D. K. Sardar, C. C. Russell, R. M. Yow, B. Zandi, and E. P. Kokanyan, *J. Appl. Phys.* **94**, 7128 (2003).; J. B. Gruber, R. M. Yow, A. S. Nijjar, C. C. Russell, D. K. Sardar, B. Zandi, A. Burger, and N. N. Roy, *J. Appl. Phys.* **100**, 043108 (2006).; S. Y. Kuo, C. S. Chen, T. Y. Tseng, S. C. Chang, and W. F. Hsieh, *J. Appl. Phys.* **92**, 1868 (2002).
- [12] S. Y. Kuo, C. T. Li, and W. F. Hsieh, *Appl. Phys. Lett.* **81**, 3019 (2002).
- [13] M. A. Chamarro, and R. Cases, *J. Lumin.* **42**, 267 (1988).
- [14] M. Pollnau, D. R. Gamelin, S. R. Luethi, H. U. Gudel, and M. P. Hehlen, *Phys. Rev. B* **61**, 3337 (2000).

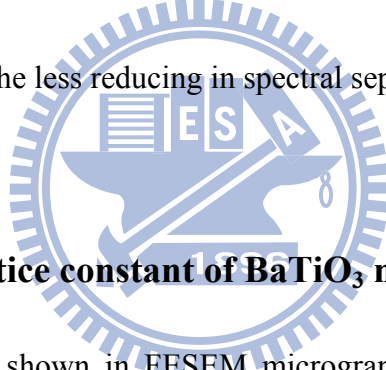
# Chapter 6 Size-dependent lattice dynamics of BaTiO<sub>3</sub> nanoparticles

Influence of the presence of substitution on the physical properties has been discussed in Chapters 4 and 5. It is similar to the results reported by Kuo *et al.* [1]. Furthermore, the physical properties have been dramatically influenced by various effects, such as temperature [2-4], pressure [3, 5], substitution [6], and size [7-11]. Continuous advance in miniaturization of ferroelectric devices, fine particles as ferroelectric materials have been applied in advanced electric devices [12] such as multilayer ceramic capacitor. Due to the close relationship between ferroelectric properties and crystal structure, the size dependence of structure is presently the major research topics.



In previous study of Ba<sub>x</sub>Sr<sub>1-x</sub>TiO<sub>3</sub> (BST) system [1], the repulsion of giant LO-TO splitting with increasing “Sr” substitution, which causes crystal structure to change from tetragonal phase toward cubic phase, is due to decrease in the dimensions of the unit cell. In this chapter we report, in contrast to that in BST system, the attractive LO-TO splitting behavior and depict the low frequency TO spectral peak along with change of the tetragonal phase toward the cubic one for reducing diameter of BaTiO<sub>3</sub> nanocrystals from 140 nm to 30 nm.

By applying single tetragonal-phase model to refine the crystal structure and the coupled-phonon model to analyze transverse optical (TO) modes of BaTiO<sub>3</sub> nanocrystals, we found, upon decreasing the particle size from 140 nm to 30 nm, the tetragonality of BaTiO<sub>3</sub> nanocrystallites is reduced accompanied with expanding unit-cell volume, which is the dominant mechanism for reducing giant LO–TO splitting in BaTiO<sub>3</sub> system. The weakening coupling of two low-frequency modes among three A<sub>1</sub>(TO) phonons leads to change the lowest one from a spectral dip to a peak; whereas the increasing coupling strength between two high-frequency modes, repels them farther so that the less reducing in spectral separation.



## 6.1 Size-dependent lattice constant of BaTiO<sub>3</sub> nanoparticles

BaTiO<sub>3</sub> nanoparticles shown in FESEM micrographs of Figure 6.1 have low aggregation and narrow size distribution with mean diameters of about 140, 60, and 30 nm, respectively. To analyze the crystal symmetry of BaTiO<sub>3</sub> nanoparticles, high resolution diffraction patterns of various sizes of BaTiO<sub>3</sub> nanoparticles were taken by using high-energy synchrotron radiation x-ray and refined by using the GSAS program; however, to retrench the layout of a printed page, here we just showed the refinement result of BaTiO<sub>3</sub> with a particle size of 60 nm in Figure 6.2. The XRD profiles around 32.5° in 2θ-scan for all sizes of BaTiO<sub>3</sub> particles indicate splitting of

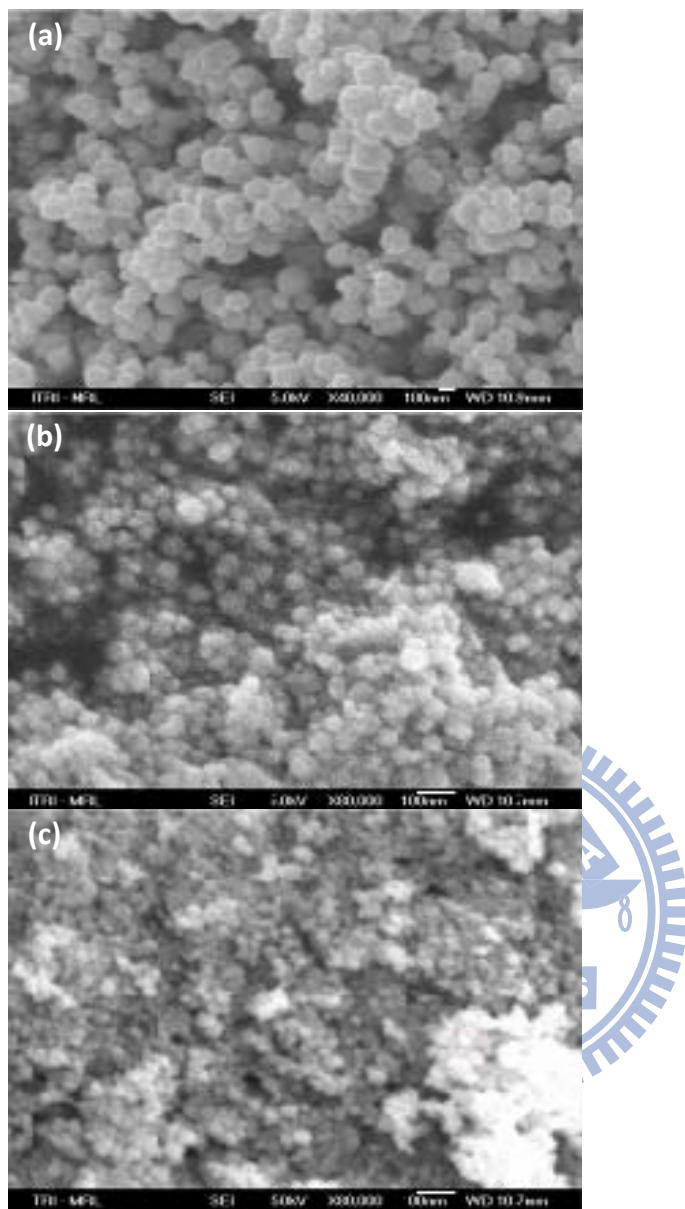


Figure 6.1: Microstructure (FESEM) of  $\text{BaTiO}_3$  nanoparticles with average grain size of  $140 \pm 8 \text{ nm}$ ,  $60 \pm 6 \text{ nm}$ ,  $30 \pm 5 \text{ nm}$ .

(004) and (400) peaks, thus, a tetragonal single phase (*P4mm*) model was applied to refine the crystal structure with the XRD data. As shown in Figure 6.2, the calculated profiles agree well with the observed ones. The refined structure parameters with very small deviations and reliability ( $R_{wp}$ ) factors for various sizes of

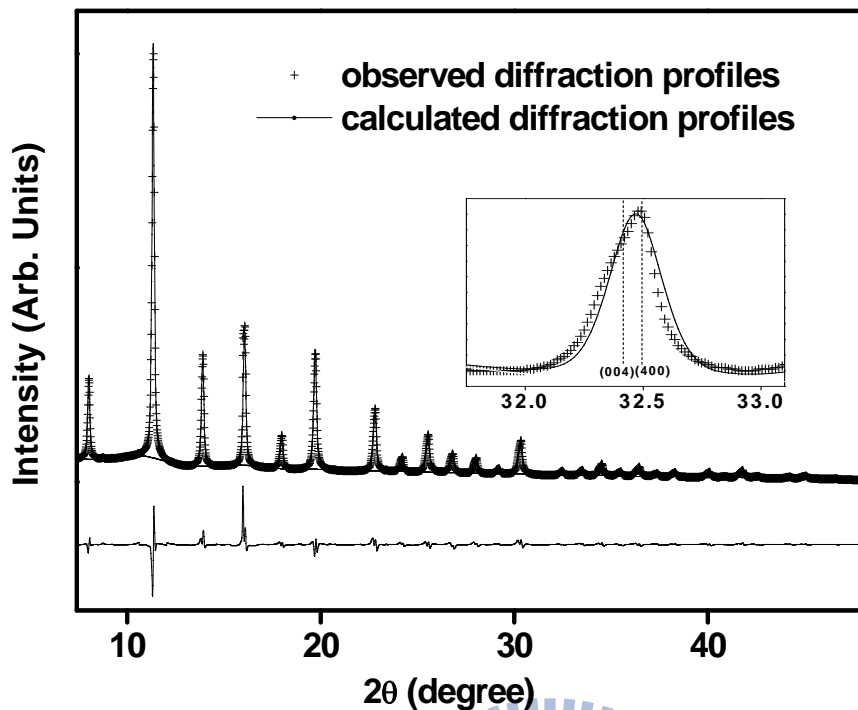
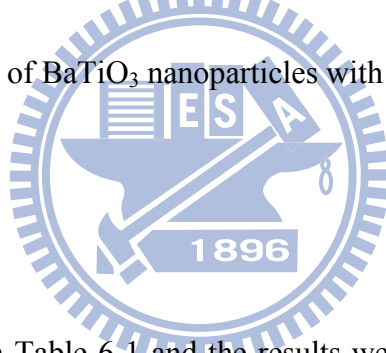


Figure 6.2: Rietveld pattern of  $\text{BaTiO}_3$  nanoparticles with average grain size of 60 nm.



nanoparticles were listed in Table 6-1 and the results were plotted in Figure 6.3. It reveals that single tetragonal-phase model is suitable for particle size smaller than 100 nm and even gets better fitting with lower  $R_{wp}$  as decreasing particle size. It is consistent with the results of Yoon, *et al.* [13] that single tetragonal phase was used for 7.5 nm, although Yashima, *et al.* [11] reported that particles with a size of 40 nm identified to be a mixture of tetragonal and hexagonal phases. Besides, the ratio  $c/a$  is  $1.0008 \pm 0.0003$ , which is still greater than 1, reveals the 30nm particle is still tetragonal, we will show later the results of Raman spectra provide auxiliary evidence

that the phonon modes specific to the tetragonal phase of  $\text{BaTiO}_3$  as described in Ref. [14] still appear. We also fitted a cubic model to the XRD pattern of the 30 nm particles. The resultant lattice constant is  $4.0341 \pm 0.0001$  nm and reliability ( $R_{wp}$ ) factors is 7.1%, which is acceptable but worse than 2.78% that fits with tetragonal model. Furthermore, the larger  $R$ -value for the larger particles may result from preferred orientation may exist in the larger particles that we did not consider in the refinement.

**TABLE 6-1** Refined crystal parameters and reliability factors of  $\text{BaTiO}_3$  nanoparticles.

| Particle size                  | $R_{wp}$ | $a, \text{\AA}$          | $c, \text{\AA}$          | $c/a$                     | Atomic coordinate    |                      |
|--------------------------------|----------|--------------------------|--------------------------|---------------------------|----------------------|----------------------|
|                                |          |                          |                          |                           | Ti                   | O(I)                 |
| $\sim \mu\text{m}$             |          | 3.9940                   | 4.0330                   | 1.0098                    |                      |                      |
| 140 nm<br>$(\pm 7 \text{ nm})$ | 11.20%   | 4.0200<br>$(\pm 0.0001)$ | 4.0304<br>$(\pm 0.0002)$ | 1.0026<br>$(\pm 0.00007)$ | $(0.5, 0.5, 0.5340)$ | $(0.5, 0.5, 0.0299)$ |
| 60 nm<br>$(\pm 6 \text{ nm})$  | 7.46%    | 4.0285<br>$(\pm 0.0004)$ | 4.0357<br>$(\pm 0.0008)$ | 1.0018<br>$(\pm 0.0002)$  | $(0.5, 0.5, 0.5201)$ | $(0.5, 0.5, 0.0160)$ |
| 30 nm<br>$(\pm 5 \text{ nm})$  | 2.78%    | 4.0329<br>$(\pm 0.0006)$ | 4.0362<br>$(\pm 0.0012)$ | 1.0008<br>$(\pm 0.0003)$  | $(0.5, 0.5, 0.5184)$ | $(0.5, 0.5, 0.0061)$ |

The lattice constants  $a$  and  $c$ , shown in Figure 6.3(a), simultaneously relax with decreasing the particle size from 140 nm to 30 nm. The results also show consistent with the assumption proposed by Ishikawa, *et al.* [15] that the tetragonality ( $c/a$ ) declines from 1.0026 to 1.0008 with expanding unit-cell volume in Figure 6.3(b) as the particle size decreases. The observation is also consistent with the results

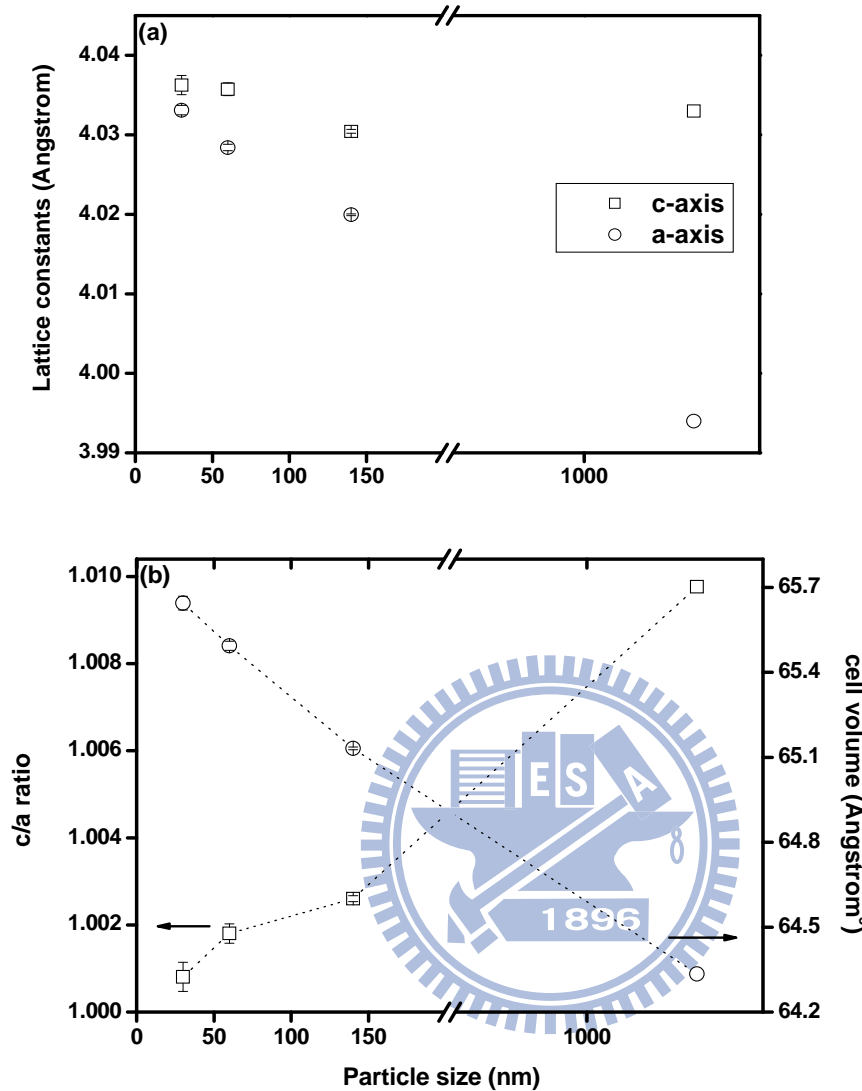


Figure 6.3: The lattice constants  $a$  and  $c$  of  $\text{BaTiO}_3$  nanoparticles after Rietveld refinement procedure and the ratio of  $c/a$ .

presented in Figure 6.1 of Ref. [10] that  $c$  reduces from micrometer size to sub- $\text{m}$  size then increases for further decreasing its size, whereas,  $a$  expands for decreasing crystal size. Nevertheless, our results of XRD refinement reveal the critical size of  $\text{BaTiO}_3$  nanoparticles, which is the size of the phase transition from tetragonal to

cubic at RT, may be smaller than 30 nm that differs from the argument reported by Hoshina, *et al.* [10], in which the size-induced phase transition occurs between 40 nm and 30 nm. According to Table 6-1 the refined atom positions in a unit cell of the tetragonal BaTiO<sub>3</sub> nanoparticles reveal less displacement of titanium and oxygen [O(I)] atoms along the *c* axis with decreasing particle size. It also indicates, similar to the results due to the temperature effect [16], that the Ti-O<sub>6</sub> octahedron shows less distorted due to the less off-center displacement (Ti) resulting from the size effect.

## 6.2 Size-dependent Raman spectra of BaTiO<sub>3</sub> nanoparticles

The Raman spectra of BaTiO<sub>3</sub> nanoparticles taken at RT were plotted in Figure 6.4 with particle sizes of 30 nm, 60 nm, 140 nm, and  $>1\text{ }\mu\text{m}$ , respectively. First of all, there is a spectral dip around  $180\text{ cm}^{-1}$  for micrometer-size sample but a spectral peak for all the nanoparticles that is assigned to  $A_1(\text{TO}_1)$  phonon mode. They are basically located at the same frequency of the destructive interference dip for the bulk BaTiO<sub>3</sub>. A broad band around  $260\text{ cm}^{-1}$  attributed to  $A_1(\text{TO}_2)$  mode, a band at  $305\text{ cm}^{-1}$  to  $B_1+E(\text{TO+LO})$  modes, the asymmetric band around  $520\text{ cm}^{-1}$  to  $E(\text{TO})$  and  $A_1(\text{TO}_3)$  modes, and the highest frequency band around  $720\text{ cm}^{-1}$  to  $A_1(\text{LO})+E(\text{LO})$  phonon modes. The phonon modes at  $305$  and  $720\text{ cm}^{-1}$  specific to the tetragonal phase of BaTiO<sub>3</sub> as described in Ref. [14] become weak and broad with decreasing

particle size. The observed broadening and weakening of tetragonal Raman bands indicate that the crystal structure becomes progressively less tetragonal due to less displacements of Ti and O(I) atoms for the smaller particle size, which is consistent with the results of XRD. The Structural model of non-polar (cubic) and polar (tetragonal)  $\text{ABO}_3$  crystal is shown in Figure 6.5. Ti atoms locate at the center of the  $\text{Ti-O}_6$  octahedron when the octahedral units are perfect in the cubic-type structure.

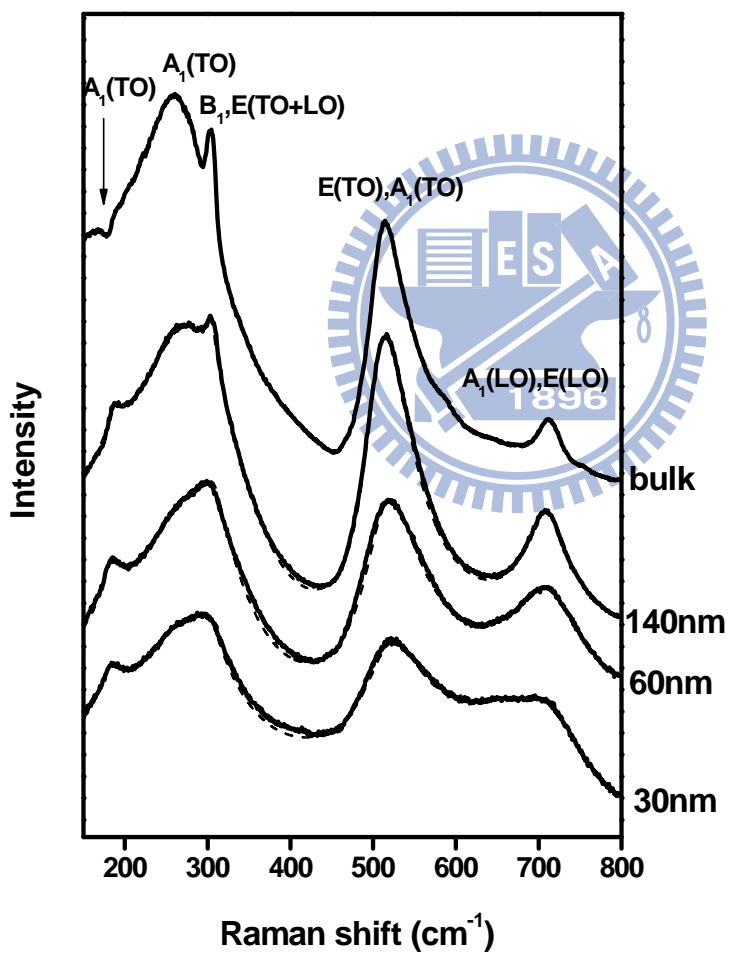


Figure 6.4: Size dependence of Raman spectra for  $\text{BaTiO}_3$  bulk ( $> 1\mu\text{m}$ ) and nanoparticles of diameter 140, 60, and 30 nm, respectively.

Due to balance of the charges, the crystal is non-polar and Raman mode is inactive. On reducing temperature, the  $\text{Ti-O}_6$  octahedron will be somewhat distorted with off-center displacement of Ti atoms toward one of the O(I) atoms while elongating the  $c$ -axis to the tetragonal structure and present spontaneous dipole. The refined atom positions in a unit cell of the tetragonal  $\text{BaTiO}_3$  nanoparticles reveal less displacement of titanium and oxygen [O(I)] atom along the  $c$  axis with decreasing particle size so that the  $\text{Ti-O}_6$  octahedron shows less distorted or less polar due to the less Ti off-center displacement resulting from the size effect.

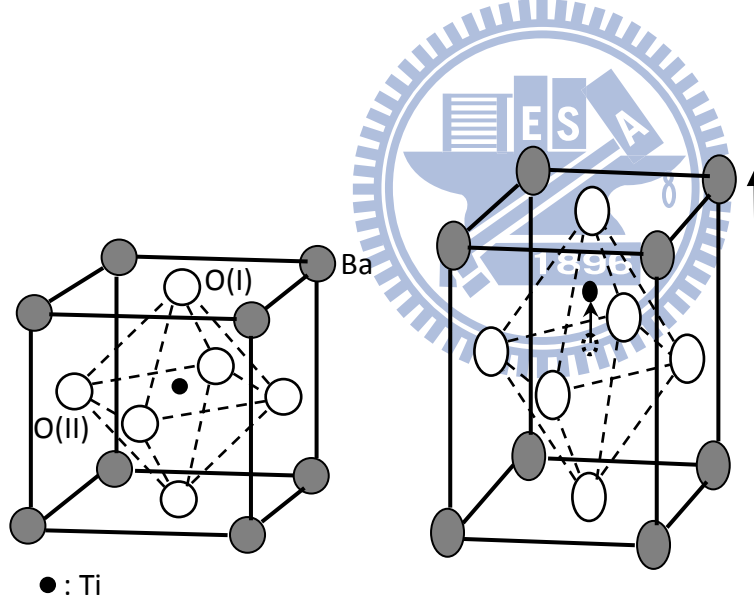


Figure 6.5: Structural model of the cubic- and tetragonal- phase occurring with bulk  $\text{BaTiO}_3$  crystals.

Although we had also observed a weak peak around  $810 \text{ cm}^{-1}$  attributed to lattice OH group [17] and a very weak band around  $930 \text{ cm}^{-1}$  (not shown here) to the oxygen vacancy [18]. There are no reports on the OH groups and no direct evidence of

oxygen vacancy that would influence the frequencies of the observed Raman modes.

The frequency shift observed in Ref. 31 should mainly result from the interface strain introduced between  $\text{BaTiO}_3$  film and substrate rather than influence of oxygen vacancy, because spectra (b) and (c) in Figure 6.4 showed therein that the  $A_1(\text{LO})+E(\text{LO})$  modes shifted to  $715 \text{ cm}^{-1}$  before appearance of a very weak  $930 \text{ cm}^{-1}$  band due to the oxygen vacancy. Finally, we did not observe  $1060 \text{ cm}^{-1}$  peak attributed to  $\text{BaCO}_3$  brought out by Pithan, *et al.* [19] so that we had prevented the  $\text{BaCO}_3$  related peaks located in the spectral range below  $200 \text{ cm}^{-1}$  by acetic acid washing.

Because the three  $A_1(\text{TO})$  modes are strongly coupled and two of them are heavily damped in the tetragonal phase of  $\text{ABO}_3$ , Sood, [20] and Chaves, *et al.* [21] have considered three coupled  $A_1(\text{TO})$  modes to describe the complicated coupling phenomenon. The Raman intensity of the three coupled modes can be expressed by

$$I(\omega) = A [n(\omega)+1] \text{ Im}[\mathbf{T}^* \mathbf{G} \mathbf{T}], \quad (6-1)$$

where  $A$  is a constant,  $[n(\omega)+1]$  is Bose-Einstein factor,  $\mathbf{T}$  is a vector involving Raman scattering amplitudes, and the inverse matrix response is

$$\mathbf{G}^{-1}(\omega) = \mathbf{\Omega}^2 - \omega^2 \mathbf{I} - i\omega \mathbf{\Gamma}. \quad (6-2)$$

In Eq. (6-2),  $\mathbf{I}$  is the unit matrix,  $\mathbf{\Omega}^2$  is the force constant matrix, and  $\mathbf{\Gamma}$  is the damping matrix:

$$\boldsymbol{\Omega}^2 = \begin{pmatrix} \omega_1^2 & \omega_{12}^2 & 0 \\ \omega_{12}^2 & \omega_2^2 & \omega_{23}^2 \\ 0 & \omega_{23}^2 & \omega_3^2 \end{pmatrix}, \boldsymbol{\Gamma} = \begin{pmatrix} \Gamma_1^2 & 0 & 0 \\ 0 & \Gamma_2^2 & 0 \\ 0 & 0 & \Gamma_3^2 \end{pmatrix}. \quad (6-3)$$

Here  $\omega_i$  and  $\omega_{ij}$  ( $i, j = 1, 2, 3$ ) are the uncoupled mode frequencies and the coupling strengths between modes  $i$  and  $j$ . The coupling between the lowest ( $\omega_1$ ) and the highest ( $\omega_3$ ) modes was set to zero ( $\omega_{13} = 0$ ), to allow less fitting parameters; this is a reasonable approximation because they are too far from each other, having no spectral superimposition.

The asymmetric broad band around 500-600 cm<sup>-1</sup> is attributed to superposition of  $E(\text{TO})$  and  $A_1(\text{TO}_3)$  modes, so that one has to separate them before making coupled-mode analysis. These two modes are distinguishable by polarized Raman scattering in single crystals. From the results of polarized Raman study on the epitaxial BaTiO<sub>3</sub> film by Marssi, *et al.* [22], the  $E(\text{TO})$  mode is situated at the low frequency shoulder with about 1/4 intensity of the  $A_1(\text{TO}_3)$  mode. According to the process to refine the XRD data by using the GSAS, we can attain better fitting result in XRD analysis without considering any preferred orientation. Therefore, in our powder samples the particles should possess random orientation. We have to consider the angle dependent frequencies of these modes. It is well known that the frequency of  $E(\text{TO})$  mode is independent of the observing angle with respect to the crystallographic axes, whereas, that of  $A_1(\text{TO})$  mode depends upon the observing

angle according to: [23]

$$[\omega_{A_1}(\theta)]^2 = (\omega_{A_1})^2 \sin^2 \theta + (\omega_E)^2 \cos^2 \theta \quad (6-4)$$

Assuming the particles are completely randomly oriented, the scattering wave vector should also randomly orient with respect to the crystallographic axis. Therefore, the observed  $A_1(\text{TO}_3)$  frequency, after averaging over  $\theta$  for Eq. (6-4) is well-defined between  $\omega_{A_1}$  and  $\omega_E$  or  $\langle \omega_{A_1}(\theta) \rangle = \sqrt{\frac{\omega_{A_1}^2 + \omega_E^2}{2}}$  and  $E(\text{TO})$  and  $A_1(\text{TO}_3)$  modes are separable. It is reasonable to extract the contribution of the  $E(\text{TO})$  mode and the coupled  $A_1(\text{TO}_3)$  mode for these randomly oriented nanoparticles. On the other hand,  $A_1(\text{LO})$  mode is inseparable from  $E(\text{LO})$  mode for tetragonal structure around  $720 \text{ cm}^{-1}$  when the scattering wave vector makes an angle with respect to crystallographic axes. It gives rise to mode mixing due to directional dispersion or called the “oblique phonon”. The observed frequency shift of angle-averaged oblique phonon in Figure 6.4 should not depend on the observing angle  $\theta$  but other effects, e.g., particle size. Therefore, other than Eq. (6-1) we added four Lorentzian functions representing background signal (Rayleigh scattering) which depends on the particle size,  $B_1+E(\text{TO+LO})$ ,  $E(\text{TO})$ , and  $A_1(\text{LO}_3)+E(\text{LO})$  to fit the measured Raman spectra.

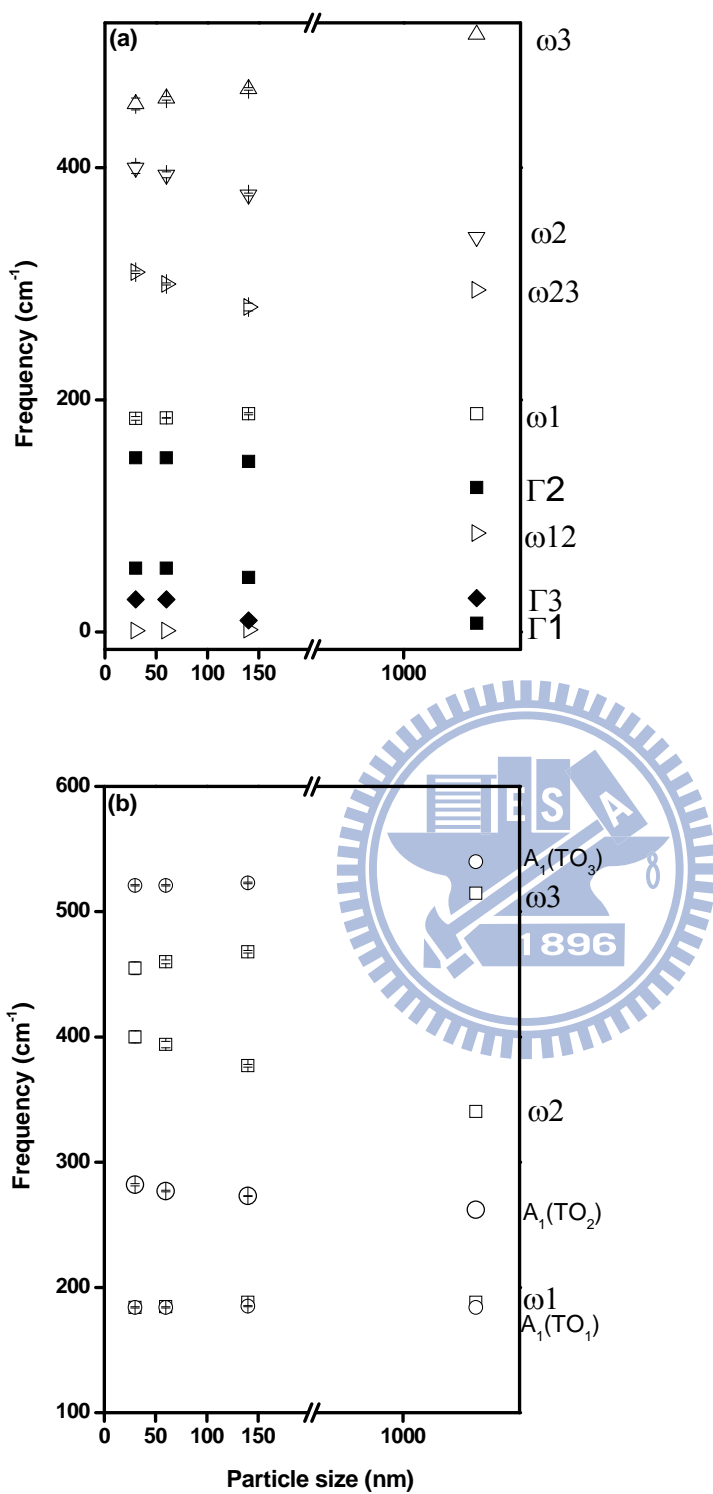


Figure 6.6: The fitted parameters using the coupled-phonon model as a function of particle size.

In order to attain the best fitting to our measured data, an extra band around  $640\text{ cm}^{-1}$  has to be considered especially for 60-nm and 30-nm samples. This  $640\text{ cm}^{-1}$  band was assigned to the grain-boundary regions [24] or was due to the hexagonal phase [11]. However, as aforementioned there is even better fitting with smaller  $R_{wp}$  for size of 30 nm in XRD analysis using single tetragonal phase, we therefore assigned the weak mode around  $640\text{ cm}^{-1}$  to the grain-boundary regions for 60-nm and 30-nm samples rather than due to the hexagonal phase.

The fitting parameters of three coupled TO modes were plotted in Figure 6.6(a) that allows us to clarify the coupling behavior of phonon with decreasing particle size. We found that the coupling strength,  $\omega_{12}$ , between  $\omega_1$  and  $\omega_2$  dramatically changes from  $85\text{ cm}^{-1}$  to nearly zero as the particle size decreases from few micrometers to nanometer. The weaker (or zero) coupling between  $\omega_1$  and  $\omega_2$  in  $\text{BaTiO}_3$  nanoparticles leads to observing a spectral peak around  $180\text{ cm}^{-1}$  for the  $A_1(\text{TO}_1)$  phonon mode rather than a dip at the same position. Figure 6.6(b) shows the plot of the as-read peak positions (hollow symbols and labeled as  $A_1(\text{TO}_i)$ ,  $i = 1, 2, 3$ ) of three  $A_1$ -symmetric TO modes from our Raman data and those obtained from the coupled-phonon model as solid symbols. It can be seen that the size-dependent decoupled (calculated) phonon frequency  $\omega_1$  overlaps with the as-read one again indicating weak coupling strength ( $\omega_{12} \sim 0$ ). With less tetragonality or small  $c/a$  due

to decreasing the particle size, we found that the approach of uncoupled  $\omega_2$  and  $\omega_3$  results in slightly increasing in  $\omega_{23}$ . The larger coupling strength ( $\omega_{23} \sim 300 \text{ cm}^{-1}$ ) repels these two modes farther such that the measured  $A_1(\text{TO}_2)$  [ $A_1(\text{TO}_3)$ ] peak only slightly shifts toward the higher (lower) frequency upon decreasing the particle size.

### 6.3 Born effective charge and LO-TO splitting in $\text{BaTiO}_3$ nanoparticles system

Furthermore, the dynamical matrices for the LO and TO modes, which have the same form of atomic displacements in a unit cell, are related by

$$D_{mn}^{LO} = D_{mn}^{TO} + \frac{4\pi e^2}{V} \frac{Z_m^* Z_n^*}{\epsilon_\infty(q)}, \quad (6-5)$$

where  $D$  represents the dynamical matrix that is proportional to the square of the vibration frequency,  $V$  is the volume of the unit cell,  $\epsilon_\infty(q)$  is the optical dielectric constant, and  $Z^*$  is the Born effective charge of the corresponding vibration. The Coulomb interaction would play an important role in the behavior of LO-TO splitting.

Figure 6.7 shows the peak positions of  $A_1(\text{LO})$  and  $A_1(\text{TO}_1)$  modes versus  $\text{BaTiO}_3$  particle size. We observed besides the expected softening of both  $A_1(\text{LO})$  and  $A_1(\text{TO}_1)$  modes, there is a decreasing trend of LO-TO splitting as the particle size decreases from  $> 1\mu\text{m}$  to 30 nm. Since Ba-based  $\text{ABO}_3$  perovskites basically

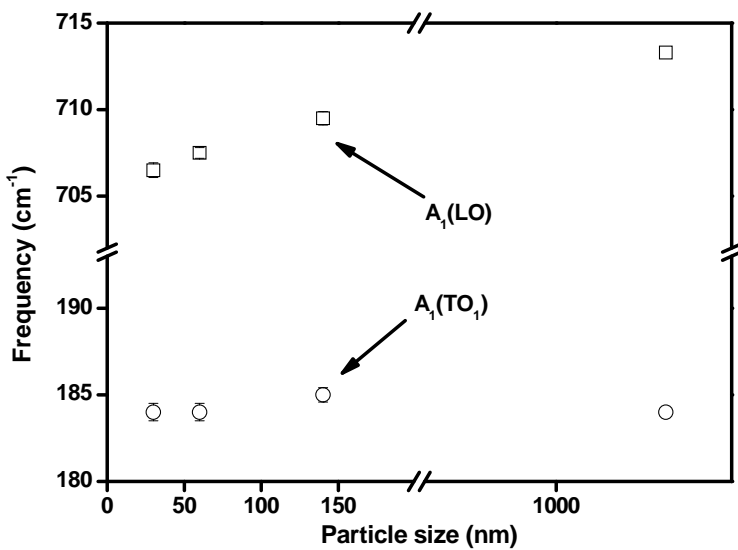


Figure 6.7: The LO-TO splitting of the  $A_1(\text{LO}_3)$  and  $A_1(\text{TO}_1)$  modes as function of particle size.

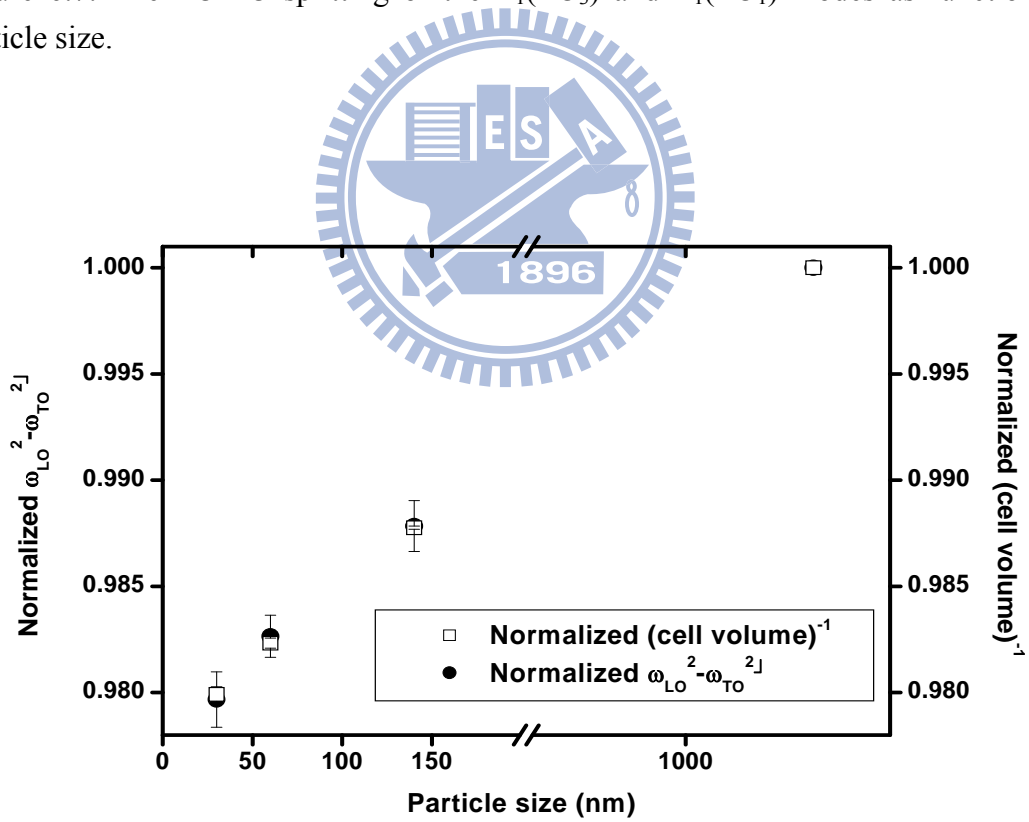


Figure 6.8: Normalized square difference of phonon frequencies of  $A_1(\text{LO}_3)$  and  $A_1(\text{TO}_1)$  and normalized reciprocal of unit cell volume for nanometer size samples to the micrometer size.

possesses ionic bonding [25, 26-28], the Born effective charge would not be influenced by change of structure [29, 27]. From the results of Figure 6.3(b) that the unit cell dimension of  $\text{BaTiO}_3$  particles increases with the particle decreasing from micrometer size to 30 nm; we would expect reducing LO-TO splitting. Relatively, we previously reported that the tetragonality declines with unit-cell volume diminishing as  $x$  changes from 1 to 0.7 in polycrystalline  $\text{Ba}_x\text{Sr}_{1-x}\text{TiO}_3$  [6]. Change of unit-cell volume was considered the dominant mechanism of increasing the LO-TO splitting in this system with negligible change of effective charge due to the substitution. In this study we directly observed the decreasing LO-TO splitting with the decline of tetragonality by decreasing the size of  $\text{BaTiO}_3$  nanoparticles which causes expansion of the unit-cell volume.

Based on Eq. (6-5), we normalized the square difference of phonon frequencies of  $A_1(\text{LO}_3)$  and  $A_1(\text{TO}_1)$  for nanometer size samples to the one of micrometer-size and plotted in Figure 6.8 to compare with the normalized reciprocal of unit cell volume also to the micrometer-size one's. It shows that the normalized square difference of phonon frequencies of  $A_1(\text{LO}_3)$  and  $A_1(\text{TO}_1)$  almost coincides with the normalized reciprocal unit cell volume with less than 2% deviation. This result indicates that the

value of  $\frac{4\pi e^2 Z_m^* Z_n^*}{\varepsilon_\infty(q)}$  is a constant, namely, the Born effective charges should not be

influenced by change of structure or size, and the change of unit-cell volume is the dominant mechanism for the tendency of the LO–TO splitting in BaTiO<sub>3</sub> system without complication of ion replacement.

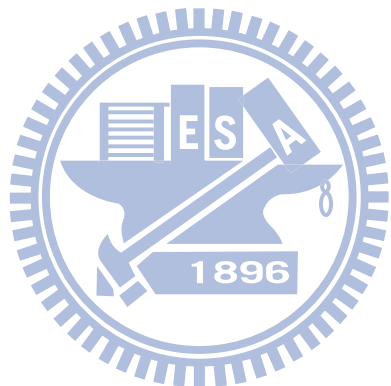
## 6.4 Summary

The size effect on structure for BaTiO<sub>3</sub> nanoparticles synthesized by the glycothermal method has been investigated using FESEM, synchrotron XRD, and Raman spectroscopy. We further applied a single tetragonal-phase model to refine the crystal structure and the coupled-phonon model to analyze the coupled  $A_1$ (TO) modes upon particle size decreasing from 140 nm to 30 nm. We explained that the weak strength of coupling between  $A_1$ (TO<sub>1</sub>) and  $A_1$ (TO<sub>2</sub>) leads to a change from a spectral dip at 180 cm<sup>-1</sup> for  $A_1$ (TO<sub>1</sub>) phonon to a peak at the same position and found that the approach of uncoupled  $\omega_2$  and  $\omega_3$  with less tetragonality due to decreasing the particle size results in slightly increasing in  $\omega_{23}$ . The larger coupling strength repels these two modes farther so that the less reducing in spectral separation. According to the results of decomposition, we also observed the decreasing LO–TO splitting with the decline of tetragonality and expansion of the unit-cell volume. And the change of unit-cell volume is the dominant mechanism for the tendency of the LO–TO splitting in BaTiO<sub>3</sub> system without complication of ion replacement.

## References

- [1] S. Y. Kuo, C. T. Li, and W. F. Hsieh, *Appl. Phys. Lett.* 81, 3019 (2002).
- [2] R. Pirc and R. Blinc, *Phys. Rev. B* 70, 134107 (2004).
- [3] J. Iñiguez and D. Vanderbilt, *Phys. Rev. Lett.* 89, 115503 (2002).
- [4] D. Damjanovic, F. Brem, and N. Setter, *Appl. Phys. Lett.* 80, 652 (2002).
- [5] U. D. Venkateswaran, V. M. Naik, and R. Naik, *Phys. Rev. B* 58, 14256 (1998).
- [6] S. Y. Kuo, W. Y. Liao, and W. F. Hsieh, *Phys. Rev. B* 64, 224103 (2001).
- [7] M. H. Frey and D. A. Payne, *Phys. Rev. B* 54, 3158 (1996).
- [8] S. Tsunekawa, S. Ito, T. Mori, K. Ishikawa, Z. Q. Li, and Y. Kawazoe1, *Phys. Rev. B* 62, 3065 (2000).
- [9] Z. Zhao, V. Buscaglia, M. Viviani, M. T. Buscaglia, L. Mitoseriu, A. Testino, M. Nygren, M. Johnsson, and P. Nanni, *Phys. Rev. B* 70, 024107 (2004).
- [10] T. Hoshina, H. Kakemoto, T. Tsurumi, S. Wada, and M. Yashima, *J. Appl. Phys.* 99, 054311 (2006).
- [11] M. Yashima, T. Hoshina, D. Ishimura, S. Kobayashi, W. Nakamura, T. Tsurumi, and S. Wada, *J. Appl. Phys.* 98, 014313 (2005).
- [12] D. H. Yoon and B. I. Lee, *J. Eur. Ceram. Soc.* 24 753 (2004).
- [13] S. Yoon, S. Baik, M. G. Kim and N. Shin, *J. Am. Ceram. Soc.* 89 [6] 1816 (2006).
- [14] R. Naik, J. J. Nazarko, C. S. Flattery, U. D. Venkateswaran, V. M. Naik, M. S. Mohammed, G. W. Auner, J. V. Mantese, N. W. Schubring, A. L. Micheli, and A. B. Catalan, *Phys. Rev. B* 61, 11367 (2000).
- [15] K. Ishikawa and T. Uemori, *Phys. Rev. B* 60, 11841 (1999).
- [16] G. Kwei, S. J. L. Billinge, S. W. Cheong, and J. G. Saxton, *Ferroelectrics* 164, 57 (1995).
- [17] G. Busca, V. Busglia, M. Leoni, and P. Nanni, *Chem. Mater.* 6, 955 (1994).
- [18] H. Z. Guo, Z. H. Chen, B. L. Chenf, H. B. Lu, L. F. Liu, and Y. L. Zhou, *J. Europ. Ceram. Soc.* 25, 2347 (2005).
- [19] C. Pithan, Y. Shiratori, and R. Waser, *J. Am. Cerm. Soc.* 89, 2908 (2006).
- [20] A. K. Sood, N. Chandrabhas, D. V. S. Muthu, and A. Jayaraman, *Phys. Rev. B* 51, 8892 (1995).
- [21] A. Chaves, R. S. Katiyar, and S. P. S. Porto, *Phys. Rev. B* 10, 3522 (1974).
- [22] M. E. Marssi, F. L. Marrec, I. A. Lukyanchuk, and M. G. Karkut, *J. Appl. Phys.* 94, 3307 (2003).
- [23] G. Burns and B. A. Scott, *Phys. Rev. B* 7, 3088 (1973).
- [24] U. D. Venkateswaran, V. M. Naik, and R. Naik, *Phys. Rev. B* 58, 14256 (1998).
- [25] R. E. Cohen, *Nature (London)* 358, 136 (1992).

- [26] Y. Kuroiwa, S. Aoyagi, and A. Sawada, *Phys. Rev. Lett.* 87, 217601 (2001).
- [27] S. Y. Kuo, C. T. Li, and W. F. Hsieh, *Appl. Phys. Letts.* 81(16), 3019 (2002).
- [28] J. C. Jan, H. M. Tsai, C. W. Pao, J. W. Chiou, K. Asokan, K. P. Krishna Kumar, W. F. Pong, Y. H. Tang, M. H. Tsai, S. Y. Kuo, and W. F. Hsieh, *Appl. Phys. Letts.* 87, 012103 (2005).
- [29] W. Zhong, R. D. King-Smith, and D. Vanderbilt, *Phys Rev. Lett.* 72, 3618 (1994).



# Chapter 7 Correlating phonon frequency shift with magnetoelectric effect in the $\text{PbTiO}_3\text{-CoFe}_2\text{O}_4$ multiferroic system due to interfacial stress

We discussed the substitution effect on perovskite structure in Chapters 4 and 5 and size effect in the last chapter. In this chapter, we continue to discuss the influence of strain effect resulting from the lattice misfit between the different media on ferroics.

The ME coupling results from the elastic bonding at the interface and is transmitted through the stress/strain exerted by magnetized magnetostrictive phase on piezoelectric phase or vice versa along their boundary and hence it induces a net polarization or magnetization [1, 2, 3]. Moreover, it is well known that the behavior of interfacial phonon is sensitive to the giant residual stress/strain resulting from the lattice misfit between the different media [4]. It is interesting and important to investigate the relationship between the ME effect and the behavior of interfacial phonon. Recently, some studies about the behavior of phonon on multiferroics were reported [5-7] with lack of concrete conclusion.

In this chapter, we report on the stress dependence of the behavior of interfacial phonon and the magnetic properties in three multiferroics consisting of the different

geometric shapes (see Figure 7.1 ) of ferromagnetic  $\text{CoFe}_2\text{O}_4$  (CFO) embedded in ferroelectrics  $\text{PbTiO}_3$  (PTO) by using the micro-Raman spectroscopy and superconducting quantum interference device (SQUID). Their energy of interfacial phonon and ferromagnetic properties depend on stress due to not only the lattice misfit but also the degree of chemical bonding at the interface between CFO and PTO matrices. The disk-3 type structure, the self-assembled CFO disks embedded in PTO matrix, illustrates the strong elastic interactions between the two phases. The larger nonsymmetrical coercivity  $H_c$  and the absence of saturation magnetization  $M_s$  of CFO matches with the larger Raman shift of  $A_1(\text{TO}_2)$  and  $A_1(\text{TO}_3)$  modes of PTO found in the disk-3 type than the other types of the CFO and PTO multilayered structure and the CFO particles embedded in PTO matrix.

## 7.1 Microstructure and morphology

The top view images of the disk-3 type shown in Figure 7.2 by using OM and FESEM were found consisting of sub-10  $\mu\text{m}$  CFO discs embedded in PTO matrix rather than nanometer sized CFO rods in PTO matrix [2]. It reveals the similar morphology as illustrated in Figure 7.1(c). Forming the CFO discs instead of CFO rods may be due to the cohesion of CFO gel is stronger than the adhesive force between CFO and PTO gels. According to the mechanism of synthesis, we may infer that the CFO and PTO multilayered structure (2-2 type) and the CFO particles

embedded in PTO matrix (0-3 type) as illustrated in Figure 7.1(a) and Figure 7.1(b), respectively.

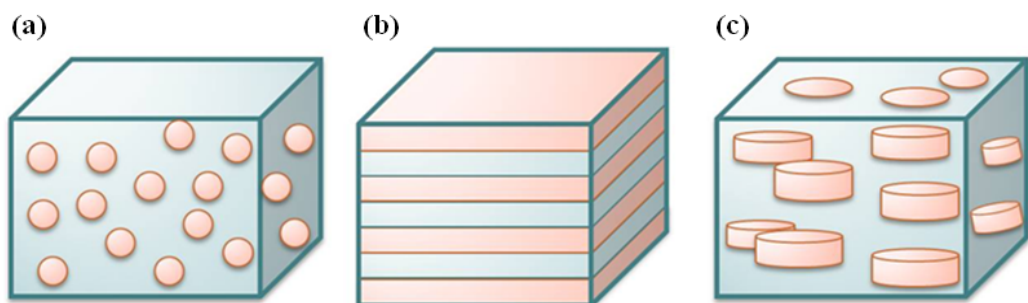


Figure 7.1: Schematic illustration of three thin films with different connectivity schemes: the 0-3 type with CFO particles embedded in PTO matrix, the 2-2 type with CFO and PTO nanolayers, and the disk-3 type with CFO disc aligned in PTO matrix.

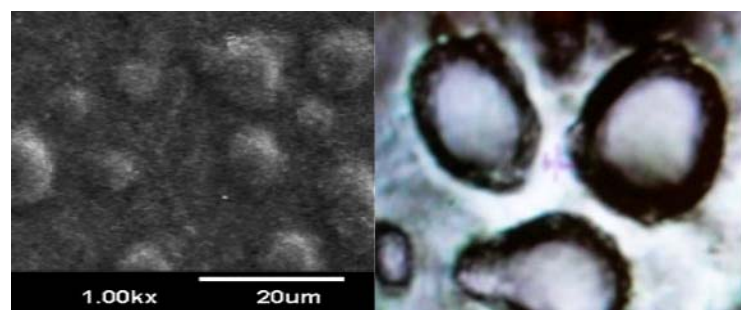
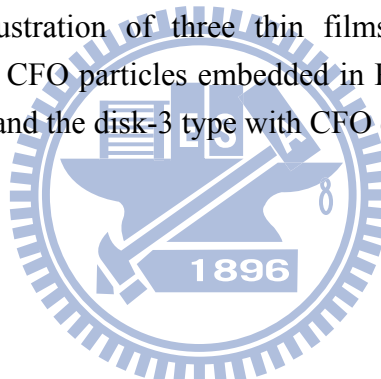


Figure 7.2: Top view of FESEM and OM images of the disk-3 type showing the CoFe<sub>2</sub>O<sub>4</sub> disks in the PbTiO<sub>3</sub> matrix.

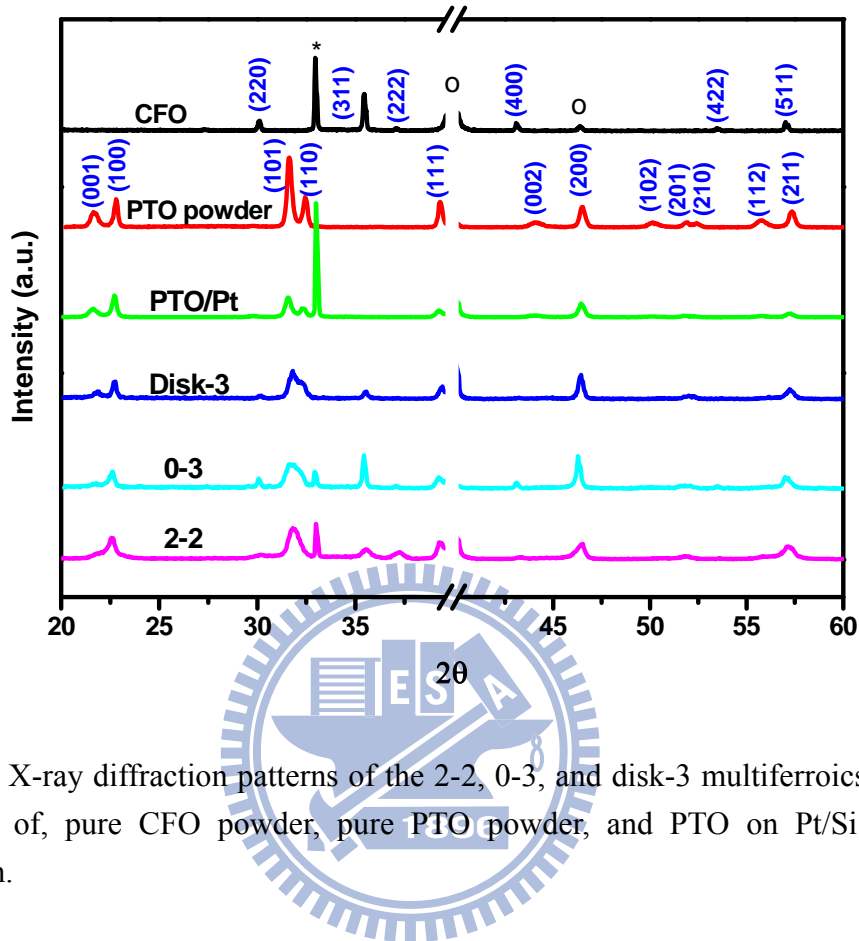


Figure 7.3: X-ray diffraction patterns of the 2-2, 0-3, and disk-3 multiferroics together with those of, pure CFO powder, pure PTO powder, and PTO on Pt/Si film for comparison.

The XRD patterns of the pure CFO and pure PTO powders, and three multiferroic films on Pt/Si substrates taken at RT as shown in Figure 7.3 reveal the correct phases with various planes without obvious secondary phases, and “\*” and “O” represent Si and Pt signals from the substrates, respectively. By using the refinement analysis of XRD data, the refined structure parameters were listed in Table 7-1 and Table 7-2. We also define strain as variation in lattice constant in this study.

**Table 7-1** The refined lattice parameters of PTO for the pure PTO powder and the films with different types

| PTO          |                         |        |           |        |           |        |
|--------------|-------------------------|--------|-----------|--------|-----------|--------|
| Samples      | $I_{(100)} / I_{(001)}$ | a(Å)   | Strain(%) | c(Å)   | Strain(%) | c/a    |
| Powder       | 1.9875                  | 3.8616 |           | 4.0189 |           | 1.0407 |
| PTO/Pt/Si    | 2.3722                  | 3.8869 | 0.6552    | 3.9817 | -0.9256   | 1.0244 |
| disk-3/Pt/Si | 2.9032                  | 3.8871 | 0.6604    | 3.9814 | -0.9331   | 1.0269 |
| 0-3/Pt/Si    | 3.1619                  | 3.8872 | 0.6629    | 3.9470 | -1.7890   | 1.0120 |
| 2-2/Pt/Si    | 3.6929                  | 3.9078 | 1.1964    | 3.9422 | -1.9085   | 1.0088 |

**Table 7-2** The refined lattice parameters of CFO for the films with different types

| CFO          |        |           |
|--------------|--------|-----------|
| Samples      | a(Å)   | Strain(%) |
| CFO/Pt       | 8.3873 |           |
| disk-3/Pt/Si | 8.3620 | -0.3016   |
| 0-3/Pt/Si    | 8.3866 | -0.0083   |
| 2-2/Pt/Si    | 8.3661 | -0.2528   |

According to Table 7-1, the result of pure PTO powder agrees with the JCPDS-International Center for Diffraction Data No. 78-0298; and its intensity ratio of diffraction peaks (100) and (001) is close to 2, indicating the random orientation. On the other hand, prefer-oriented vertical *a*-axis growth with the *c*-axis lying on the substrate surface is obvious in the 2-2 type and the 0-3 type films but is less in the disk-3 type film and pure PTO/Pt/Si film. We also found that the *a*-axis of PTO matrix is lengthening with the compression of *c*-axis for all type films and PTO/Pt/Si film. The compression of *c*-axis is the most obvious in 2-2 type and is the least in PTO/Pt/Si film. The lattice constant of Pt is about 3.9240 Å and that of CFO is

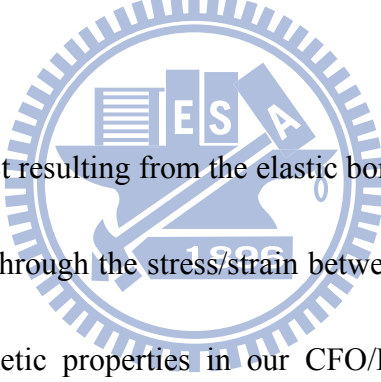
about 8.3873 Å. For PTO/Pt/Si film, the tensile stress of lattice  $a$  and the compressed one of lattice  $c$  in PTO matrix arise from mismatch of the Pt lattice, whose lattice constant lies in between them. The stain/stress of PTO matrix is due to the interface of PTO and Pt substrate only. However, for three multiferroic samples, the stress in PTO matrix arises from both the interface of PTO and Pt substrate and that of PTO and CFO matrices.

There are more than twice as many lattice constant of CFO (8.3873 Å) to those of PTO ( $a$ : 3.8616 Å,  $c$ : 4.0189 Å). Having the larger mismatch along  $a$  of PTO with CFO than along  $c$ , CFO exerts the larger tensile stress on the  $a$ -lattice of PTO. Therefore, the PTO matrices in all the CFO-embedded PTO samples are strongly elongated in  $a$ -axis that leads to compress in the  $c$ -axis for preserving the unit cell volume. Consequently, the decreasing trend of  $c/a$  for PTO matrix is not difficult to comprehend as a result of the tensile stress induces  $a$ -lattice elongation with the compressive  $c$ -axis.

From the information of lattice parameters of PTO matrices in Table 7-1, it is difficult to differentiate the stress/strain due to the interface of PTO and CFO matrices from that of PTO and Pt layer. We therefore predict the lattice parameters of the CFO matrices for all types of samples in Table 7-2 and find that the lattices of CFO matrices are compressed for all types. Because in three multiferroic films the CFO

matrices only bond to the PTO ones, the stresses exerted in CFO matrices should be only on the interfaces of PTO and CFO matrices. As mentioned previously, more than twice as many lattice constant of CFO to the PTO ones, PTO exerts compressive stress on the lattice of CFO. From Table 7-2, we found the most obvious compression is in the disk-3 type and the least compression in the 0-3 type for these three types of samples. Therefore, the train/stress caused by the lattice mismatch between the CFO and PTO matrices is the most pronounced in the disk-3 type and is the least in the 0-3 type that will be further confirmed by micro-Raman spectroscopy

later on..



The ME coupling effect resulting from the elastic bonding at the interface [1, 2, 3] should also be transmitted through the stress/strain between the interface of CFO and PTO matrices. The magnetic properties in our CFO/PTO multiferroics should be influenced by the stress/strain, thus it is more important to directly observe the interfacial stress/strain using another appropriate probe of local behavior besides the peak shifts of XRD diffractions of CFO which covers mm<sup>2</sup> area and sub- $\mu$ m depth. In the following study, we used SQUID to investigate the ferromagnetic properties in our multiferroics and the micro-Raman measurement system to probe the stress dependence of behavior of interfacial phonon, which is sensitive to the interfacial stress/strain.

## 7.2 Magnetic properties

We measured the RT magnetizations by applying the magnetic fields perpendicular and parallel to the surface of the films. Figure 7.4 shows the measured magnetic hysteresis loops for pure cobalt ferrite and different geometrical CFO contained multiferroics. The out-of-plane (Figure 7.4(a)) and the in-plane (Figure 7.4(b)) hysteresis loops of the 0-3 type are similar to that of the pure CFO powder in the values of coercivity  $H_c$ . It may result from the 0-3 type sample was made of dispersing pure CFO particles in PTO matrix, in which the chemical bonding between CFO particles and PTO matrix might not form. However, the saturation magnetization  $M_s$  of the 0-3 type for both the in-plane and out-of-plane loops is lower than that of the pure CFO powder. This discrepancy should result from the inaccuracy for estimating CFO volume % in the 0-3 type. Owing to inability to estimate CFO volume % of different geometric CFO contained multiferroics, we will not compare the values of saturation magnetization  $M_s$  among different types of samples.

The out-of-plane coercivity  $H_c$  under the positive magnetic field in Figure 7.4 are about 0.97, 1.01, 1.51, and 0.20 kOe in pure cobalt ferrite powder, 0-3, 2-2, and disk-3 types, respectively. Notice that the out-of-plane coercivity  $H_c$  of the disk-3

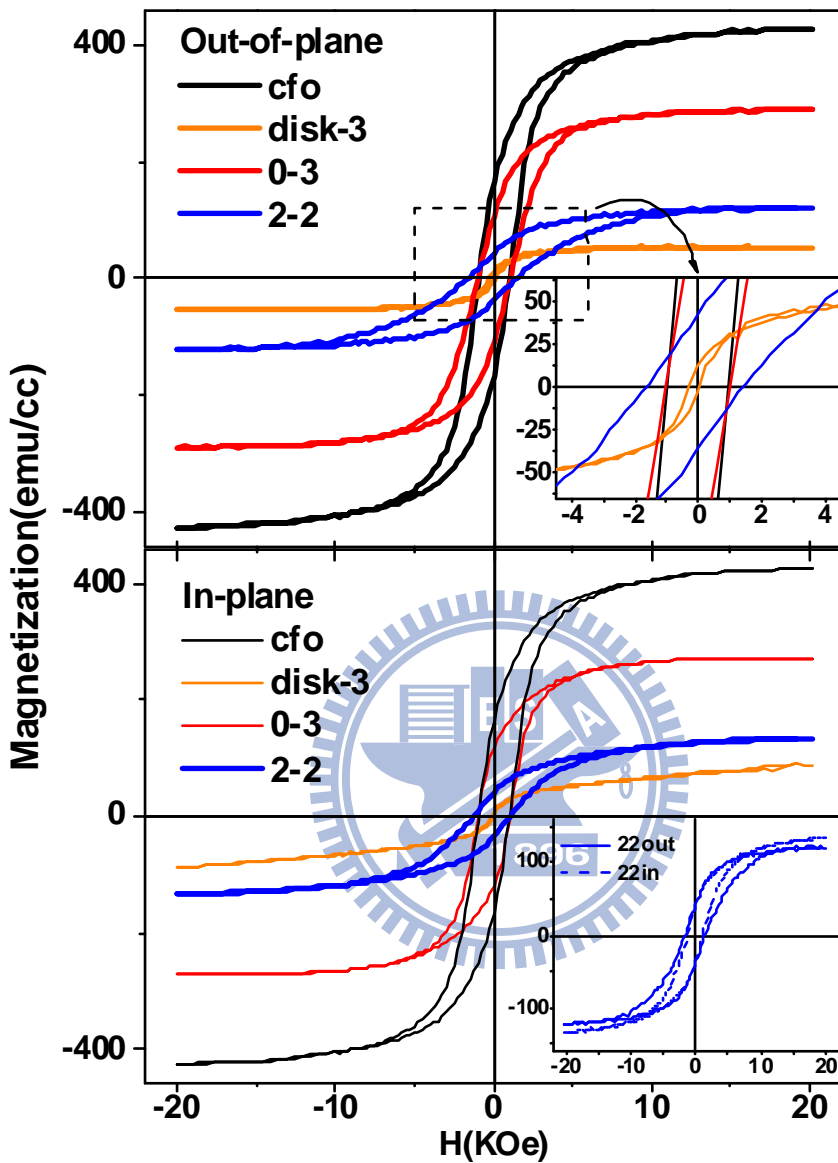


Figure 7.4: Hysteresis loops of out-of-plane and in-plane magnetization for the pure CFO, 0-3, 2-2, and disk-3 samples.

type is the lowest having only 0.2 kOe. O'Handley [8] proposed that the coercivity

$H_c$  decreases with increasing defect size in fuzzy defect case, which is often defined

by strain fields. Wan *et al.* [2] also reported that the easier magnetization characteristic should contribute to the increase of the total magnetocrystalline energy related to the magnetoelastic coupling due to the compressive stress in the CFO phase caused by the lattice mismatch between the CFO and PTO matrices [from](#) our XRD results. Zhang *et al.* [9] also considered the reason that the lattice mismatch induces strains can indeed alter the magnetic properties.

The ME effect involves dynamic magnetoelastic coupling, key requirements for the ferrite phase are unimpeded domain motion and a large magnetostriction  $\lambda$  [10].

A soft initial permeability (low coercivity) is the main ingredient for strong ME effects. In magnetically hard CFO bulk, however, one has the disadvantage of a large coercive field that limits domain rotation. Since the ME effect originates at the interface, it is important to consider the influence of growth-induced stress and its effect on dynamics of domain motion. The lower inset of Figure 7.4 shows the hysteresis loops of the 2-2 type measured in-plane and out-of-plane with an external field up to 20 kOe. It reveals that the in-plane coercivity  $H_c$  is smaller than the out-of-plane one with nonsymmetrical values for the negative and the positive magnetic field. The differences in nonsymmetrical  $H_c$  reveal that it is easier to rotate the magnetic domain in horizontal direction than in vertical direction. It should contribute to the increase of the total magnetocrystalline energy related to the

magnetoelastic coupling due to the compressive stress in the CFO phase caused by the lattice mismatch between the CFO and PTO matrices [8].

As the coupling interaction between ferroelectric and ferromagnetic phases in the multiferroic is still an elastic interaction, the constitutive equations for the coupling magnetic-mechanical-electric interactions in multiferroics can be expressed by direct notation for tensors as [11]

$$\mathbf{D} = e\mathbf{\epsilon} + \kappa\mathbf{E} + \alpha\mathbf{H} + \mathbf{P}_s, \quad (7-1)$$

$$\mathbf{B} = \mu(\mathbf{\epsilon}, \mathbf{E}, \mathbf{H}) \mathbf{H} + \mathbf{M}_s, \quad (7-2)$$

where  $e$ ,  $\epsilon$ ,  $\kappa$ ,  $\alpha$ ,  $\mu$ ,  $\mathbf{D}$ ,  $\mathbf{E}$ ,  $\mathbf{B}$ ,  $\mathbf{H}$ ,  $\mathbf{P}_s$ , and  $\mathbf{M}_s$  are the piezoelectric coefficient, strain, dielectric constant at strain, magnetoelectric coefficient, permeability, electric displacement, electric field, magnetic induction, magnetic field, spontaneous polarization and magnetization, respectively. The magnetization  $\mathbf{M}_s$  in multiferroics is dependent on the direction of electric displacement, therefore, phenomena that the loop slightly shifts toward negative magnetic field should come from the ME effect between ferroelectric and ferromagnetic matrices.

We observed in Figure 7.4 the more apparent softening of initial permeability or low coercivity and asymmetric in-plane hysteresis loop for the disk-3 type. The in-plane negative and the positive coercive field  $H_c$  of the 2-2 type are about -1287.62 and 949.09 Oe; and those of the disk-3 type are -187.74 and 123.64 Oe. The

variation in the difference between the negative and the positive coercive field  $H_c$  of the disk-3 type is 34%, which is larger than that of the 2-2 type of 26%.

We speculate that the absence of saturation magnetization  $M_s$  in-plane loops of the disk-3 and 2-2 types may be due to the coupled interaction between ferromagnetic and ferroelectric materials. Under the magnetization process, the change of CFO structure resulting from magnetostriction could produce stress on the surrounding PTO structure. As the magnetic field increases, the strain imposed by CFO on PTO will increase. The strained PTO bonding along the interface should eventually affect the boundary structure of CFO matrix. Consequently, it not only lowers the values and increases asymmetry of the coercivity  $H_c$  but also causes more difficult to saturate the magnetization of CFO. Since the disk-3 type consists of the self-assembled CFO disks embedded in PTO matrix, it has the largest stress/strain due to the lattice misfit and the strongest chemical bonding between the CFO and PTO matrix, we observed the lowest  $H_c$ , the largest asymmetry of  $H_c$ , and the most difficult saturation of CFO magnetization in the disk-3 type.

### 7.3 Relationship between interfacial phonon behavior and magnetic properties

PTO belongs to the  $C_{4v}^1(P4mm)$  space group with tetragonal phase at RT [12], it has  $3A_1(\text{TO})$ ,  $3E(\text{TO})$ ,  $3A_1(\text{LO})$ , and  $3E(\text{LO})$  Raman active modes. Figure 7.5 shows

the RT Raman spectra of the phonon modes of PTO assigned according to Foster *et al.* [13] to clarify the structural variation of PTO powder on Si (PTO/Si), PTO film on Pt pre-coated Si (PTO/Pt/Si), and three multiferroic films on Pt/Si substrates.  $A_1(\text{TO})$

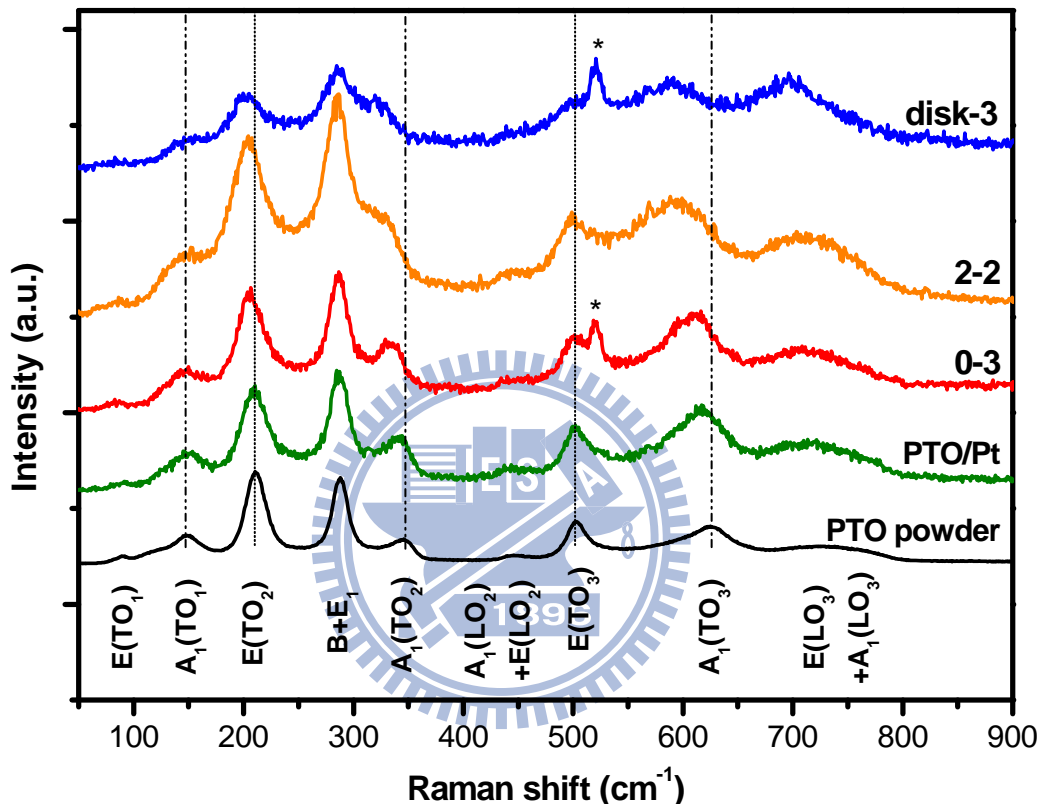
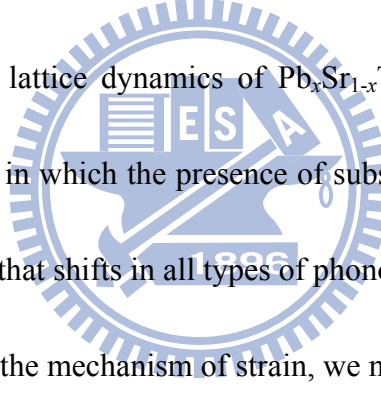


Figure 7.5: Micro Raman spectra of disk-3, 2-2, 0-3 multiferroics together with those of PTO on Pt/Si, and PTO powder for comparison.

mode is especially interesting, since the  $A_1(\text{TO})$  mode consists of displacements of Ti and oxygen ions relative to the lead ions and is, with the  $E(\text{TO})$  mode, a soft mode. On the other hand, CFO belongs to cubic phase (Space Group:  $Fd\bar{3}m$  (227)) [14-16] and the Raman signal is hardly detected. Therefore, we shall concentrate on change

of Raman modes of PTO in various types of CFO/PTO structures.

The phonon modes have remarkable shifts in their frequencies for different types, the  $A_1$  modes especially. The  $A_1(\text{TO}_1)$ ,  $A_1(\text{TO}_2)$ , and  $A_1(\text{TO}_3)$  modes of PTO having frequencies at 150, 350, and 630  $\text{cm}^{-1}$  show significantly red-shifted and broadened while the  $E$  modes vary just marginally in all multiferroics as compared with the pure PTO powders. We speculated that the reasons for the above-mentioned frequency shifts are not from structure change but from the strain either between structures and substrate or intra-structures. The significant shift of  $A_1$  mode with invariable  $E$  mode in this study is unlike the lattice dynamics of  $\text{Pb}_x\text{Sr}_{1-x}\text{TiO}_3$  polycrystalline powder reported by Kuo *et al* [17], in which the presence of substitution  $\text{Sr}^{2+}$  ions on  $\text{PbTiO}_3$  yields structure changes so that shifts in all types of phonon modes.



In order to investigate the mechanism of strain, we need to recognize whether the shift of  $A_1$  mode in multiferroics in this study is due to strains between substrate and structure or intra structures by referring to the spectra of PTO on Pt and Si substrates. In Figure 7.5, we observed that all phonon modes of PTO on Pt and Si substrates are almost invariable or vary just a little bit as compared with ones of the pure PTO powder. It indicates that shift of phonon mode of PTO in three multiferroic samples do not result from interaction between substrates and PTO but from the interfacial stress between CFO and PTO matrices.

In order to further investigate the behavior of  $A_1$  modes belonging to the PTO matrix in three multiferroic samples, Lorentzian line fitting was adopted to resolve the overlapping modes. The fitting results are in good agreement with experimental spectra (not shown) and the peak positions of  $A_1(\text{TO}_1)$ ,  $A_1(\text{TO}_2)$ , and  $A_1(\text{TO}_3)$  of various types were plotted in Figure 7.6. For PTO matrix, the results of XRD indicate prefer-oriented vertical  $a$ -axis growth with the  $c$ -axis lying. The oxygen atoms and cations (Pb and Ti) of PTO oscillate along  $c$ -axis in the  $A_1(\text{TO})$  modes, while the atoms oscillate on the plane composed by  $a$  and  $b$  axes in the  $E$  modes. Undoubtedly, the  $A_1$  modes, describing the vibration of atoms along  $c$  direction, could be significantly influenced by the strains resulting from the interfacial mismatch of PTO with CFO. However, owing to deficit of interaction with ferromagnetic materials, the behavior of  $E$  modes just like the pure PTO films having slightly shift in positions of their spectral peaks.

Further analyzing the phonon modes in three multiferroic samples, we observed the largest shift of  $A_1(\text{TO}_2)$  and  $A_1(\text{TO}_3)$  in the disk-3 type, whereas the smallest shift in the 0-3 type. It indicates that the Raman shift in the disk-3 type is due to the stronger coupling between BTO and CFO matrices resulting from existing most  $a$ -domain [18, 19], in which the  $c$ -axis of PTO matrix strongly bonds with CFO one. This result agrees well with the results of magnetic properties of multiferroics that

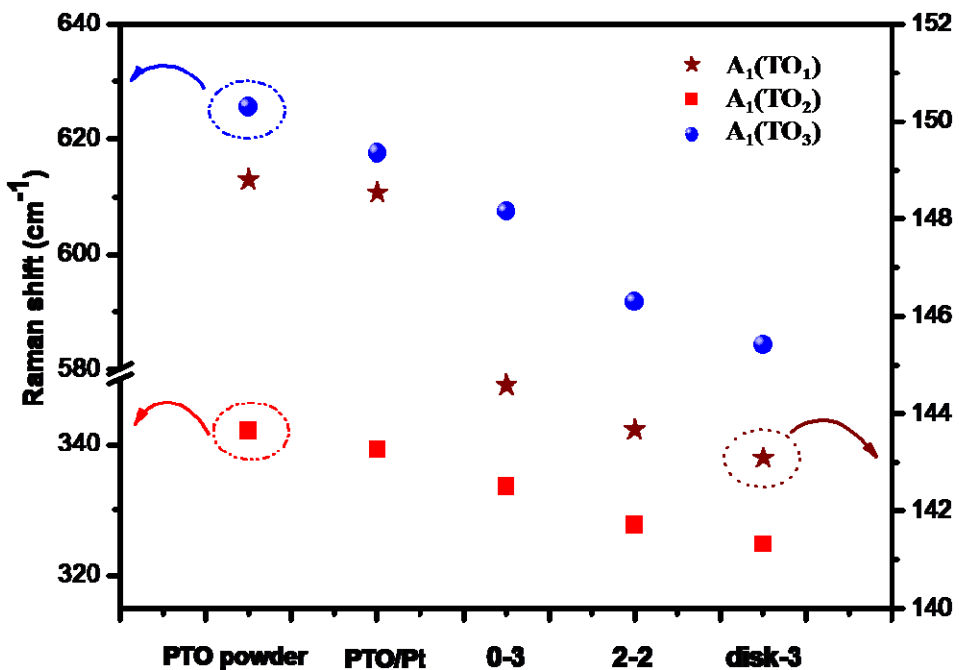


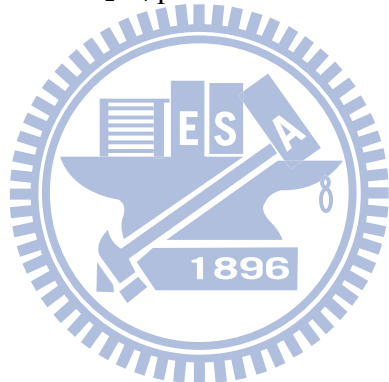
Figure 7.6: The fitted Raman shift of the  $A_1(TO_3)$ ,  $A_1(TO_2)$ , and  $A_1(TO_1)$  modes as a function of film type.

depends on the interface stress between CFO and PTO matrices which is also sensitive to the behavior of interfacial phonons. Therefore, the micro-Raman spectroscopy is a good probe for investigating the multiferroics and is under the way to study interfacial phonons under the applied magnetic field.

## 7.4 Summary

The characteristics of three different geometric forms of the  $PbTiO_3$ - $CoFe_2O_4$  multiferroics fabricated by the simple solution method has been investigated using OM, FESEM, XRD, SQUID, and micro-Raman spectroscopy. The analysis of the

magnetic and Raman measurements under different geometric forms indicates the dependence of magnetic property and behavior of interfacial phonons on stress/strain due to the lattice misfit and the chemical bonding at the interface between  $\text{CoFe}_2\text{O}_4$  and  $\text{PbTiO}_3$  matrices. The largest nonsymmetrical coercivity  $H_c$  and the absence of saturation magnetization  $M_s$  of  $\text{CoFe}_2\text{O}_4$  consist with the largest shift of  $A_1(\text{TO}_2)$  and  $A_1(\text{TO}_3)$  modes of  $\text{PbTiO}_3$  in the disk-3 type, the self-assembled  $\text{CoFe}_2\text{O}_4$  disks embedded in  $\text{PbTiO}_3$  matrix, than the other types of the  $\text{CoFe}_2\text{O}_4$  and  $\text{PbTiO}_3$  multilayered structure and the  $\text{CoFe}_2\text{O}_4$  particles embedded in  $\text{PbTiO}_3$  matrix.



## References

[1] H. Zheng, J. Wang, S. E. Lofland, Z. Ma, L. Mohaddes-Ardabili, T. Zhao, L. Salamanca-Riba, S. R. Shinde, S. B. Ogale, F. Bai, D. Viehland, Y. Jia, D. G. Schlom, M. Wuttig, A. Roytburd, and R. Ramesh, *Science* **303**, 661-663 (2004).

[2] J. G. Wan, X. W. Wang, Y. J. Wu, M. Zeng, Y. Wang, H. Jiang, W. Q. Zhou, G. H. Wang, and J. M. Liu, *Appl. Phys. Lett.* **86**, 122501 (2005).

[3] C. W. Nan, G. Liu, Y. H. Lin, and H. Chen, *Phys. Rev. Lett.* **94**, 197203 (2005).

[4] D. S. Fu, T. Ogawa, H. Suzuki, and K. Ishikawa, *Appl. Phys. Lett.* **77**, 1532-1534 (2000).

[5] J. Barbosa, B. G. Almeida, J. A. Mendes, A. G. Rolo, J. P. Araujo, and J. B. Sousa, *J. Appl. Phys.* **101**, 09M101 (2007).

[6] N. Ortega, A. Kumar, P. Bhattacharya, S. B. Majumder, and R. S. Katiyar, *Phys. Rev. B* **77**, 014111 (2008).

[7] H. M. Zheng, J. Kreisel, Y. H. Chu, R. Ramesh, and L. Salamanca-Riba, *Appl. Phys. Lett.* **90**, 113113 (2007).

[8] R. C. O'Handley, *Modern Magnetic Materials: Principles and Applications* (Wiley, New York) (2000).

[9] Y. Zhang, C. Y. Deng, J. Ma, Y. H. Lin, and C. W. Nan, *Appl. Phys. Lett.* **92**, 062911 (2008).

[10] G. Srinivasan, E. T. Rasmussen, Gallegos, R. Srinivasan, Y. I. Bokhan and V. M. Laletin, *Phys. Rev. B* **64**, 214408 (2001).

[11] C. W. Nan, G. Liu, Y. Lin, and H. Chen, *Phys. Rev. Lett.* **94**, 197203 (2005).

[12] J. A. Sanjurjo, E. L. ez-Cruz, and B. Gerald, *Phys. Rev. B* **28**, 7260 (1983).

[13] C. M. Foster, Z. Li, M. Grimsditch, S. K. Chan, and D. J. Lam, *Phys. Rev. B* **48**, 10160 (1993).

[14] Z. W. Wang, R. T. Downs, V. Pischedda, R. Shetty, S. K. Saxena, C. S. Zha, Y. S. Zhao, D. Schiferl, and A. Waskowska, *Phys. Rev. B* **68**, 094101(2003).

[15] O. N. Shebanova and P. Lazor, *J. Solid State Chem.* **174**, 424-430 (2003).

[16] J. V. Larry, *Phys. Rev. B* **9**, 5236 (1974).

[17] S. Y. Kuo, W. Y. Liao, and W. F. Hsieh, *Phys. Rev.B* **64**, 224103 (2001).

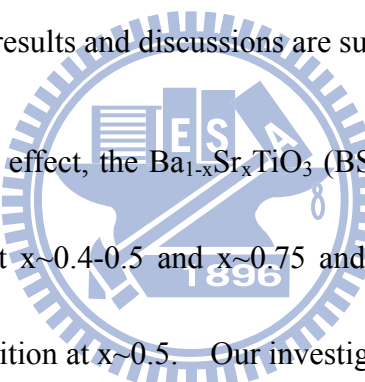
[18] S. H. Lee, H. M. Jang, S. M. Cho, and G. C. Yi, *Appl. Phys. Lett.* **80**, 3165-3167 (2002).

[19] A. Bartasyte, O. Chaix-Pluchery, J. Kreisel, C. Jimenez, F. A. Weiss, Z. Saltyte, and M. Boudard, *J. Appl. Phys.* **103**, 014103 (2008).

# Chapter 8 Conclusion and Prospective

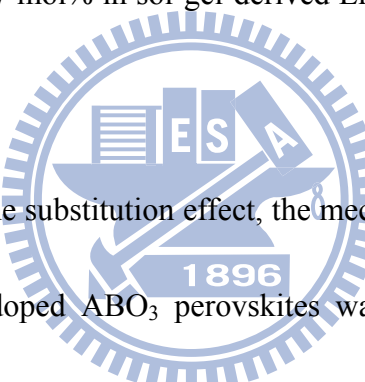
## 8.1 Conclusion

The major accomplishment of this work was the study on the influence of perovskite structure by substitution, size and strain effects on characteristics of ferroics, namely,  $\text{Er}^{3+}$ -doped  $\text{Pb}_{0.8}\text{La}_{0.2}\text{TiO}_3$ ,  $\text{Er}^{3+}$ - $\text{Yb}^{3+}$  codoped  $\text{ABO}_3$  perovskites with different degrees of tetragonality (including  $\text{PbTiO}_3$ ,  $\text{BaTiO}_3$ , and  $\text{SrTiO}_3$ ),  $\text{BaTiO}_3$  nanoparticles, and  $\text{PbTiO}_3\text{-CoFe}_2\text{O}_4$  multiferroics synthesized by chemical solution methods. All the results and discussions are summarized as follow:



Due to the substitution effect, the  $\text{Ba}_{1-x}\text{Sr}_x\text{TiO}_3$  (BST) system exhibits structural ordering transition points at  $x\sim 0.4\text{-}0.5$  and  $x\sim 0.75$  and  $\text{Pb}_{1-x}\text{Sr}_x\text{TiO}_3$  (PST) exhibits one structural ordering transition at  $x\sim 0.5$ . Our investigations indicate that the lattice ratio  $c/a$  is around 1.002 for the undoped  $\text{Pb}_{0.8}\text{La}_{0.2}\text{TiO}_3$  (PLT) polycrystalline films, and slightly increases and then declines to around 1.001 at 7 mol%  $\text{Er}^{3+}$ -dopant, and then increases to 1.007 for the samples with 9 and 15 mol% in sol-gel-derived  $\text{Er}^{3+}$ -doped PLT polycrystalline films. However, our investigations also found that the maximum emission was observed at 7 mol% but no emission for  $\text{Er}^{3+}$  dopant larger than 9 mol%, which possesses the higher tetragonality than for the 7 mol% one. From the results of Raman spectra, the peak attributed to  $\text{A}_1(\text{TO}_3)+\text{E}(\text{TO}_3)$  phonon

modes keeps almost unchanged as  $\text{Er}^{3+}$  concentration increases from 0 mol% to 7 mol%, but vanishes for samples with 9 and 15 mol%  $\text{Er}^{3+}$  concentrations. The disappearance of Raman modes due to weak disorder effect (resulting from a displacement of Ti ion is caused by decreasing the crystal diameter to result in the formation of a centrosymmetric structure with increasing  $\text{Er}^{3+}$  concentration. Finally, our investigation show destruction to a displacement of Ti in the short-range structure by observing the disappearance of fluorescence emission and Raman signals when the  $\text{Er}^{3+}$  concentration exceeds 7 mol% in sol-gel-derived  $\text{Er}^{3+}$ -doped PLT polycrystalline films.

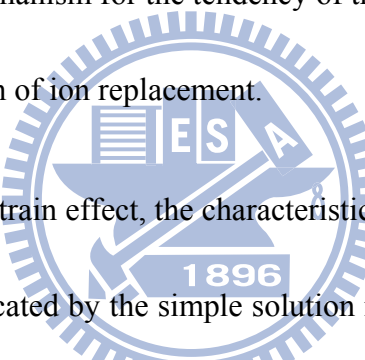


For another study on the substitution effect, the mechanism of upconversion (UC) emission in  $\text{Er}^{3+}$ - $\text{Yb}^{3+}$  co-doped  $\text{ABO}_3$  perovskites was discussed. As increasing  $\text{Yb}^{3+}$  co-doped concentrations in 6 mol%  $\text{Er}^{3+}$  doped  $\text{PbTiO}_3$ ,  $\text{BaTiO}_3$ , and  $\text{SrTiO}_3$  polycrystalline powder samples synthesized by sol-gel method, we have observed the room-temperature green UC emission at 550 nm being quenched by the simultaneously enhanced red UC emission at 660 nm under the 980-nm laser excitation. For codoping  $\text{Yb}^{3+}$  ions up to 6 mol% in  $\text{PbTiO}_3$  and only  $\text{Er}^{3+}$  doped  $\text{PbTiO}_3$  samples, which still possess relatively large tetragonality, the green UC emission is still much stronger than red one. In these cases, both the UC emissions are dominated by the two-photon process. But, as further increasing the  $\text{Yb}^{3+}$  ion

concentration, the crystal structures tend to become cubic phase with enhancing red UC emission and almost diminishing in green emission. Since the pure BaTiO<sub>3</sub> crystal exhibits weaker tetragonality than PbTiO<sub>3</sub>, the stronger red emission and weaker green one were expected at the lower codoped Yb<sup>3+</sup> concentration in BaTiO<sub>3</sub> system than in PbTiO<sub>3</sub> one. The observed quench of green radiation accompanied with enhancement of red radiation should be due to the efficient energy back-transfer (EBT) process by raising Yb<sup>3+</sup> concentration. The efficient EBT process requires not only Yb<sup>3+</sup> concentration but also level match of  $^4S_{3/2} \rightarrow ^4I_{13/2}$  in Er<sup>3+</sup> and  $^2F_{7/2} \rightarrow ^2F_{5/2}$  in Yb<sup>3+</sup> under assistance of Boltzmann distributed population within the manifold of  $^4S_{3/2}$  or/and  $^4I_{13/2}$  (Er<sup>3+</sup>) state affected by the crystal field with different symmetries. As a result, declining tetragonality results in the centrosymmetric crystal field for high Yb<sup>3+</sup>-ion concentration to achieve the level match required for the EBT process that may be difficult to be fulfilled with asymmetric crystal field in the tetragonal phase.

Additionally, we report, in contrast to the substitution effect, the size effect on structure for BaTiO<sub>3</sub> nanoparticles synthesized by the glycothermal method. We applied a single tetragonal-phase model to refine the crystal structure and the coupled-phonon model to analyze the coupled  $A_1$ (TO) modes upon particle size decreasing from 140 nm to 30 nm. Our investigations indicate that the weak strength

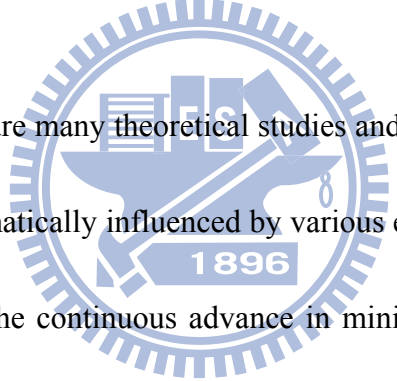
of coupling between  $A_1(\text{TO}_1)$  and  $A_1(\text{TO}_2)$  leads to a change from a spectral dip at 180  $\text{cm}^{-1}$  for  $A_1(\text{TO}_1)$  phonon to a peak at the same position and found that the approach of uncoupled  $\omega_2$  and  $\omega_3$  with less tetragonality due to decreasing the particle size results in slightly increasing in  $\omega_{23}$ . The larger coupling strength repels these two modes farther so that the less reducing in spectral separation. According to the results of decomposition, we also observed the decreasing LO-TO splitting with the decline of tetragonality and expansion of the unit-cell volume. And the change of unit-cell volume is the dominant mechanism for the tendency of the LO-TO splitting in  $\text{BaTiO}_3$  system without complication of ion replacement.



Finally, regarding the strain effect, the characteristics of three different geometric forms of multiferroics fabricated by the simple solution method has been investigated using optical microscopy (OM), field-emission scanning electron microscopy (FESEM), X-ray diffraction (XRD), superconducting quantum interference device (SQUID), and micro-Raman spectroscopy. We report on the stress dependence of the behavior of interfacial phonon and the magnetic properties in three multiferroics consisting of the different geometric shapes of ferromagnetic  $\text{CoFe}_2\text{O}_4$  (CFO) embedded in ferroelectrics  $\text{PbTiO}_3$  (PTO). Their energy of interfacial phonon and ferromagnetic properties depend on stress due to not only the lattice misfit but also the degree of chemical bonding at the interface between CFO and PTO matrices. The

disk-3 type structure, the self-assembled CFO disks embedded in PTO matrix, illustrates the strong elastic interactions between the two phases. The larger nonsymmetrical coercivity  $H_c$  and the absence of saturation magnetization  $M_s$  of CFO matches with the larger Raman shift of  $A_1(\text{TO}_2)$  and  $A_1(\text{TO}_3)$  modes of PTO found in the disk-3 type than the other types of the CFO and PTO multilayered structure and the CFO particles embedded in PTO matrix.

## 8.2 Prospective



In recent years, there are many theoretical studies and many experimental reports on physical properties dramatically influenced by various effects, such as substitution, shape, size, strain, etc. The continuous advance in miniaturization of devices, fine structure as a ferric material have been applied in advanced electric devices such as ferroelectric random access memory (FRAM), multilayer ceramic capacitor (MLCC), and in other integrated devices. Among these effects, the size dependence of properties with different shapes is presently one of the major research topics.

It is necessary for us to synthesize various high purity perovskite nanocrystals with uniform size and homogeneous shape.  $\text{BaTiO}_3$  nanoparticles with uniform size were synthesized by glycothermal treatment and size-dependent properties were

discussed. Furthermore, much effort has been recently put into morphology controlled synthesis of crystalline ferroelectric oxide materials because the effects of a large nonlinear optical coefficient and a large dielectric constant are highly dependent on the size and shape. [1] Of various nanostructures low-dimensional nanostructures, such as nanoparticles, nano-wires, nanocubes and nanorods, have especially received great interest from the scientific and engineering communities [2, 3] because these structures exhibit distinct physical and chemical properties from bulk materials due to their smaller particle sizes and larger surface-to-volume ratios. Thus, many studies have probed the optical, [4] electronic, [5] and magnetic [6] properties of these nanostructures. Scientists expect one-dimensional (1D) structures, nano-rods, and nanowires to provide new alternatives for developing devices because of recent theoretical studies from the first principles and experiments on ferroelectric nanowires. This possibility primarily arises because the size-dependent ferroelectricity of 1D structures functions with much smaller diameters than do 0-D structures (nanoparticle), and the Curie temperature is reduced as the diameter of the 1D structure is reduced. [7-9] Wang *et al.* [10] also reported a method for studying the axial poling and switching in 1D BaTiO<sub>3</sub> nanowires by using piezoresponse force microscopy (PFM).

Therefore, we have proposed the novel insight into the nature of low-dimensional  $\text{ABO}_3$  nanostructures related to the size and shape experimentally and theoretically. Because the  $\text{ABO}_3$  1D nanostructure is difficult to obtain due to the isotropy of the  $\text{ABO}_3$  crystal structure and the anisotropy of the 1D structure, the control of nucleation and growth of 1D nanostructure materials is still a big challenge. Presently, the three-series products (BT-1, spherical  $\text{BaTiO}_3$ ; BT-2, cube-shaped  $\text{BaTiO}_3$ ; and BT-3, rod-shaped  $\text{BaTiO}_3$ ) were synthesized roughly with different barium and multishaped titanium precursors. (see Figure 8.1)

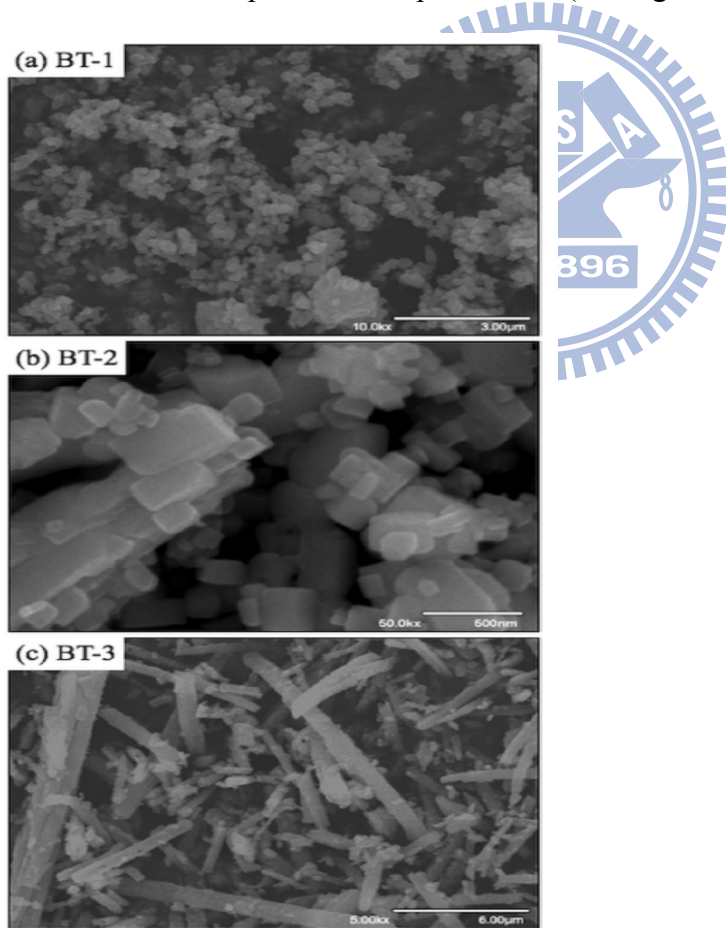


Figure 8.1: SEM images of the three-series products: BT-1, BT-2, and BT-3.

Magnetoelectric (ME) effect in multiferroics is an important mechanism in applications of transducers, actuators, and sensors. The ME coupling in bi-ferroic (e.g.,  $\text{PbTiO}_3\text{-CoFe}_2\text{O}_4$ ) self-assembled epitaxial nanostructures occurs indirectly via the elastic coupling. Although theoretical studies [11-13] point out the importance of the residual strains in the ME coupling, there is limited information on the lattice strains in ferromagnetic nanostructures in a ferroelectric matrix. We also reported on the relationship between local behavior of interfacial phonons and ferromagnetic properties in bi-ferroic ( $\text{PbTiO}_3\text{-CoFe}_2\text{O}_4$ ). Their energy of interfacial phonons and ferromagnetic properties depend on stress due to not only the lattice misfit but also the degree of chemical bonding at the interface between matrices. At the same time, we still hope a detailed study of lattice strains for bi-ferroic nanocomposite heteroepitaxial structure could be continued experimentally and theoretically in the future based on the accomplishment have been done in this thesis.

## References

- [1] S. O'Brien, L. Brus, and C. B. Murray, *J. Am. Chem. Soc.* 123, 12085 (2001).
- [2] A. P. Alivisatos, *Science* 271, 933 (1996).
- [3] J. T. Hu, T. W. Odom, and C. M. Lieber, *Acc. Chem. Res.* 32, 435 (1999).
- [4] M. H. Huang, S. Mao, H. Feick, H. Q. Yan, Y. Y. Wu, H. Kind, E. Weber, R. Russo, and P. D. Yang, *Science* 292, 1897 (2001).
- [5] T. Thurn-Albrecht, J. Schotter, C. A. Kastle, N. Emley, T. Shibauchi, L. Krusin-Elbaum, K. Guarini, C. T. Black, M. T. Tuominen, and T. P. Russell, *Science* 290, 2126 (2000).
- [6] W. J. Liang, M. Bockrath, D. Bozovic, J. H. Hafner, M. Tinkham, and H. Park, *Nature*, 411, 665 (2001).
- [7] G. Geneste, E. Bousquet, J. Junquera, P. Ghosez, *Appl. Phys. Lett.* 88, 3 (2006).
- [8] J. W. Hong and D. N. Fang, *Appl. Phys. Lett.* 92, 3 (2008).
- [9] J. E. Spanier, A. M. Kolpak, J. J. Urban, I. Grinberg, O. Y. Lian, W. S. Yun, A. M. Rappe, and H. Park, *Nano Lett.* 6, 735 (2006).
- [10] Z. Y. Wang, A. P. Suryavanshi, and M. F. Yu, *Appl. Phys. Lett.* 89, 3 (2006).
- [11] J. Slutsker, Z. Tan, A. L. Roytburd, and I. Levin, *J. Mater. Res.* 22, 2087 (2007).
- [12] C. G. Zhong, Q. Jiang, J. Fang, and X. F. Jiang, *J. Appl. Phys.* 105, 044901 (2009).
- [13] G. Liu, C. W. Nan, and J. Sun, *Acta Mater.* 54, 917 (2006).

# 黃同慶簡歷 (Vita)

## 基本資料

姓名：黃 同 慶 (Tung-Ching Huang)

性別：男

出生年月日： 1973 年 10 月 25 日

籍貫： 台南縣

永久通訊處：(722)台南縣佳里鎮興化里8鄰佳里興479

號之3

email:[htc.eo92g@nctu.edu.tw](mailto:htc.eo92g@nctu.edu.tw); [htc.eo98g@gmail.com](mailto:htc.eo98g@gmail.com)

## 學歷：

1993.8 - 1998.7 國立台灣師範大學物理系 學士

2001.8 - 2003.7 國立交通大學光電所 碩士

2003.8 - 2009.10 國立交通大學光電所 博士

## 經歷：

1998.8 - 2001.7 臺北市立重慶國中理化教師

## 博士論文題目：

鈣鈦礦結構對螢光及鐵性材料特性的影響

Influence of perovskite structure on luminescence and  
characteristics of ferroics

# Publication list

## I. Refereed Journal Publications:

- 1 **Tung-Ching Huang**, Mei-Tan Wang, Hwo-Shuenn Sheu, and Wen-Feng Hsieh, “Size-dependent lattice dynamics of barium titanate nanoparticles”, *Journal of Physics-Condensed Matter*, 19, 476212 (2007).
- 2 **Tung-Ching Huang** and Wen-Feng Hsieh, “Er-Yb Codoped Ferroelectrics for Controlling Visible Upconversion Emissions”, *Journal of Fluorescence*, 19, 511 (2009).
- 3 **Tung-Ching Huang** and Wen-Feng Hsieh, “Destruction of the short-range disorder due to erbium doping in  $Pb_{0.8}La_{0.2}TiO_3$  films”, *Journal of Raman Spectroscopy*, accepted for publication (2009).
- 4 Kuan-Chih Huang, **Tung-Ching Huang**, and Wen-Feng Hsieh, “Morphology-Controlled Synthesis of Barium Titanate Nanostructures”, *Inorganic Chemistry*, 48(19):9180-4 (2009).

## II. Conference:

1. **Tung-Ching Huang** and Wen-Feng Hsieh, “Decreasing Splitting of LO-TO Phonons in  $BaTiO_3$  Nanoparticles Due to Unit-cell Volume”, in 2006 MRS Spring Meeting, San Francisco, USA, post paper (2006).
2. **Tung-Ching Huang** and Wen-Feng Hsieh, “Quenching green and enhancing red upconversion emissions of  $Er^{3+}$  by reducing tetragonality in  $Yb^{3+}$  co-doped ferroelectrics”, 2008 E-MRS Fall Meeting, Warsaw, Poland, oral paper (2008).
3. **Tung-Ching Huang** and Wen-Feng Hsieh, “Destruction to the short-range disorder due to erbium dopant in  $Pb_{0.8}La_{0.2}TiO_3$  poly-crystalline films”, in Conference of Year 2005 Annual Meeting of Chinese Physical Society, Kaoshiung, TAIWAN, oral paper (2005).
4. **Mei-Tan Wang**, **Tung-Ching Huang**, and Wen-Feng Hsieh, “Grain size effect on the lattice dynamics of barium titanate nanoparticles” in Conference of Year 2007 Annual Meeting of Chinese Physical Society, Chunli, TAIWAN, oral paper (2007)
5. **Tung-Ching Huang**, Chung-Ting Li, Shou-Yi Kuo, and Wen-Feng Hsieh, in Proceedings of Optics and Photonics Taiwan'02, Taipei, TAIWAN, post paper (2002)